CORA Cork Open Research Archive
Cartlann Taighde Oscailte Chorcaí

Title	Nanostructured ferroelectric materials
Authors	Varghese, Justin M.
Publication date	2012-12
Original Citation	Varghese, J. D. 2012. Nanostructured ferroelectric materials. PhD Thesis, University College Cork.
Type of publication	Doctoral thesis
Link to publisher's version	http://pubs.acs.org/doi/pdfplus/10.1021/nl2039106, http://pubs.acs.org/doi/pdfplus/10.1021/cm301928w
Rights	© 2012, Justin Manjaly Varghese - http://creativecommons.org/licenses/by-nc-nd/3.0/
Download date	2024-03-29 11:15:06
Item downloaded from	https://hdl.handle.net/10468/992

UCC
University College Cork, Ireland
Coláiste na hOllscoile Corcaigh

Nanostructured Ferroelectric Materials

Justin Manjaly Varghese, MSc.

ucc

Coláiste na hOllscoile Corcaigh, Éire
University College Cork, Ireland

Thesis presented for the degree of Doctor of Philosophy to the

National University of Ireland, University College Cork.

Tyndall National Institute and Department of Chemistry

Supervisor: Prof. Justin D. Holmes and Prof. Roger W. Whatmore

Head of the Department: Prof. Michael A. Morris

December 2012

Declaration

I, Justin Manjaly Varghese, hereby confirm that the work presented within this thesis for the degree of Doctor of Philosophy, is my own research work, and has not been submitted for any other degree, either at University College Cork or elsewhere.

_____ _____

Justin Manjaly Varghese Date

Abstract

Nanostructured materials are central to the evolution of future electronics and information technologies. Ferroelectrics have already been established as a dominant branch in the electronics sector because of their diverse application range such as ferroelectric memories, ferroelectric tunnel junctions, etc. The on-going dimensional downscaling of materials to allow packing of increased numbers of components onto integrated circuits provides the momentum for the evolution of nanostructured ferroelectric materials and devices. Nanoscaling of ferroelectric materials can result in a modification of their functionality, such as phase transition temperature or Curie temperature (T_C), domain dynamics, dielectric constant, coercive field, spontaneous polarisation and piezoelectric response. Furthermore, nanoscaling can be used to form high density arrays of monodomain ferroelectric nanostructures, which is desirable for the miniaturisation of memory devices.

This thesis details the use of various types of nanostructuring approaches to fabricate arrays of ferroelectric nanostructures, particularly non-oxide based systems. The introductory chapter reviews some exemplary research breakthroughs in the synthesis, characterisation and applications of nanoscale ferroelectric materials over the last decade, with priority given to novel synthetic strategies. Chapter 2 provides an overview of the experimental methods and characterisation tools used to produce and probe the properties of nanostructured antimony sulphide (Sb_2S_3), antimony sulpho iodide (SbSI) and lead titanate zirconate (PZT). In particular, Chapter 2 details the general principles of piezoresponse microscopy (PFM). Chapter 3 highlights the fabrication of arrays of Sb_2S_3 nanowires with variable diameters using newly developed solventless template-based approach. A detailed account of domain imaging and polarisation switching of these nanowire arrays is also provided. Chapter 4 details the preparation of vertically aligned arrays of SbSI nanorods and nanowires using a surface-roughness assisted vapour-phase deposition method. The qualitative and quantitative nanoscale ferroelectric properties of these nanostructures are also discussed. Chapter 5 highlights the fabrication of highly ordered arrays of PZT nanodots using block copolymer self-assembled templates and their ferroelectric characterisation using PFM. Chapter 6 summarises the conclusions drawn from the results reported in chapters 3, 4 and 5 and the future work.

Acknowledgements

It is with immense gratitude that I acknowledge the great support and help of my supervisor Prof. Justin Holmes for his expert and valuable guidance extended to me during my PhD. Without his constant encouragement, persistent help and humorous jibes this thesis would not have been possible. It gives me great pleasure in acknowledging the support and guidance of my co-supervisor Prof. Roger Whatmore, who has the attitude and the substance of a genius and an excitement with regard to explaining the basics of material physics.

I also take this opportunity to record my sincere thanks to Prof. Martyn Pemble for his great mentoring and also for providing an opportunity to work with the FORME research cluster at Tyndall National Institute.

I am indebted to 'The great bunch of lads in 115' for keeping my mood up always with their great 'craic and banter'. First of all, I would like to thank my early colleagues in 115: J O'B, Ciara, Richard Hobbs, David 'legend' Burke, Mark, Arun, Gill, Timmy G, Kamil, Machteld, Richard Phelan and Ju Xu. Many thanks to the person whose name I cannot pronounce properly yet (S'w'en Barth) for his help with TEM imaging, and also for his constant encouragement and positive criticism. Also, I would like to express my deepest thanks to my new fellow mates in 115: Olaaan, Reganator, 'Bantry' John, 'Cool' Subha, Angelica, Brenda, Mike, Elaine and Colm Glynn for their amazing support. Thanks also to the 343 team: Colm Eile (my fellow house mate), Parvanellah, Dipu, Tom, Atul, Atul Eile, Barbara, Matt, Ben, Keith, Ivan, Cian, Colm O' Mahony and Timothy. Sincere thanks to Tandra for her great help and assistance in making and analysing BCP template samples. Thanks to the ERI members Pal, Joe, Eoin and especially Pete for XPS analysis.

‘Rocking’ Raj and ‘Classy’ Sankar, my immense thanks to you guys for your great support and company. Also, thanks to my fellow ‘Malayalee (മലയാളി)’ friends in UCC Sibu ji, Ravi bhai, Krishna, Satheesh, Lekha, Vimal, Deepak and Ragh for their marvellous company that always made me feel at home.

This thesis would not have been complete without decent SEM and TEM images. I owe my deepest thanks to Nikolay, for providing access to the electron microscopy facility at the EMAF lab in Tyndall. I also thank ‘Mr. Top Gun’ Colm O’ Regan for spending his time taking great TEM images of my samples. I also wish to thank my Tyndall colleagues Yordan, Vince Lodge, Michael Schmidt, Patrick Carolan, Roisin, Anushka, Shelly, Krimo Khalfi, Carmel Kelleher, Panfeng Zhang, and Mary-Claire O’ Regan for their assistance and support. Special thanks to Lynette Keeney and Nitin Deepak for their helping hand with the PFM measurements.

Many thanks to the fellow neighbours of 115: especially Terry ‘my local guardian in UCC’, and the great technicians Johnny, Tony and Mick for the help and for the ‘numerous’ humorous conversations. Special thanks to Matthias for letting me use his ‘INTEL private office’ to write my thesis, without it I would not be finished in time, and also for his superb IT support.

I wish to express my sincere thanks to all the administrative and technical staff at the Department of Chemistry and Tyndall for their assistance and support. Special thanks to Eileen, Christine, Colette, Claire, Mary, Chrissie, Tina, Pat, Rose, Agnes, Derry, Noel and Donnacha of Department of Chemistry for their help.

Dear my wonderful wife Jyothsana, a million thanks for your limitless love, support and caring you offered. My heartfelt thanks to my loving parents: Varghese and Rosily, and my siblings: Jerin and Jain, you were my prime source of inspiration. Above all, I thank almighty GOD for everything.

Dedicated to my family

Table of contents

Declaration *ii*

Abstract *iii*

Acknowledgements *iv*

Chapter 1 Introduction **1**

1.1 A Short History of Ferroelectricity and Piezoelectricity **2**

1.1.1 A Primer on Ferroelectric Materials 2

1.2 Nanoscale Ferroelectrics and Piezoelectrics **5**

1.3 Classification of Ferroelectric Nanostructures **7**

1.4 Fabrication of Ferroelectric Nanostructures **9**

1.4.1 Zero-dimensional ferroelectric nanostructures 9

1.4.2 One-dimensional ferroelectric nanostructures 12

1.4.3 Two-dimensional ferroelectric nanostructures 19

1.4.4 Three-dimensional ferroelectric nanostructures 26

1.5 Characterisation of Nanoscale Ferroelectric Materials **28**

1.6 Scaling Effects of Nanoscale Ferroelectric Materials **33**

1.7 Applications of Nanoscale Ferroelectric Materials **40**

1.8 Future Outlook of Nanoscale Ferroelectric Materials **44**

1.9 Thesis Summary **45**

1.10 References **47**

Chapter 2 Experimental Methods **64**

2.1 Preparation of Tris(diethyldithiocarbamate) Antimony (III) **65**

2.2 Preapartion of Anodic Aluminium Oxide (AAO) Templates **66**

2.2.1 Solventless preparation of arrays of antimony sulphide nanowires 68

2.3 Vapour Phase Growth of SbSI Nanorods **70**

2.4 Fabrication of Arrays of Lead Zirconate Titanate Nanodots **72**

2.5 PFM analysis of Sb_2S_3-AAO Samples **73**

2.5.1 Acquisition of polarisation-electric field hysteresis loops 75

2.6 Structural and Morphological Characterisation Techniques **75**

2.6.1 X-ray diffraction analysis 75

2.6.2 Electron microscopy analysis 76

2.6.3 X-ray photoelectron spectroscopy 77

2.7 References **78**

Chapter 3 Nanoscale Ferroelectric and Piezoelectric Properties of Sb_2S_3 Nanowire Arrays **79**

3.1 Abstract **80**

3.2 Background **80**

3.2.1 Antimony sulphide (Sb_2S_3) 80

3.2.2 Synthesis of antimony sulphide nanostructures 81

3.3 Results and Discussion **84**

3.3.1 Thermogravimetric analysis of $Sb(S_2CNEt_2)_3$ 84

3.3.2 Morphological analysis 84

3.3.3 Structural and compositional analysis 87

3.3.4 Nanoscale ferroelectric and piezoelectric properties of Sb_2S_3 nanowire arrays: PFM analysis 91

3.3.5 Bulk ferroelectric measurements on Arrays of Sb_2S_3-AAO nanowires 103

3.4 Conclusions 106

3.5 References 107

Chapter 4 Surface Roughness Assisted Growth of Vertically Oriented Ferroelectric SbSI Nanorods 111

4.1 Abstract 112

4.2 Background 113

4.2.1 Antimony sulphoiodide (SbSI) 113

4.2.2 Vertically aligned arrays of SbSI nanowires 114

4.3 Results and Discussion 115

4.3.1 Growth of SbSI nanorods on AAO/Ti/Si substrates 116

4.3.2 Growth of arrays of SbSI nanowires on Pt/Si substrates 124

4.4 Conclusion 135

4.5 References 136

Chapter 5 Fabrication of Arrays of PZT Nanodots via Block Co-Polymer Self-Assembly 140

5.1 Abstract 141

5.2 Introduction 142

5.2.1 Block co-polymer Self-assembled Templates 142

5.3 Results and Discussion 144

5.3.1 Structural and morphological characterisation of PZT nanodot arrays 144

5.3.2 Piezoresponse force microscopy analysis of arrays of PZT nanodots 152

5.4 Conclusion 156

5.5 References 157

Chapter 6 Conclusions and Future Work 160

6.1 Conclusions and Future Work 161

6.2 References 166

जो हुआ वह अच्छा हुआ।
जो हो रहा है, वह अच्छा हो रहा है ।
जो होगा, वह भी अच्छा होगा ।
परिवर्तन ही संसार का नियम है।

श्रीमद् भगवद गीता सार

"Whatever has happened has happened for good.

Whatever is happening is happening for good.

Whatever is going to happen, it will be for good.

Change is the law of the universe."

The Bhagavad Gita (Hindu Scripture).

Chapter 1

Introduction

1.1 A Short History of Ferroelectricity and Piezoelectricity

In 1880 brothers Pierre and Paul-Jacques Curie discovered the existence of piezoelectricity in various crystals like quartz, tourmaline and Rochelle salt.[1,2] This discovery provided the drive for further study in the field of piezoelectrics, notably works done by Walter Cady and Erwin Schrödinger.[3,4] In 1912, Erwin Schrödinger first coined the term "*ferroelektrisch*" or '*ferroelectricity*'.[4] Credit for discovering ferroelectricity goes to Joseph Valasek for his systematic study of the magnetic properties of ferromagnetics and the dielectric properties of Rochelle salt, which he presented at the annual meeting of the American Physical Society in Washington on 23rd April 1920.[5,6] Another major breakthrough in ferroelectric research happened in the early 1940s, during World War II, with the discovery of ferroelectricity in barium titanate ($BaTiO_3$) and other perovskite based materials.[7-9] The discovery of ferroelectricity in $BaTiO_3$ opened up new vistas of application for ferroelectric materials, leading to significant interest in other types of ferroelectrics.[10,11] Since the discovery of ferroelectricity in Rochelle salt 92 years ago, there have been many theoretical and experimental advances in the research area.[11-21] In particular, the last two decades witnessed significant progress in the miniaturisation of electronics components, which resulted in the rapid development of nanoferroelectric research.[12-21]

1.1.1 A Primer on ferroelectric materials

In order to have a better understanding of the data presented in this thesis, the fundamentals of ferroelectric and related materials are presented in this section. All materials undergo a small change in their dimensions when subjected to an external force, such as a mechanical stress, an electric field, or even a change in temperature.[10,22] Depending on the crystal structure of the material, a small

dimensional modification by an electric field, a change in temperature or a mechanical stress can create an electric polarisation change inside the crystal and hence give rise to the occurrence of ferroelectricity, pyroelectricity and piezoelectricity respectively.[10,22] A material's crystal structure must lack a centre-of-symmetry (be "acentric") for it to show piezoelectricity, and be both acentric and possess a unique axis of symmetry (making it a "polar" structure) for it to be pyroelectric. There are 32 crystal classes, and 11 of them possess a centre of symmetry. Of the remaining 21 acentric classes, all except one exhibit a polarisation change when subjected to mechanical stress and hence are *piezoelectric*. Ten of these 20 classes possess a unique axis of symmetry (are polar) and an electric polarisation exists within the structure in the absence of an applied field. The electric polarisation in these polar materials changes with temperature, making them *pyroelectric*.[10,22] As they are acentric, they also show piezoelectric behaviour. *Ferroelectrics* are a subgroup of pyroelectrics, in which spontaneous polarisation within the structure can be switched between different stable directions by an application of an electric field of sufficient magnitude (the coercive field).[10,22] Figure 1.1 depicts the basis of piezoelectricity, pyroelectricity and ferroelectricity.

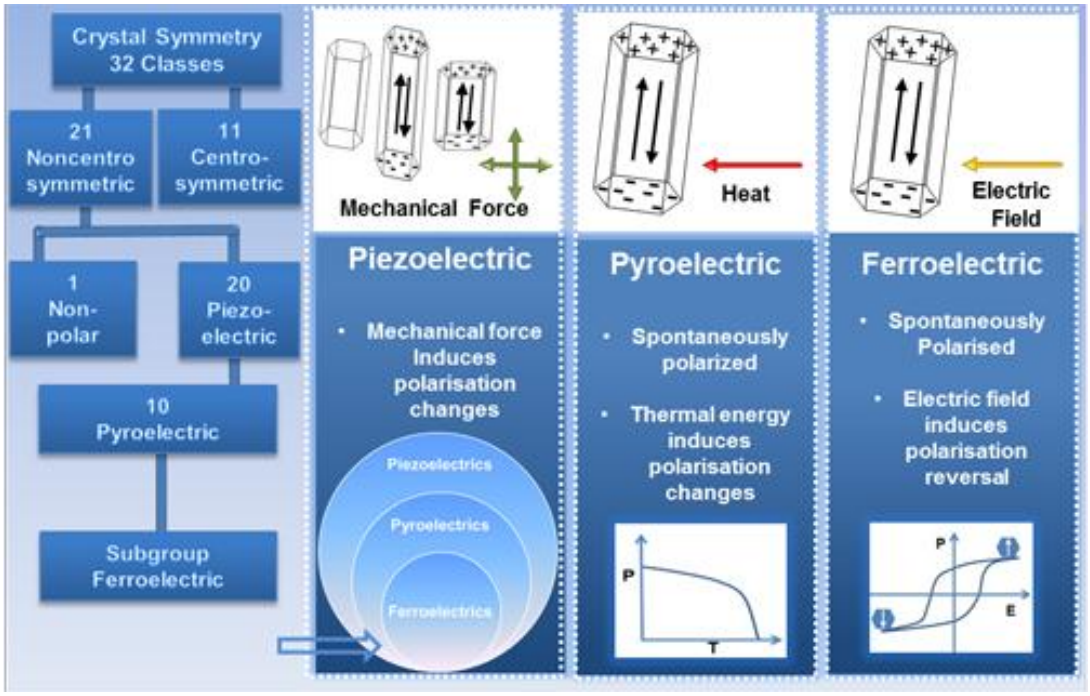

Figure 1.1. Schematic representation of piezoelectricity, pyroelectricity and ferroelectricity on the basis of crystal symmetry (Column 1) and their origin based on the mode of polarisation change occurring inside the material (Column 2-4). Venn diagram in column 2 shows that all ferroelectric materials are pyroelectric and piezoelectric but not vice versa. The graphs in columns 3 and 4 represent the polarisation (*P*) change with respect to temperature (*T*) and electric field (*E*) respectively.

According to the Landolt–Börnstein data base,[23] ferroelectric materials are classified into three major groups comprising of 72 families; according to their chemical composition and crystal structure.[9] These three ferroelectrics groups are (1) inorganic oxides, (2) inorganic non-oxides, and (3) organic crystals, liquid crystals and polymers.[9,23] Among these three groups, the oxide-based ferroelectrics especially the ABO_3 perovskite-type family, are the most extensively studied. Commonly studied ferroelectrics such as barium titanate ($BaTiO_3$), lead titanate

($PbTiO_3$), and lead zirconate titanate ($PbZr_xTi_{(1-x)}O_3$) belong to perovskite family.[9,11,22] Within the non-oxide ferroelectrics, some chalcogenide and chalcohalide-based materials show promising ferroelectric characteristics, *e.g.* zinc cadmium telluride (ZnCdTe)[24], germanium telluride (GeTe)[25] and antimony sulfoiodide (SbSI)[26]. Within the polymer family, polyvinylidene fluoride (PVDF) and its copolymers with trifluoroethylene show excellent ferroelectric and piezoelectric characteristics.[27] A more detailed description of different types of ferroelectric families can be found elsewhere.[9,23]

1.2 Nanoscale Ferroelectrics and Piezoelectrics

Materials in the nanostructured form are central to the evolution of future electronics and information technologies. Ferroelectrics have already been established as a dominant branch in the electronics sector, because of their diverse application range. The on-going dimensional downscaling of materials, to cram more components onto integrated circuits, in turn gives a great boost to the evolution of potential nanostructured ferroelectric materials and devices.[12-21] For instance, memory storage based on ferroelectric polarisation reversal has been predicted as one of the emerging memory technologies[12], owing to their high read-write speed, low power consumption and long rewriting endurance.[28,29]

Size and dimensionality plays a critical role in determining the ferroelectric characteristics of a material at the nanoscale, due to the different ways in which dipoles align in ferroelectric crystals. Since ferroelectricity is a collective phenomenon caused by the arrangement of charge dipoles inside a crystal, an increase in surface area by nano-structuring could trigger immense changes in the long- and short-range ordering of dipoles inside a material. These changes could

alter some of the ferroelectric functionality, such as phase transition temperature or Curie temperature (T_C), domain dynamics, dielectric constant, coercive field, or spontaneous polarisation, piezoelectric response, *etc*., at the nanoscale.[14,21,30-36] In short, low dimensional ferroelectrics show marked deviations in their properties compared to their bulk ferroelectric counterparts, mostly due to the great enhancement of surface area. Since the surface characteristics of nanostructures are morphology and size dependent, the type of nano-structuring used in ferroelectrics must be based on the dependence of some parameter related to the ferroelectric functionality under consideration. This parameter could be crystallinity, alignment, ordering or even surface modification of the ferroelectric nanostructures under consideration.[37]

This introductory chapter reviews some exemplary breakthroughs that outline the progress in research in nanoscale ferroelectric material syntheses, characterisations and applications covering mostly the last decade, with priority given to novel synthetic strategies. The 'bottom-up' and 'top-down' approaches used so far for synthesising nanoscale ferroelectrics of various morphology and structuring will be discussed in detail, whilst highlighting the pros and cons of each synthetic strategies. This section will also address the current efforts in making precisely ordered ferroelectric nanostructures. All of the developments in the synthesis of nanoscale ferroelectrics will not be complete without proper choice of characterisation tools to study the ferroelectric features at the nanoscale, and these techniques will be discussed in the succeeding part of this chapter; focusing on scanning probe based techniques, especially piezoresponse microscopy (PFM), as these are the vital characterisation tools to investigate the ferroelectric and piezoelectric functionality at the nanoscale.[38-47] The concluding section will give a summary on emerging

nanoferroelectric applications and the future outlook of the entire field of nanoferroelectric research.

1.3 Classification of Ferroelectric Nanostructures

Generally nanostructured materials fall into 4 different classes, *viz*. zero-dimensional (0D), one-dimensional (1D), two-dimensional (2D), and three-dimensional (3D) nanostructures.[48] Over the last decade considerable progress in the fabrication of various nanoscale ferroelectric materials, in a number of novel geometries under the above mentioned four categories, has been achieved (Figure 1.2 and Table 1.1).[15-17,19,20,49-51]

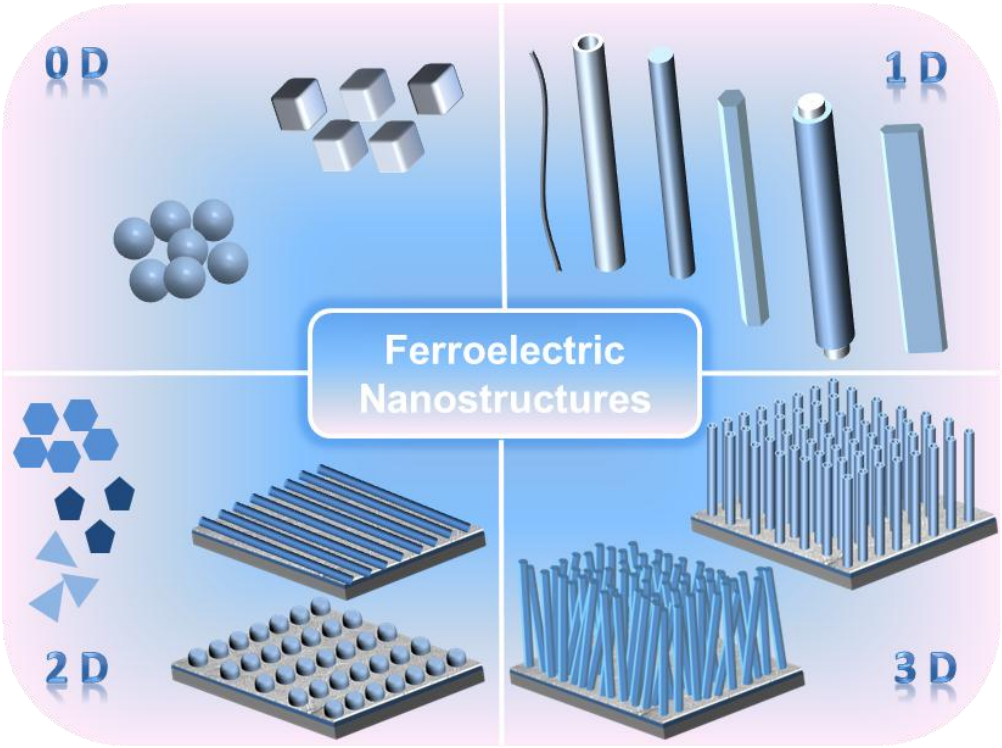

Figure 1.2. Common types of ferroelectric nanostructures; (0D) 'zero-dimensional'- spheres and cubes, (1D) 'one-dimensional'- wires, tubes, rods, core-shell, and belts or ribbons, (2D) 'two-dimensional'- plates and horizontally aligned arrays of dots or wires, and (3D) 'three-dimensional'- vertically aligned nanowire/rod/tube array.

Table 1.1. Survey of some recent developments in the synthesis of ferroelectric nanostructures.

Family	*Compounds*	*Experimental methods*	*Nano-morphology*
Pervoskite	$BaTiO_3$	Sol-gel,[52,53] metal-organic decomposition,[54, 55,56] PLD,[57] hydrothermal,[58-64] supercritical,[65] templated,[52,66-71] electrophoretic deposition,[72] surfactant-assisted,[73] molten-salt,[74-77] FIB,[78-80] electro-spinning.[53]	rod,[55,72,75,77,79] wire,[56,59,66,67,74,80] belt,[74] tube,[52,60,71] cube,[62,64] particle,[54,58,61,65,73] lamella,[78] fibre,[53] torus,[63] dot array.[57,68-70]
	$(Ba,Sr)TiO_3$	Solvothermal,[81,82] templated,[83] sol-gel.[83]	particle,[81,82] tube.[83]
	$NaTaO_3$	Chemical reduction[84]	rod[84]
	$PbTiO_3$, PZT	Hydrothermal,[85,86] PLD,[87] EBL-assisted,[88-91] nanoimprint lithography,[92,93] self-assembly,[94-99] templated,[66,71,87,89,100-105] electro-spinning,[106-108] sol-gel,[89,100,101] molten-salt,[74,76,77] FIB.[109,110]	islands,[94-99] particle,[86] dot,[109] rod,[76,77] wire,[66,74,92,106-108] tube,[71,89,102,103,105] ordered-array.[85,87-91,93,100,101,104,110]
	PLZT	Hydrothermal[111]	hollow sphere[111]
	$SrTiO_3$	Hydrothermal,[59,64] metal-organic decomposition,[55] templated,[52] molten-salt.[74]	cube,[64] rod,[55,75,77] tube,[52] wire.[59,74]
	$K_{0.5}Bi_{0.5}TiO_3$	Hydrothermal,[112] sol-gel.[112]	wire[112]
	$Na_{0.5}Bi_{0.5}TiO_3$	Hydrothermal,[113] sol-gel.[113]	whisker[113]
Layered structure	$Bi_4Ti_3O_{12}$	Templated,[114,115] sol-gel,[114] hydrothermal,[116] solid-state.[115]	rod,[115] tube,[114,115] plate.[116]
	$Bi_{4-x}Nd_xTi_3O_{12}$	Templated,[117] sol-gel.[117]	tube-array[117]
	$Bi_{4-x}La_xTi_3O_{12}$	Electro-spinning,[118] sol-gel,[118] templated[119]	fibre,[118] tube[119]
	$BiFeO_3$	Templated,[120,121] sonochemical.[122]	tubes[120], wires,[121] rod.[122]
Tungsten-Bronze	ε-WO_3	Flame spray pyrolysis[123]	particle[123]
Pyrochlore	$Bi_2T_2O_7$	Templated,[124] sol-gel.[124]	tube[124]
Non-oxides	SbSI	Sonochemical[125]	wire[125]
	$SbS_{1-x}Se_xI$	Sonochemical[126]	wire[126]
	Sb_2S_3	Templated,[127] solvent-less.[127]	wire-array[127]
	GeTe	Solution-phase synthesis[25,128]	particle[25,128]
Polymers	PVDF, P(VDF-TrFE)	Nano-intaglio technique,[129] nano-imprint lithography,[130-132] templated.[133-135]	ordered array,[129-131,133] wire.[132,134,135]

1.4 Fabrication of Ferroelectric Nanostructures

There are two approaches for fabricating ferroelectric nanostructures: 'bottom-up' and 'top down', as highlighted in the following sections. 'Bottom-up' processing refers to the synthesis of nanomaterials starting at the atomic or molecular level. Solution-based routes, *e.g.* sol-gel based chemical solution deposition,[52,53,83,89,100,112,114,117,136] templating,[19,52,66-71] solution-phase decomposition[19,54, 55,56] and hydro/solvothermal synthesis [19,58-64] are the most commonly employed 'bottom-up' approaches for synthesising ferroelectric nanostructures, *i.e.* nanoparticles, nanowires and nanotubes. 'Top-down' processing *e.g.* focused ion beam (FIB) milling[78-80,109,110] and some lithographical methods such as nano-imprint lithography[93,131,132,137,138], consists of carving away at a bulk ferroelectric material to create coherently and continuously ordered nanosized structures.

1.4.1 Zero-dimensional ferroelectric nanostructures

Nanoparticles of different size and shape, such as quantum dots, spheres and cubes were the first experimentally studied ferroelectric nanostructures, due to their size dependence ferroelectric characteristics.[30,139,140] Park *et al.*[30] first reported the decrease in T_C and the increase in the tetragonal crystal distortion of $BaTiO_3$ nanoparticles with decreasing diameter (33 to 140 nm). The researchers also determined that the minimum critical diameter required for a ferroelectric phase transition in the nanoparticles was 37 nm. Since these initial findings on $BaTiO_3$ nanoparticles many different types of ferroelectric nanoparticles have been synthesised by a variety of solution-based methods, as highlighted in the transmission electron microscopy (TEM) images shown in Figure 1.3.

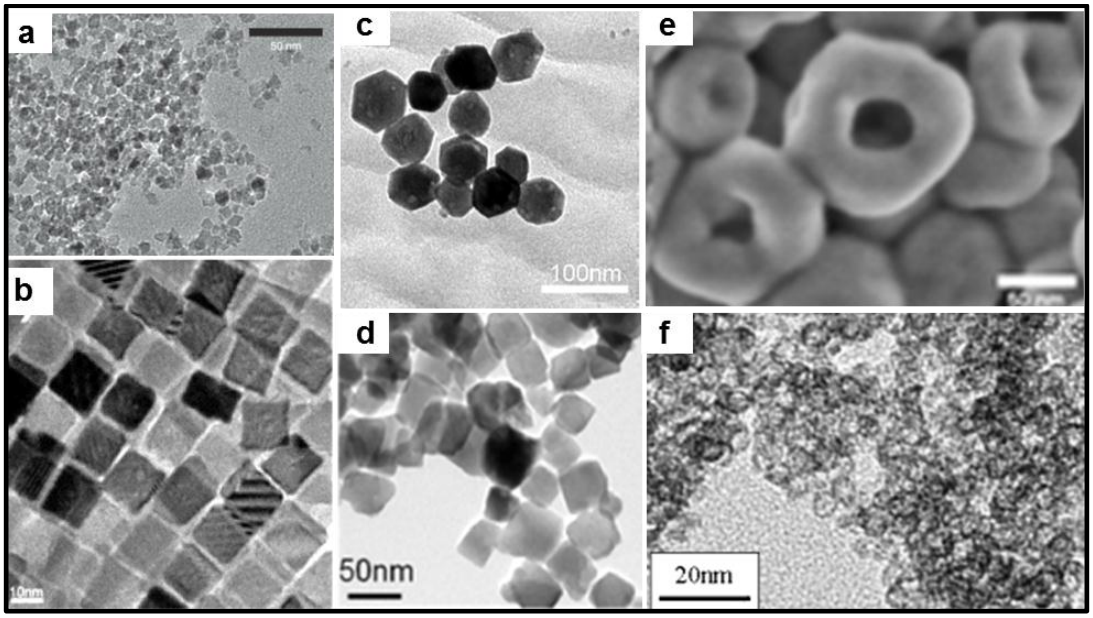

Figure 1.3. TEM images of (a) $BaTiO_3$ nanoparticles (~6 to 8 nm) synthesized at room temperature using a bio-inspired solution-phase metal-organic decomposition,[54] (b) $BaTiO_3$ nanocubes prepared hydrothermally,[62] (c) dodecahedral shaped $BaTiO_3$ nanoparticles prepared by hydrothermal reaction,[61] and (d) cube-shaped $LiNbO_3$ nanoparticles prepared via solvothermal route.[141] (e) SEM image of $BaTiO_3$ nanotorus prepared by hydrothermal reaction,[63] and (f) TEM image of PLZT hollow nanospheres synthesised hydrothermally[111].

Nanoparticles can be synthesised by homogeneous nucleation from a liquid phase.[37] Recently, Ould-Ely *et al.*[54] engineered the large-scale synthesis of $BaTiO_3$ nanoparticles, utilising a kinetically-controlled, vapour diffusion-assisted hydrolysis protocol by which a bimetallic alkoxide precursor, $BaTi(OCH_2CH(CH_3)OCH_3)_6$, decomposed to produce uniform sized (~6 to 8 nm) paraelectric nanoparticles (Figure 1.3(a)), at room temperature; successfully yielding up to 250 ± 5 g $BaTiO_3$ nanoparticles in single batches. Sub 10 nm sized colloidal nanocrystals of germanium telluride (GeTe), the simplest known ferroelectric, was synthesised

recently by the metal-organic decomposition of bis[bis(trimethylsilyl)amino]Ge(II) ($(TMS_2N)_2Ge$) with trioctylphosphine-tellurium (TOP-Te) in the presence of 1-dodecanethiol and excess trioctylphosphine at 230 °C.[25,128] Many groups have successfully synthesised ferroelectric nanoparticles close to their predicted critical size-limit, where ferroelectricity disappears. For instance, Niederberger *et al.*[82] solvothermally prepared ultra-fine $BaTiO_3$, $SrTiO_3$, and $(Ba,Sr)TiO_3$ spherical nanoparticles with a mean diameter of 5 nm. Recently, Xu *et al.*[86] hydrothermally synthesised free-standing lead zirconate titanate (PZT) nanoparticles with diameters ~ 4 nm. Hollow ferroelectric nanostructures are also of interest; for instance, lanthanum doped lead zirconate titanate (PLZT) hollow nanospheres (Figure 1.3(f)) with size as low as 4 nm were prepared hydrothermally. Nanocrystals can be formed in a variety of morphologies, due to differences in the surface energy of crystal facets which are dependent on the reaction environment.[142] Thus the shape and morphology of a nanocrystal can be tuned by altering the surface-energy of a specific crystal facet by selectively adsorbing inorganic or organic ligands onto these facets.[142] This crystal engineering strategy has been successfully applied to the hydrothermal synthesis of dodecahedral shaped $BaTiO_3$ nanoparticles (Figure 1.3(c)), through the selective adsorption of polyethylene glycol (PEG) moieties onto the {110} surface facets of $BaTiO_3$.[61] Adireddy *et al.*[62] have also reported the controlled solvothermal synthesis of mono-disperse, free-standing, $BaTiO_3$ nanocubes with a mean diameter 20 nm (Figure 1.3(b)). They attribute the cubical shape of the as-synthesised $BaTiO_3$ nanoparticles to the preferential formation of {100} planes during the crystal nucleation process. Similarly, cube-shaped $LiNbO_3$ nanoparticles (~50 nm in diameter, Figure 1.3(d)) were synthesised via solvothermal treatment of the single-source precursor, $LiNb(OEt)_6$ by Mohanty *et al.*[141]

1.4.2 One-dimensional ferroelectric nanostructures

Various types of one-dimensional (1D) semiconductor architectures[143,144] have been already demonstrated, ranging from device configurations such as field effect transistors (FET),[145] sensors,[146] to flexible electronics components,[147] *etc*. The numerous potential applications of 1D semiconductor nanostructures arise from their geometries, which can be readily manipulated.[143,148,149] Recently, Weber *et al.*[150] fabricated Si nanowires with dimensions only one atom tall and four atoms wide, with remarkable low resistivity values (~0.3 mΩ. cm), comparable to the current carrying capabilities of copper.

One-dimensional ferroelectric nanostructures (nanowires, rods, tubes, belts) are the most extensively studied nanostructures due to their size-driven ferroelectric behaviour[17,19] Among the 1D ferroelectrics, pervoskite-structured ternary oxides of ABO_3 type, *e.g.* $BaTiO_3$, $PbZr_{1-x}Ti_xO_3$, $SrTiO_3$, are the most extensively investigated material due to their excellent ferroelectric characteristics.[17,19] Although $PbZr_{1-x}Ti_xO_3$ nanowires were the first 1D structures to be synthesised,[151,152] $BaTiO_3$ nanowires were the 1D ferroelectric studied for its size-dependent ferroelectric behaviour[55,56,153]. Urban[56] and Yun[153] *et al.* demonstrated that $BaTiO_3$ nanowires with diameters as small as 10 nm displayed ferroelectric behaviour.

Significant progress has been made recently in the synthesis and characterisation of many 1D ferroelectric nanostructures with various morphologies.[17,19] The most commonly adopted techniques towards the realisation of 1D ferroelectrics are, 'bottom-up' routes such as template-based synthesis,[52,83,89,100,114,120,121] hydro/solvothermal synthesis,[60,112,154,155] molten-salt synthesis,[74-77] solution-based metal-organic decomposition,[55,56] and electrospinning[53,118]. Among the 'top-down' approaches, methods such as focus ion beam (FIB) milling,[80] and nanoimprint

lithography[92,137,138,156,157] have largely been employed. Figure 1.4 shows SEM and TEM images of different forms of pervoskite-based ID ferroelectric nanostructures synthesised recently by various methods. The synthesis routes to 1D ferroelectric nanostructures can be grouped into two different categories: (i) template-free synthesis, and (ii) template-assisted synthesis.

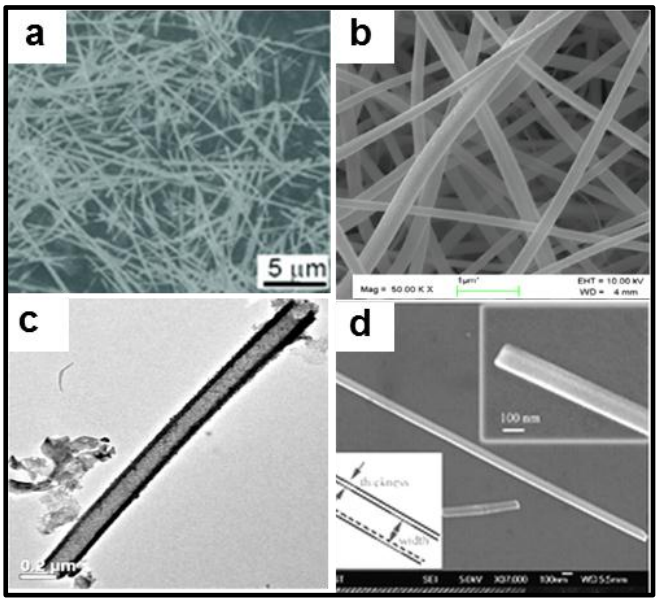

Figure 1.4. SEM images of (a) $NaNbO_3$ nanowires synthesised by a hydrothermal method,[155] and (b) $BaTiO_3$ nanofibers made by sol-gel assisted electro-spinning.[53] (c) TEM image of an isolated $BaTiO_3$ nanotube made using an anodic aluminium oxide template[52] and (d) SEM image of a $BaTiO_3$ nanostrip synthesised by a molten-salt method[74].

1.4.2.1 Template-free synthesis of 1D nanoferroelectrics

Hydro/solvothermal synthesis has been effectively utilised for synthesising complex pervoskite ferroelectric nanowires and tubes, owing to the homogeneous mixing of individual reactants under subcritical conditions.[60,112,154,155] This approach

facilitates the easy diffusion and homogeneous nucleation of the reacting species and allows the formation of highly crystalline stoichiometric materials at low temperatures.[158] For example, highly crystalline $NaNbO_3$ nanowires (Figure 1.4(a)) were synthesised by the hydrothermal reaction of NaOH and Nb_2O_5 at crystallisation temperature as low as 150 °C.[155] In hydrothermal reactions, the size, morphology and crystallinity of a material can be tuned by varying parameters such as reaction temperature, duration, solvent type, surfactant type and pH of the solution.[158] For instance, Magrez *et al.*[154] studied the evolution of 1D $KNbO_3$ nanostructures through various morphologies by adjusting the reaction temperature and concentration of the precursors used. Although hydrothermal routes for synthesising 1D nanostructures have many advantages, such as low temperature synthesis, homogeneous nucleation, narrow particle-size distribution, controlled morphology and high crystallinity, there are a number of synthetic disadvantages, which include the need for expensive autoclaves, safety issues and long reaction times. All of these drawbacks put constraints on scalability of hydrothermal methods for synthesising bulk quantities of nanoscale materials.[158]

The decomposition of metal-organic precursors in solution is another approach employed for synthesising ferroelectric nanorods and wires. Urban and co-workers[55] synthesised well-isolated single crystalline nanorods of $BaTiO_3$ and $SrTiO_3$ (diameters ranging from between 5 to 60 nm and length up to 10 μm), by the solution-phase thermolysis of barium titanium isopropoxide ($BaTi[OCH(CH_3)_2]_6$) and strontium titanium isopropoxide ($SrTi[OCH(CH_3)_2]_6$ in the presence of oleic acid respectively. The oleic acid coordinates with the precursor molecule to form an elongated inverse micelle structure in the reaction medium, which subsequently decomposed at high temperatures to form anisotropic nanorods.[55] Although

organometallic decomposition methods can produce high quality 1D ferroelectric nanostructures with narrow diameter distribution, the air-sensitive nature of the precursors and relatively low product yields can be a hindrance. Another solution-based approach for producing 1D ferroelectric material is molten-salt synthesis, which has used for the large scale production of nanoferroelectrics.[74-77] This method involves the reaction of precursors in a molten salt medium, such as NaCl or KCl melt, which leads to the precipitation of the nanostructures. Molten-salt synthesis can be carried out over short time duration (1 to 4 hours) using common salts of constituent materials, making this approach more facile and environmentally benign compared to hydro/solvothermal methods.[74-77] The basic formation mechanism of nanostructures by molten-salt methods is dependent on the control of surface and interface energies of precursors and salt used; different morphologies can be formed by varying the salt or precursor concentrations.[74-77] 1D nanostructures of common ferroelectrics such as $BaTiO_3$ (Figure 1.4(d))[74], $SrTiO_3$, and $PbTiO_3$ have been synthesised by this method.[74-77] Electrospinning has also been used to produce high aspect ratio 1D nanofibers and wires of ferroelectric materials,[53, 106-108,118] *e.g.* $BaTiO_3$ nanofibers (Figure 1.4(b))[53]. Other less common techniques, such as sonochemical synthesis[125,126,159, 122] and electrophoretic deposition[72], have also been employed for the synthesis of ferroelectric nanowires and nanorods.

Ramesh *et al.*[160,161] introduced the concept of focus ion beam (FIB) milling for the 'top-down' fabrication of ferroelectric nanostructures. Later on, Marshall *et al.*[162] fabricated PZT nanocapacitors with surface areas ranging from 6×10^{-14} m^2 to 3×10^{-12} m^2 in the form of circular capacitors with lateral diameters between 90 nm and 2 μm using FIB milling. Schilling[80] and McQuaid[79] *et al.* adopted this technique to fabricate nanocolumns of $BaTiO_3$ from single-crystal barium titanate by a 'top-

down' method (SEM images of $BaTiO_3$ nanocolumns and a detailed scheme of the FIB processing is shown in Figure 1.5)[80]. Although this technique is time consuming, it has the advantage of user-defined morphological control of the nanostructures produced.

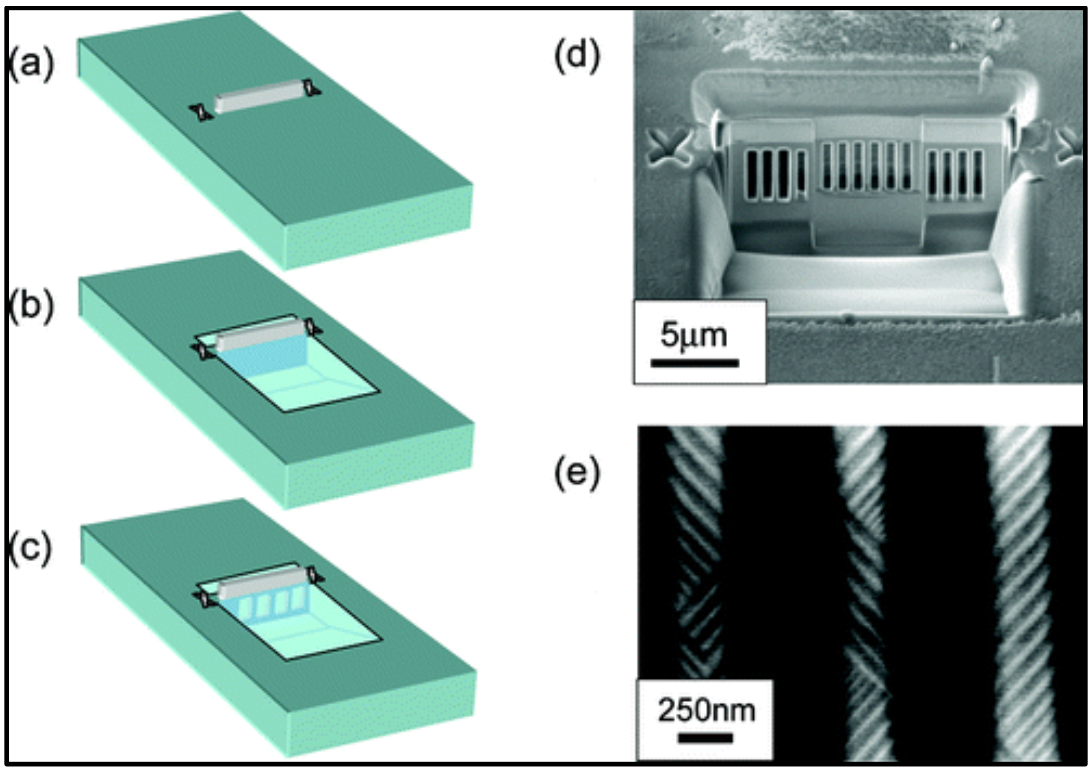

Figure 1.5. Schematic diagrams (a) to (c) illustrating a FIB processing method to cut nanoscale lamella into $BaTiO_3$ single-crystalline nanowires. First, a protective Pt bar is deposited by the local ion-beam induced breakdown of Pt-based organic precursor gases between two alignment crosses (a). Automated software allows the milling of trenches on either side of a $BaTiO_3$ lamella (b), and the sample is then reoriented to allow milling into the lamellar face to leave columns of material, as shown in the schematic illustration in (c). (d) SEM image of the $BaTiO_3$ columns and (e) STEM imaging using a high-angle annular dark field detector reveals distinct contrast from stripe domains.[80]

1.4.2.2 Template-assisted synthesis of 1D nanoferroelectrics

In 1994 an article published in *Science*[163] by Charles R Martin highlighted the potential of using 'template-based synthetic approaches' to realise various types of nanoscopic materials, including polymers, metals and semiconductors. Template-directed 'bottom-up' synthesis has been proven as the most successful and facile strategy in making 1D ferroelectrics so far. Materials with nanosized vertical or horizontal channel structure, such as anodic aluminium oxide (AAO), track-etched polymer membranes, self-assembled block copolymer films and porous silicon, have been used as templates for synthesising 1D nanostructures.[163] The channels in the templates act as nano-moulds, whereby the precursor is impregnated into the pores of the template by suitable methods such as electrodeposition, solution or vapour phase deposition, and subsequently the precursor is decomposed to form 1D nanostructures.[163] The template can then be completely removed or partially etched to form isolated or arrays of 1D nanostructures. The major benefit associated with template synthesis is that the physical dimensions of 1D nanostructure can be precisely controlled, simply by varying the pore-diameter and length of the channels of the template employed. Moreover, mono-disperse nanostructures can be harvested in large quantities owing to the high pore density (between 10^9 and 10^{12} pores per cm^2) present in the templates.[163] However, templates must meet certain processing conditions if they are to be used in the synthesis of 1D ferroelectric nanostructures, *e.g.* chemical and thermal inertness, uniformity of the porous channels and the easy release of the nanostructures from the template channels.[37,164] In this regard, anodic aluminium oxide (AAO) template satisfies most of the above mentioned requirements and is the most widely used template for the generation of 1D nanostructures.[165] AAO membranes have a high density of hexagonally ordered

cylindrical channels (or pores) aligned perpendicular to the membrane plane (Figure 1.6(a-c)) and these pores can act as templates for the fabrication of 1D ferroelectric nanostructures.

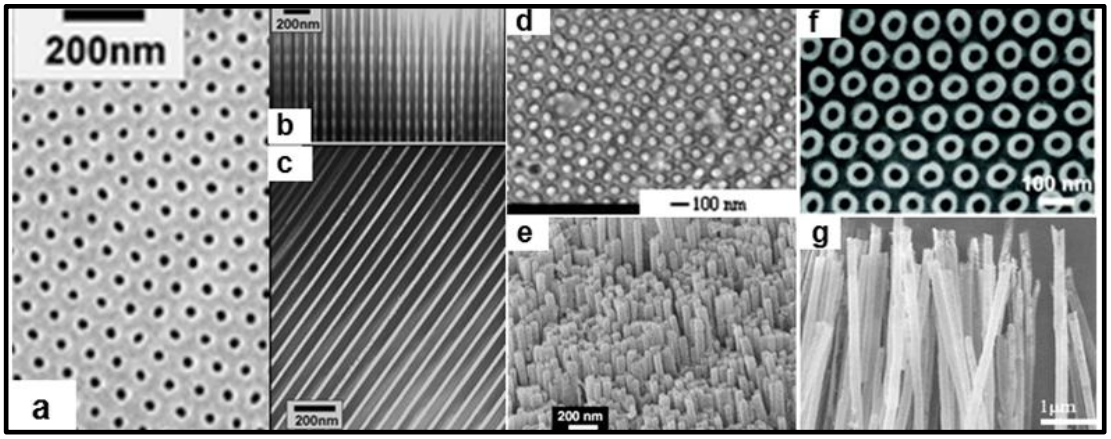

Figure 1.6. (a) Plan-view SEM image of an AAO template showing hexagonally ordered pores, (b) and (c) cross-sectional TEM images of same AAO memebrane showing vertically aligned pore channels.[166] (d) Plan-view SEM image of an AAO template filled with PZT nanowires,[100] (e) side-view SEM images of free standing arrays of $BiFeO_3$ nanorods after dissolving the AAO template,[121] (f) plan-view SEM image of an AAO template filled with PZT nanotubes,[103] and (g) Nd-doped $Bi_4Ti_3O_{12}$ nanotubes liberated after dissolving the AAO template[117].

In 2002, Hernandez *et al.*[136] explored the potential use of AAO templates to synthesise pervoskite oxide-based 1D nanostructures such as $BaTiO_3$ and $PbTiO_3$ nanotubes by a sol-gel assisted method. The method was so simple that the permeation of the precursor sol into the pores of the AAO templates was achieved by just dipping the template in the sol for 1 minute, followed by drying and calcination. Following the success of this method, many ferroelectric materials have been synthesised in 1D form by AAO templating, ranging from classic Rochelle salt[167] to

many oxide based ferroelectrics (Figure 1.6(d-g))[52,100,102,103,105,121,124] and polymer ferroelectrics such as polyvinylidene difluoride (PVDF)[132,134,135]. Solution-based synthesis in conjunction with AAO templating is the most widely approach for producing 1D nanostructures,[52,100,102,103,121,124] although methods such as electrodeposition[66,72] have also been used. 1D nanostructures such as nanotubes, wires or rods can also act as 1D templates; either as a reactive template (where the template itself is incorporated into the final product by a suitable reaction) or a passive template (where the template is non-reactive and can be etched away after the reaction).[165] For example, TiO_2 nanowires and Bi_2O_3 nanorods have been used as reactive templates for the synthesis of $BaTiO_3$ nanowires[67] and $Bi_4Ti_3O_{12}$ nanorods/tubes[115], by treating the templates with $BaCO_3$ and a Ti(IV) peroxocomplex respectively. In a different method, PZT and $BaTiO_3$ nanotubes were prepared using passive templates such as Si and ZnO nanowires, where these sacrificial nanowire templates were etched after the deposition of the material.[168] More extensive information on the synthesis and characterisation of 1D nanoferroelectrics can be found in recent reviews by Handoko[17] and Rørvik[19] *et al.*

1.4.3 Two-dimensional ferroelectric nanostructures

Planar structures such as plates[116] or lamella[78] and lateral arrays of nanodots[87] or wires[92] constitute the two-dimensional (2D) nanoferroelectric family. The formation of periodic arrays of isolated ferroelectric nanoislands or dots has already been shown to enhance the performance of ferroelectric random access memories (FeRAM), by providing a high density of ferroelectric single-domains per unit area.[87,169] Different forms of 'top-down' and 'bottom-up' routes, such as electron beam lithography (EBL), nanoimprint lithography (NIL), self-assembly and

template-assisted synthesis, have been used for the geometrical patterning of 2D nanoferroelectrics.

Alexe *et al.*[90] pioneered research on the 2D arrangement of ferroelectric nanostructures for their potential use in high density ferroelectric memories. The researchers used EBL for the 'top-down' fabrication of regular arrays of $SrBi_2Ta_2O_9$ and PZT nanoisland capacitors with lateral dimensions ~100 nm.[90] Huang *et al.*[91] also fabricated well-ordered PtO_x/PZT/PtO_x arrays of capacitors, down to a cell size of 90 × 90 nm, using EBL and plasma etching with a photoresist mask. Clemens *et al.*[88] have produced polycrystalline arrays of $PbTiO_3$ nanoislands (lateral dimensions ~50 to 100 nm) using EBL assisted synthesis. Nguyen and co-workers demonstrated the wafer-scale production of laterally ordered 40 nm PZT nanowires, using a 'photolithography and etching for nanoscale lithography' (PENCiL) technique.[170] This PENCiL method made use of a Ni nanowire array mask to generate horizontally aligned PZT nanowire array. Dip-pen lithography[171] is another way of producing nanopatterns and was used in the fabrication of array of $PbTiO_3$ nanodots, with a minimum lateral dimension of ~37 nm on a Nb-doped $SrTiO_3$ substrate.[172] This method utilised the position control capabilities of an atomic force microscope (AFM) cantilever to produce patterns of ordered nanostructures.[171] Although the lithographic fabrication of nanostructures allows pre-defined precise positioning and morphological control of these structures, drawbacks such as high time consumption and complex etching process involved make it a less prevalent route for making 2D nanoferroelectrics.

NIL has emerged as a facile and high-throughput patterning technology for fabricating geometrically ordered nanostructures, in which the surface patterns of a template are replicated into a material by mechanical contact followed by de-

moulding.[137] This method has the capability of achieving sub 20 nm structures with precise position.[137] The process of making arrays of wires and dots of nanostructures using a NIL method is schematically demonstrated in Figures 1.7(a)[92] and 1.7(d)[130]. Harnagea and co-workers reported seminal work on NIL processing of ferroelectric nanostructures, fabricating arrays of submicron sized (~ 300 nm) ferroelectric PZT cells.[173] Hu *et al.*[130] adopted nanoimprinting technique for the realisation of high density (~33 Gbits $inch^{-2}$) regular arrays of poly(vinylidene fluoride-trifluoroethylene) [P(VDF-TrFE)] nanocells for non-volatile memory applications (Figures 1.7(d) and 1.7(e)). Subsequently the NIL technique has been extended to fabricate arrays of PZT nanowires[92,156] (Figures 1.7(c) and 1.7(d)) and gratings[93,157] using sol-gel precursors. The great potential of nanoimprinting to produce a variety of geometrically ordered ferroelectric nanostructures has yet to be explored.

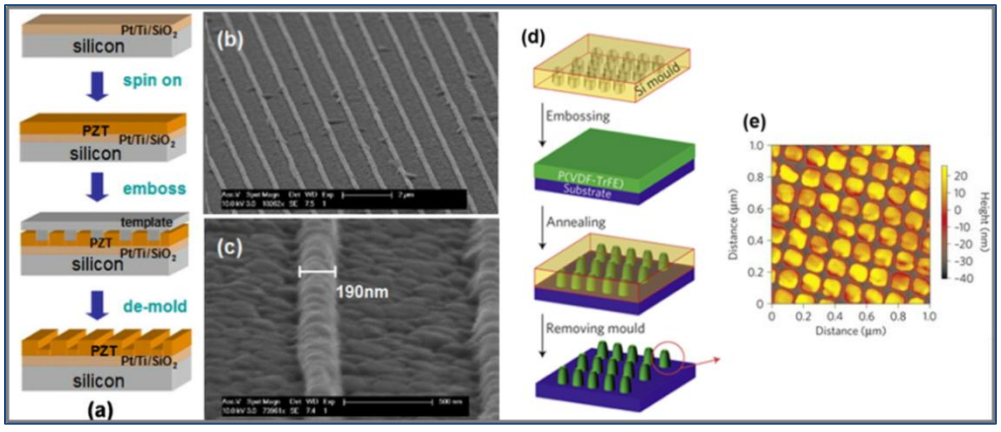

Figure 1.7. (a) Schematic illustration of nanoembossing process of making ferroelectric PZT nanowire arrays, (b) SEM image showing horizontally aligned PZT nanowire arrays and (c) a single PZT nanowire with width of 190 nm.[92] (d) Schematic diagram of the nanoimprinting process of P(VDF-TrFE) copolymer nanocell arrays and (e) AFM topography image of P(VDF-TrFE) copolymer nanocell arrays.[130]

Among the 'bottom-up' approaches, self-assembly-based chemical solution deposition (CSD) has been regarded as the simplest route for the preparation of 2D array of ferroelectric materials.[94-99,174] For instance, Szafraniak *et al.*[94,97] prepared single-crystalline PZT nanoislands (20 to 200 nm in lateral dimensions) by a self-patterning CSD method based on the instability of ultrathin PZT films on a niobium-doped $SrTiO_3$ substrate. The researchers observed that the annealing temperature, substrate interface and surface defects played a crucial role in the formation of PZT nanoislands.[94-97,174] Although self-assembly methods have been successfully employed in making isolated ferroelectric nanostructures of smaller dimensions than those produced by optical lithography, its incapability to achieve geometrical ordering and a narrow size distribution of the nanostructures make this technique less prevalent.

Template-assisted 'bottom-up' synthetic approaches provide a route to achieving 2D geometrical ordering of ferroelectric nanostructures, with narrow size distributions.[37] Nanosphere lithography (NSL)[175] has been demonstrated as a versatile template-based method for generating 2D ferroelectric nanostructures.[68-70,104,176-178] NSL processing consists of two steps: (i) deposition of the desired material inside the void space created by self-assembled monodisperse nanospheres, such as polystyrene latex spheres, and (ii) dissolution of the spheres resulting in ordered arrays of 2D nanoparticles.[175] In NSL, the spacing and size of the periodically arranged nanostructures can be readily controlled by using polymer spheres with different diameters, and/or by changing the amount of material deposited,[69,175] *e.g.* 2D patterned arrays of ferroelectric pervoskite nanodots of $BaTiO_3$ (Figure 1.8),[68-70] PZT[177] and $SrBi_2Ta_2O_9$[68,70], with variable dimensions and coverage density, have been created by NSL techniques in conjunction with pulsed laser deposition. In

addition, NSL can be used to fabricate nanosized electrodes on top of ferroelectric thin films for producing arrays of nanoscale capacitors.[104]

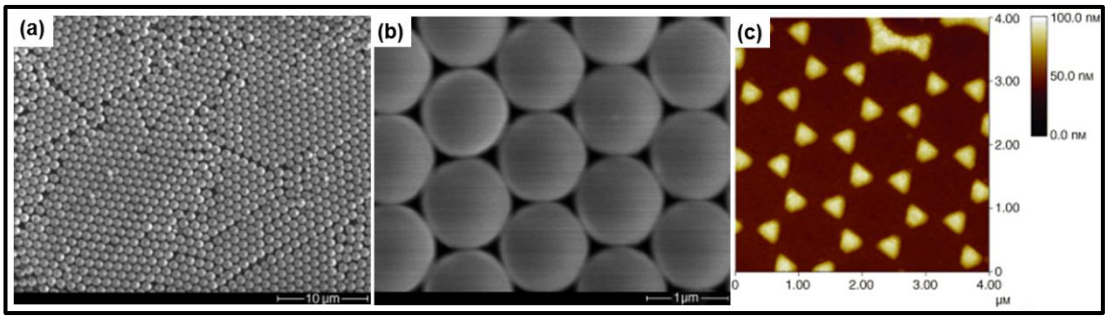

Figure 1.8. (a) Low magnification and (b) high magnification SEM images of 1 μm diameter latex sphere monolayer template, used as a mask for the pulsed laser deposition of $BaTiO_3$ and (c) AFM topography image showing ordered arrays of $BaTiO_3$ nanopyramids (after annealing) obtained using a 1 μm diameter latex sphere monolayer mask.[69]

Although NSL has been successful utilised for nanopatterning arrays of 2D ferroelectric materials, it is difficult to deposit multilayers of materials from the same template.[49] Since high temperature annealing is required for the crystallisation of oxide ferroelectrics, the use of polymer spheres is also not possible for multilayer deposition. These problems have been rectified by the use of thermally stable templates, such as a silicon nitride shadow mask,[179,180] AAO membranes[87,181,182] and gold nanotube membranes,[183] as nanostencil masks for the fabrication of 2D arrays of nanodots. Due to the high thermal stability and inertness of these templates, they have the capability of allowing the multilayer deposition of nanomaterials. Pulsed laser deposition (PLD) has commonly been used for the controlled deposition of ferroelectric materials through nanostencil masks.[179] For example, Lee *et al.*[87]

demonstrated the use of ultrathin AAO membranes as a stencil mask for the fabrication of arrays of PZT nanodots on Pt/MgO substrates by PLD. After the deposition of PZT, a layer of platinum metal was deposited on top of the nanodots, while keeping the AAO mask in place, to form Pt/PZT/Pt structures. Using this approach the researchers were able to fabricate arrays of individually addressable Pt/PZT/Pt nanocapacitors with a coverage density of 176 Gb inch^{-2}, for potential use in ultrahigh-density ferroelectric memories.

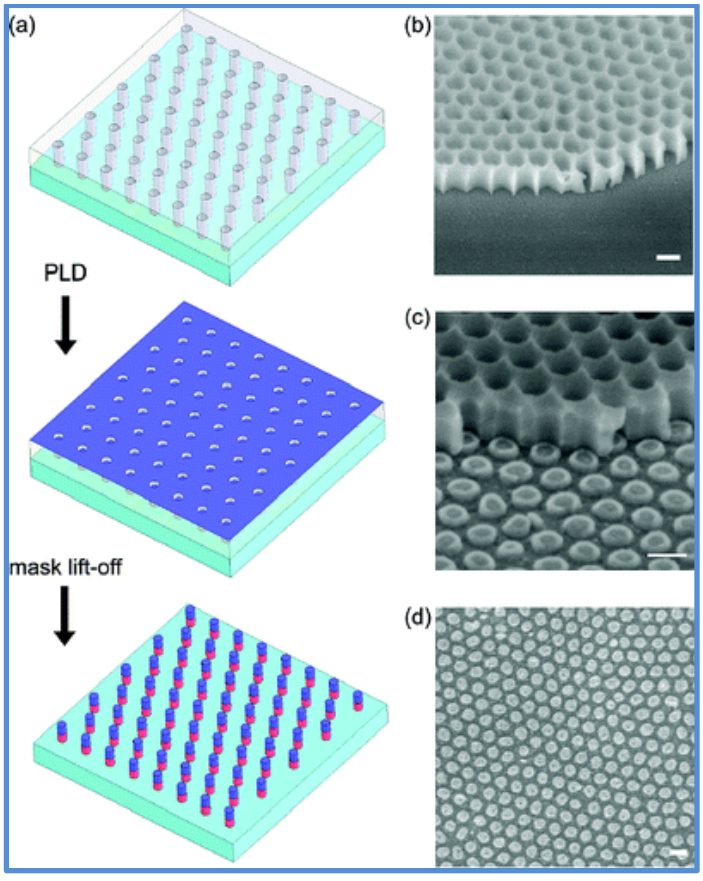

Figure 1.9. (a) Schematic illustration of AAO stencil-based nanofabrication of $BaTiO_3/CoFe_2O_4$ multi-layered arrays of nanodots formed by pulsed laser deposition (PLD). SEM images of (b) as-transferred AAO mask onto a STO substrate, (c) $BaTiO_3$ nanodots with partially removed AAO after first layer deposition and (d) $BaTiO_3/CoFe_2O_4$ two-layered nanodot arrays. The scale bars shown are 100 nm.[57]

Multilayer deposition can also be used to combine functionalities of different materials, *e.g.* Lu *et al.*[57] fabricated $BaTiO_3/CoFe_2O_4$ ferroelectric/ferromagnetic (magnetoelectric) multi-layered arrays of nanodots in order to couple the ferroelectric and ferromagnetic properties of these materials. The process of making arrays of $BaTiO_3/CoFe_2O_4$ nanodots is schematically illustrated in Figure 1.9.[57] AAO stencil-based nanofabrication also finds use in the patterning nanoelectrodes on ferroelectric thin films,[57] *e.g.*, $BiFeO_3$ thin film nanocapacitors have been fabricated by depositing Pt onto a 90 nm thick BFO thin film, pre-deposited on a $SrTiO_3$ substrate with a $SrRuO_3$ top electrode layer, through a AAO mask to form Pt nanoelectrodes with a thickness of 25 nm and diameter 380 nm.[184,185]

The self-assembly of block copolymers (BCPs) is another template-based fabrication route to achieve 2D ordering of nanostructures.[186,187] BCPs consisting of at least two or more distinct homopolymers linked end to end through covalent bonds. When dissolved in a selective solvent of one of the blocks, block copolymer micelles are observed that consist of a core formed by insoluble blocks surrounded by a corona of soluble blocks. Due to thermodynamic incompatibility and chain connectivity, the phase separation between two (or more) blocks in a BCP occurs only in nanometre range (~5 to 50 nm). Depending on the self-assembly conditions and nature of the individual polymer blocks, organised patterns with various geometries (sphere, cylinder, and lamellar) are possible to form. Under appropriate conditions, BCPs self-assemble or phase-separate to form ordered nanoscale patterns, such as aligned cylinders and lamellas, of constituent blocks with a domain spacing that depends on the molecular weight, segment size and the strength of interaction between the polymer blocks.[186-188] Metal ions and organics can be selectively incorporated into one or both blocks of these self-assembled BCP films, which could be used for the

fabrication of functional nanostructure patterns. For instance, nanodot and nanowire arrays with high periodicity can be fabricated on various substrates. The feature size and shape of the patterns are mainly controlled by many parameters, especially: chemical composition and molecular weight of the blocks, solvent type, and annealing conditions. This can be used to tune to the size and shape of the nanostructures. Kang *et al.*[133] used a polystyrene-*b*-poly(ethyleneoxide) (PS-*b*-PEO) di-block polymer template for the confined crystallisation of the ferroelectric polymer PVDF-TrFE into trenches, which were 30 nm in width and 50 nm in periodicity. Kim *et al.*[101] fabricated high density array of epitaxial $PbTiO_3$ nanoislands with a height of 7 nm and a diameter of 22 nm on a single-crystalline Nb-doped $SrTiO_3$ (100) substrate over a large area (cm^2) by utilising the DSA of the polystyrene-*b*-poly(4-vinylpridine) copolymer. Recent developments in BCP-assisted patterning of nanostructures suggests that these templates have the potential to form well aligned and precisely positioned 2D patterns at sub 10 nanometre scales.[189-191] BCP-based fabrication opens up immense prospects for the production of laterally-ordered ferroelectric nanopatterns. Other techniques such as FIB processing,[78,109,110,162] single ion irradiation,[192] and solution-based synthesis[116,128] have also used for the preparation of 2D nanoferroelectrics.

1.4.4 Three-dimensional ferroelectric nanostructures

The ability to order and align ferroelectric or piezoelectric nanostructures, especially nanotubes and nanowires, into high-density free-standing arrays is highly useful for commercial applications.[85,193-196] For example, vertically aligned arrays of PZT nanowires (Figure 1.10(a)) prepared via hydrothermal synthesis, finds application as mechanical to electrical energy converters.[85] Under the application of an uniaxial

compressive force, these PZT nanowires generate a piezoelectric field which in turn produces an electrical output.[85]

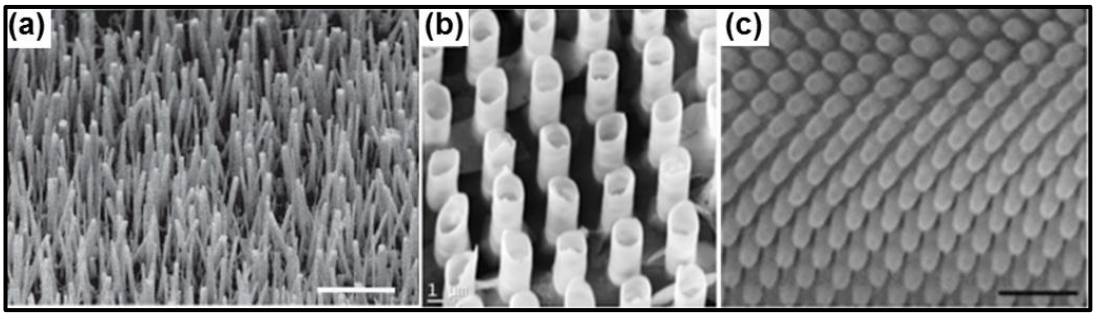

Figure 1.10. SEM images of (a) epitaxially grown arrays of PZT nanowires on an Nb-doped STO substrate by hydrothermal decomposition[85] (scale bar, 5 μm), (b) arrays of PZT nanotubes on a porous Si template produced by metalorganic-decomposition[102] and (c) array of PZT nanotubes fabricated via soft-template infiltration[89] (scale bar, 500 nm).

Scott *et al.*[102] noticed intense terahertz emission from vertically aligned arrays of PZT nanotubes (Figure 1.10(b)), while such emission was totally absent in flat PZT films or bulk. They attributed this effect to the vertical alignment of the nanotubes.[102] Hong *et al.*[132] noticed a five times enhancement in the piezoelectric response for PVDF–TrFE nanostructures aligned perpendicular on a Si substrate compared to PVDF–TrFE thin films. 3D nanostructuring also provides an opportunity to study the size and morphology dependence of ferroelectric characteristics. For instance, Bernal and co-workers fabricated well-ordered free standing arrays of PZT nanotubes (Figure 1.10(c)) by vacuum infiltration of a sol-gel precursor solution into a polymeric template, created using electron beam lithography, and studied the effect of the critical thickness of the nanotubes on their

ferroelectric behaviour.[89] This template-based method[89] has the advantage of precise control over the size, shape and location of the nanostructures, enabling fabrication of NEMS and energy harvesting devices.[193] Other methods such as hydrothermal synthesis,[197-199] PLD[200] and AAO template-assisted fabrication[100,103,121,201] have also been used to prepare 3D ferroelectric nanostructures.

1.5 Characterisation of Nanoscale Ferroelectric Materials

Although there have been numerous research articles published on the fabrication of ferroelectric nanostructures, only a few studies have focused on size-dependent ferroelectric characteristics. A significant understanding of nanoscale ferroelectricity amongst researchers evolved with the advent of scanning probe microscopy (SPM) and piezo-response microscopy (PFM) techniques.[38,39,202,203] Other characterisation tools such as high resolution TEM,[80,109,178,204-207] synchrotron x-ray scattering,[32] scanning probe Raman[45,47] and dielectric spectroscopy[42-44] have also been utilised to probe scaling effects in ferroelectric nanostructures. This section will provide an overview of the latest developments in the characterisation nanoscale ferroelectrics.

PFM has been the pivotal characterisation tool for probing nanoscale materials due to its ability to locally image, quantify and manipulate ferroelectric features of individual nanostructures.[38,39,202,203] PFM uses a conducting AFM tip to measure the local electromechanical response of a ferroelectric material. An applied voltage through the conducting tip on to the surface of the ferroelectric surface causes local deformation of the sample due to converse piezoelectric effects. The tip deflects in response to this deformation, which is then translated into local piezoresponse and phase images. The images obtained provide a qualitative picture of the

piezoresponse and domain structure of individual nanostructures. The quantification of a piezoresponse from an individual nanostructure is possible through the application of switching-spectroscopy PFM.[40,208] This operational mode of PFM is used to locally switch the polarisation, and acquire the resulting local switching hysteresis, of a ferroelectric nanostructure. Put together, the main uses of PFM are (i) to measure a piezo-response, (ii) ferroelectric domain imaging and patterning, (iii) to study domain dynamics and phase transformations and (iv) local polarisation switching and mapping, at the nanoscale.[33, 34, 191, 192] The major applications of PFM are illustrated in Figure 1.11 (adopted from Lee *et al.*[87]). PFM has also been used extensively to study and understand the mechanisms of nanoscale ferroelectric domain growth.[39,202,203,209,210] For example, Rodriguez *et al.* investigated the domain switching dynamics[211] and polarisation states[182] in PZT nanoislands and nanodots using PFM phase image mapping. Although PFM is a versatile and easy to use technique, its spatial resolution both in terms of PFM tip size and electric field spread, may limit its use for the smallest nanostructures of interest.[14] Recently, efforts have been made to increase the spatial resolution regime of PFM.[41,212] Maksymovych *et al.*[41] acquired remnant piezoresponse hysteresis loops from epitaxial $BiFeO_3$ thin films with dimensions as small as 4 unit cells (1.6 nm) using PFM in ultra-high vacuum.

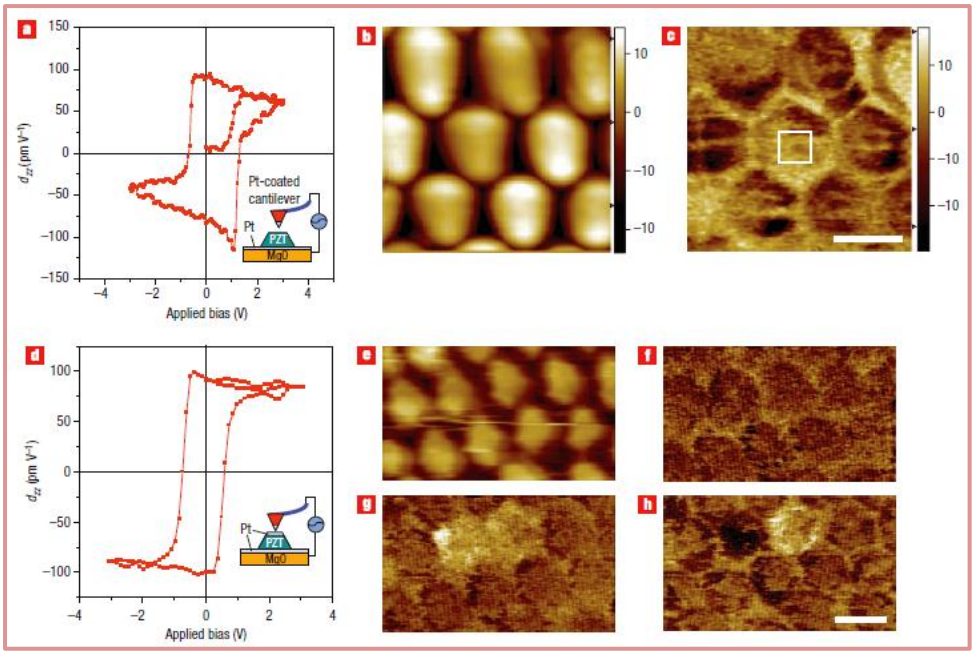

Figure 1.11. (a) Piezoelectric hysteresis loop obtained from epitaxially grown PZT on a Pt/MgO(100) substrate, (b) topographic and (c) piezoresponse images of nanoisland PZT/Pt/MgO(100). The hysteresis loop shown in (a) was obtained from the area marked by a white rectangle in (c). (d) Piezoelectric hysteresis loop obtained from a ferroelectric [Pt/PZT/Pt/MgO(100)] nanocapacitor, and (e) a topographic image of the corresponding sample. PFM images (f) before switching, (g) after positive switching of two capacitors by applying $+3V_{dc}$, and (h) after negative switching of one of the two previously switched capacitors by applying $-3V_{dc}$. Insets in (a) and (d) represent the switching measurement configuration. The scale bars in (b), (c) and (e–h) are 100 nm.[87]

High-resolution TEM offers atomic-scale resolution for investigating ferroelectric polarisation domains and switching mechanisms.[80,109,178,204-207] Nelson *et al.*[206] used aberration-corrected TEM combined with SPM for *in-situ* monitoring of the kinetics and dynamics of ferroelectric switching in $BiFeO_3$ thin films, at millisecond temporal and sub-Ångström spatial resolution (Figure 1.12).

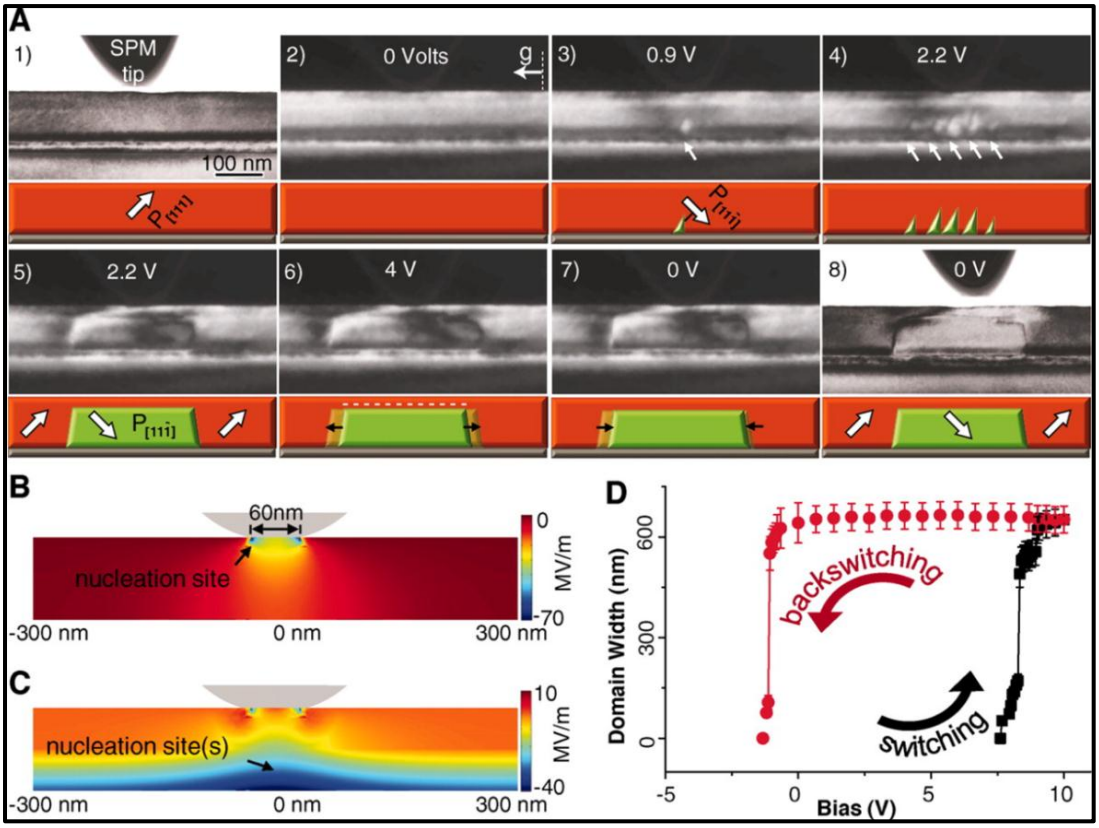

Figure 1.12. (A) Chronological TEM dark-field image series obtained from a single-domain $BiFeO_3$ thin film formed on a $La_{0.7}Sr_{0.3}MnO_3$ (electrode)/$TbScO_3$ substrate. Nucleation occurs at the $La_{0.7}Sr_{0.3}MnO_3$ electrode interface at 0.9 V (images 1 to 3), producing a metastable stationary domain. Additional bias increases the size and number of these domains up to 2.2 V (image 4). At 2.2 V, the domains merge and propagate forward just short of the surface (image 5), where they remain pinned along a (001) plane even after the voltage is nearly doubled (image 6). The lateral extent of the domain is reduced slightly with the removal of the bias (image 7) and remains unchanged after the tip is removed (image 8). (B) Normal component of the electric field from the surface probe. (C) Normal component of the electric field, including top and bottom Schottky junctions. (D) A ferroelectric hysteresis loop formed by the primary 71° switching as determined by the area of a switched domain.[206]

Jia *et al.*[205] used aberration-corrected TEM to study the cation–oxygen dipoles near 180° domain walls in epitaxial $PbZr_{0.2}Ti_{0.8}O_3$ thin films on the atomic scale. Similarly, Polking *et al.*[213] studied ferroelectric ordering in GeTe and $BaTiO_3$ nanocrystals (sub 10 nm) by obtaining maps of atomic-scale ferroelectric structural distortions using aberration-corrected TEM, in conjunction with holographic polarisation imaging. Gregg *et al.*[79, 111, 206] have also explored the ferroelectric domain patterns in various ferroelectric nanostructures using scanning transmission electron microscope (STEM).[80,109,207] Of note, the ferroelectric domain patterns and their orientations in isolated $PbZr_{0.42}Ti_{0.58}O_3$ single-crystal nanodots were visualised by means of bright-and dark-field TEM imaging.[109]

Raman spectroscopy can yield important information regarding the local crystal symmetry of a material, due to its sensitivity to atomic displacements and lattice vibrations, and thus can be used to study the domain structure and phase transition/stability in a ferroelectric material.[139,140,214,215] Ultraviolet Raman spectroscopy has been used to measure to measure T_C in ultrathin films and superlattices.[216,217] Tenne *et al.*[216] examined the size-dependence of T_C in $BaTiO_3$ films as thin as 1.6 nm using UV Raman scattering. The combination of SPM and spectroscopy techniques enables the characterisation of the structure-properties relationship of ferroelectric nanomaterials with high spatial resolution.[45] For example, Berweger *et al.*[47] used tip-enhanced Raman spectroscopy (TERS), a combination of SPM and Raman spectroscopy, to determine the crystallographic orientation and to image the ferroelectric domains in $BaTiO_3$ nanocrystals, with ~ 3 nm spatial resolution. In a similar way, scanning nonlinear dielectric microscopy (SNDM) has been used for the observation of ferroelectric polarisation distributions, domains and measurement of dielectric characteristics at nanoscale.[42-44] Non-contact

mode scanning nonlinear dielectric microscopy (NC-SNDM) allows the visualisation of nanodomains and domain walls with atomic-scale resolution. In addition, SNDM has many advantages over PFM, such as high speed imaging of domains and the absence of screening effect from free surface charges.[42] All the techniques mentioned above provide an in-depth understanding of nanoscale ferroelectricity, which potentially unlocks numerous future applications for ferroelectric nanostructures.

1.6 Scaling Effects of Nanoscale Ferroelectric Materials

The scaling of a ferroelectric into 'nano' dimensions results in an increase in the materials surface area, at which point surfaces charges play a dominant role in determining the polarisation of the nanomaterial. 1n 1979, Kretschmer *et al.*[218] highlighted the influence of surface effects on the spontaneous polarisation of ferroelectric thin films. Thus transforming a bulk ferroelectric material into a nanostructured form can render significant changes to its characteristics, such as spontaneous polarisation (P_S), T_C and polarisation domain structure, which can be used to tune or tailor the ferroelectric features of a material.[21,31] Moreover, nanostructuring can generate highly dense arrays of isolated ferroelectric nanostructures and domains.[87,90,219] Isolated domains can acts as individual memory elements for storing 'bits' of data required for high-density ferroelectric memory storage, *e.g.* Lee *et al.*[87] fabricated arrays of individually addressable Pt/PZT/Pt nanodot capacitors with a density of 176 Gb inch^{-2}, for non-volatile ferroelectric random access memory (FeRAM).

A consequence of nanostructuring ferroelectric materials is the appearance of a critical size limit, below which spontaneous polarisation cannot be sustained in a

ferroelectric material.[30,32] One cause of lost ferroelectric behaviour in nanoscale systems is the existence of a depolarising field, due to the incomplete compensation of the polarisation induced surface charges over a large surface area.[33,220] Thus the basic understanding of this size limit in ferroelectrics is of prime importance to many potential applications,[36] since this limit determines the extent to which a ferroelectric material can be scaled down without losing its characteristics. Last decade witnessed considerable progress in investigating the critical size limit and the size influence of many ferroelectric nanostructures, of various dimensions and geometries. Even though several experimental reports on the minimum size limit of various nanoferroelectrics have been published, there have been discrepancies between the stated critical sizes, depending on the preparation route, morphology and characterisation tool used.[30,32,139,140,161,221-225] For example, in 1988 Ishikawa and co-workers experimentally demonstrated that sol-gel-prepared $PbTiO_3$ nanoparticles displayed a critical size limit of approximately 10 nm at 300 K.[139,140] Later on, Fong *et al.*[32] demonstrated that the ferroelectric phase in $PbTiO_3$ thin films was stable for thicknesses down to 3 unit cells (~ 1.2 nm) at room temperature. Roelofs *et al.*[99] suggested that the reduced critical size-limit of thin films could be due to the fact that they shrink the ferroelectric polarisation component in one dimension only, but not in all three directions as with nanoparticles. The critical film thickness of other pervoskite-based ferroelectrics such as $BaTiO_3$ (2.4 nm)[225] and PZT (4 nm)[222] have also been demonstrated experimentally. Apart from thin films,[32,161,221,222,225] many other nanostructured ferroelectrics have also been the subject of size-induced ferroelectric behaviour and these theoretical and experimental findings are discussed in the forthcoming section.

Zero dimensional (0D) ferroelectrics, *e.g.* nanoparticles, have been widely investigated by researchers.[30,139,140,223] For example, the finite size-effect on the ferroelectric phase transitions in $PbTiO_3$ nanoparticles were studied in the late '80s.[140], *e.g.* Ishikawa *et al.*[139, 140] noticed a decrease in T_C with a decrease in the size of $PbTiO_3$ nanoparticles.[139,140] Later in the mid '90s, Zhong[226] and Wang[227,228] *et al.* theoretically predicted a decrease in the polarisation and T_C with decreasing particle size for $PbTiO_3$ and $BaTiO_3$ nanoparticles. Park *et al.*[30] explored the particle-size induced phase transition in $BaTiO_3$ nanoparticles, revealing that the size reduction of $BaTiO_3$ progressively increased the symmetry of its crystal structure, as evidenced by a decrease in tetragonal distortion, and consequently suppression of its ferroelectric polarisation.[30] Sun[229] and Jiang *et al.*[223] observed similar trends for $BaTiO_3$ and $PbTiO_3$ nanoparticles respectively. Jiang *et al.*[223] also noticed an increase in the dielectric constant as a function of decreasing $PbTiO_3$ particle size, attributed to the presence of an amorphous surface layer and surface energy associated with domain walls.[223] Polking *et al.*[213] revealed experimentally the influence of surface depolarisation effects on ferroelectric polarisation stability at the nanoscale, by comparing highly conducting GeTe with strongly insulating $BaTiO_3$ nanocrystals of comparable sizes (sub 10 nm) and shapes. The polar GeTe crystals were observed to stabilise nanoscale ferroelectricity more effectively than insulating $BaTiO_3$ particles, through effective screening of polarisation-induced surface charges.[213] In addition, they demonstrated room-temperature ferroelectric polarisation switching in 10 nm $BaTiO_3$ nanocubes using PFM.[213] The concept of mechanically induced stress effects on nanoscale ferroelectrics has been reported for $BaTiO_3$ nanoparticles, by Basun *et al.*[230] Not only were $BaTiO_3$ nanoparticles observed to maintained their ferroelectric behaviour down to 10 nm, but they also

showed enhanced spontaneous polarisation and dipole moment values. Numerous reports have been published to-date on the size-driven ferroelectric properties of various nanoparticles.[33,63,141,207,224,231-234]

2D patterned arrays of ferroelectric nanoparticles, nanoislands and nanodots have been extensively studied for their scaling effect, due to their potential use in high-density FeRAM cells.[68,70,87,90,91,138,173,183,219] For example, Lee *et al.*[87] demonstrated ferroelectric switching in individual Pt/PZT/Pt nanodot capacitors with diameters of 60 nm and a height between 20–40 nm, where two neighbouring nanocapacitors could be switched into opposite states. The presence of single polarisation-domains in individual ferroelectric nanodots will be highly beneficial for the realisation of FeRAM with enhanced performance.[169] For example, Lu *et al.*[57] successfully fabricated epitaxial arrays of $BaTiO_3$ nanodots on $SrRuO_3/SrTiO_3(001)$ substrates with individual nanodots possessing single *c*-domain structures. Similar mono-domain formation was observed in arrays of $PbTiO_3$ nanodots.[101,172,235] Kim *et al.*[101] noted a relatively high piezoresponse in $PbTiO_3$ nanodots and attributed this enhancement to the presence of uniform sized *c*-domains. Son and co-workers explored the size-dependent ferroelectric behaviour in $PbTiO_3$ nanodots.[172,235] They noted a decrease in the piezoelectric coefficient (d_{33}) and an increase in the coercive electric field with decreasing thickness, or increasing lateral size, of the nanodots and illustrated that $PbTiO_3$ nanodots with diameter around 10 nm could preserve ferroelectricity.[172,235] Similar trend in ferroelectric behaviour was also reported by Kim *et al.*[101] Ma *et al.*[70] demonstrated the retention of ferroelectricity in arrays of $BaTiO_3$ nanocrowns and $SrBi_2Ta_2O_9$ nanorings with dimensions as small as ~9 and 5 nm, respectively. Chu *et al.*[95] studied the role of substrate-ferroelectric interfaces on the size-driven ferroelectricity in epitaxially grown PZT nanoislands on

$SrTiO_3$(001) substrates. They highlighted that individual PZT nanoislands, with a height of ~10 nm, displayed ferroelectric polarisation instability associated with misfit dislocations between the PZT lattice and the substrate.

Significant progress has been achieved in understanding the scaling effects in 1D ferroelectrics, especially nanowires. Yun[153] and Urban *et al.*[56] provided the seminal experimental evidence for the presence of ferroelectricity in individual $BaTiO_3$ nanowires as small as 10 nm in diameter, using scanning probe microscopy. Moreover, they demonstrated the non-volatile memory application potential of these nanowires by locally switching ferroelectric polarisation domains in these structures, as small as 100 nm^2.[153] Also, Suyal *et al.*[236] studied nanoscale ferroelectric behaviour in potassium niobate tantalate [$K(Nb_{0.8}Ta_{0.2})O_3$] nanorods using PFM and were successful at switching the polarisation direction of an area of 50 nm^2 on an individual nanorod. Many theoretical investigations were subsequently undertaken to elucidate ferroelectric behaviour in 1D nanoferroelectrics. For instance, Naumov and Fu theoretically predicted the existence of ferroelectric ordering in PZT nanowires with diameters larger than 2 nm.[237] They also concluded that the 1D morphology of nanowires may force the polarisation to align either along the longitudinal or the transverse direction, depending on the extent of the depolarisation field in that particular direction.[237] Thus the diameter of a ferroelectric nanowire may be used to tune the magnitude of spontaneous polarisation and T_C.[237] Also, Hong *et al.*[35] demonstrated theoretically that T_C, the mean polarisation and the area of ferroelectric hysteresis loops decreases upon reducing the diameter of $BaTiO_3$ nanowires (Figure 1.13) and the ferroelectricity in these wires disappears at a critical size of ~ 1.2 nm,[35] consistent with the prediction by Geneste *et al.*[34]

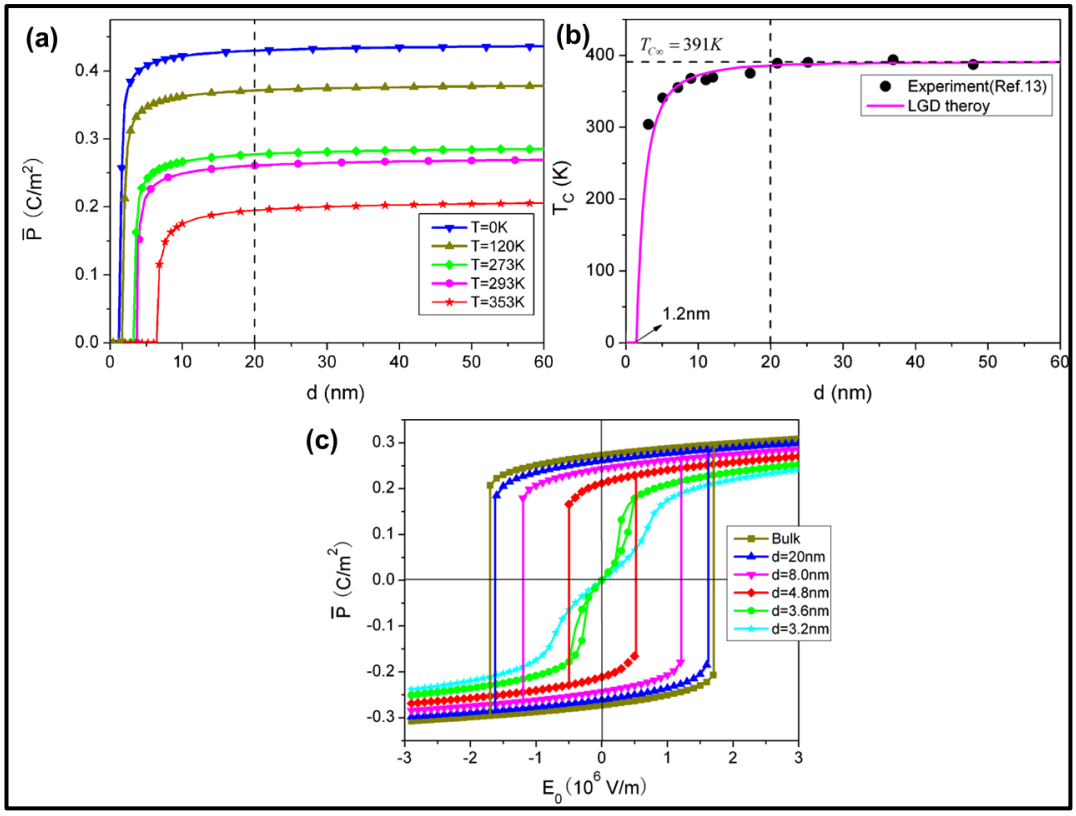

Figure 1.13. Size effects on (a) the mean polarisation at different temperatures, (b) T_C (black dots are from experiment[238]) and (c) polarisation-electric field (P-E) hysteresis loops ($T = 293$ K) of $BaTiO_3$ nanowires.[35]

Moreover, Spanier *et al.*[238] proved experimentally that T_C in $BaTiO_3$ nanowires was inversely proportional to the nanowire diameter. They noticed that T_C fell below room temperature at a nanowire diameter ~ 3 nm,[238] while bulk $BaTiO_3$ samples show a T_C of 120 °C.[8,239] An extrapolation of this data indicated that $BaTiO_3$ nanowires with diameter as small as 0.8 nm can support ferroelectricity at lower temperatures. They explained the observed ferroelectric stability at lower nanowire diameters by an adsorbate-induced charge screening mechanism, by which the depolarisation field can be minimised; for instance, by surface hydroxyl (-OH) groups. In addition, their theoretical calculations indicated that the ferroelectric polarisation can be tuned by changing the surface properties of the nanowire, which

opened up new possibilities in controlling ferroelectricity at the molecular level.[240,241] Li and co-workers studied the polarisation-dependence of physisorption on ferroelectric surfaces.[241] They investigated the energetics of physisorption on ferroelectric domains for CH_3OH and CO_2 on $BaTiO_3$ and $Pb(Ti_{0.52}Zr_{0.48})O_3$ thin film surfaces, with the aim of tailoring surface reactivity. Recently, Louis *et al.*[242] demonstrated experimentally that the direction and extent of ferroelectric polarisation in a ferroelectric nanowire can be tuned by varying its size. They conducted their study on $KNbO_3$ and $BaTiO_3$ nanowires using a combination of experimental and theoretical techniques, such as X-ray diffraction, Raman spectroscopy and first-principles-calculation, to reveal the nanoscale ferroelectric phase transition mechanism. Also, Schilling and co-workers demonstrated morphologically-controlled ferroelectric polarisation in single-crystal $BaTiO_3$ nanowires, by locally changing the aspect ratio of the nanowires using FIB milling techniques.[80] They noticed the presence of axial (∥ to the nanowire axis) and non-axial (⊥ to the axis) polarisation components in these nanowires, which were strongly sensitive to the local morphology.

Any fabrication technique that can easily manipulate the size and dimensions of ferroelectric nanowires offers great advantages for studying the scaling effect. From this viewpoint, template-based fabrication techniques need special mention. Preferential crystal orientation, ordering and high-density arrays of ferroelectric nanostructures can be achieved by templating.[71,89,100,103,105,117,167,196] Since ferroelectricity is a co-operative phenomenon, crystal orientation and ordering have a significant influence on the ferroelectric properties of nanoscale materials, such as polarisation direction and domain structure. Recently, Bernal *et al.*[89] fabricated highly-ordered vertical arrays of PZT nanotubes with variable diameters, using an

EBL-patterned polymeric electron resist template, to study piezoelectric size effects. The size effect in the PZT nanotubes with various wall thicknesses, ranging from 5 nm to 25 nm, was studied while keeping the aspect ratio constant. They noticed an increase in the remnant piezoresponse and a decrease in coercive voltage with increasing tube wall thickness and also the presence of a critical size limit at ~ 10 nm. Yadlovker *et al.*[167] prepared highly dense array of Rochelle salt (RS) single crystalline nanorods with uniform ferroelectric polarisation orientation and nanodomain sizes using AAO templates. These arrays of nanowires exhibited an enhancement in their spontaneous polarisation, one order higher than reported for bulk RS, due to the single crystalline nature and long-range ordering of the wires inside the AAO membranes. Similar enhancements have been reported for single crystalline KIO_3, [243] Sb_2S_3 [127] and $PbTiO_3$ [198,199] nanorods. As noted above, preferential orientation of ferroelectric nanostructures can enhance ferroelectricity by introducing anisotropy in a particular direction. Vertically aligned PVDF−TrFE co-polymer nanograss structures showed a piezoelectric response (210.4 pm V^{-1}) five times larger than that of its flat thin film counterparts.[132] Similar enhancements in piezoelectric performance were observed in horizontally aligned arrays of PZT nanowires, where the nanowires displayed the highest reported piezoelectric coefficient (d_{eff} ~145 pm V^{-1}) reported,[170] as well as in arrays of buckled PZT nanoribbons.[244] More in depth information on scaling effects in nanoscale ferroelectrics can found in recently published reviews.[14,16,19]

1.7 Applications of Nanoscale Ferroelectric Materials

The polarisation of ferroelectric materials can be changed by using three forms of energy, *i.e.* electric, thermal and mechanical or vice versa, giving these materials

pyroelectric and piezoelectric characteristics as well. These three inter-dependent properties of ferroelectrics have been widely exploited for many functional applications.[11,239,245,246] The various applications of ferroelectrics are schematically shown in Figure 1.14. The reversible polarisation of a ferroelectric material can be used in non-volatile memory applications, as the direction of polarisation switching represents the binary '1' and '0' in data storage.[11,239,246,247] Ferroelectric thin films have already shown potential as FeRAMs in memory storage applications.[11,239,246] The piezo effect in ferroelectrics can be used to convert mechanical energy to electrical energy, or vice versa, and find wide-spread use as actuators, transducers and micro-elelctromechanical (MEMS) devices.[11] As all ferroelectric materials are pyroelectric, they can also generate an electrical current in response to any change in ambient temperature; this principle finds use in infrared thermal imaging.[10,248] In addition, pyroelectric materials can act as energy scavengers,[249] whereby electrical energy can be created from wasted heat in an electronic circuit.[250] Owing to their high dielectric permittivity, ferroelectrics also find extensive use as capacitors in electronic industry.[11,239,245] Apart from the niche applications mentioned above, the latest developments in the use of nanoferroelectrics are summarised in the following section.

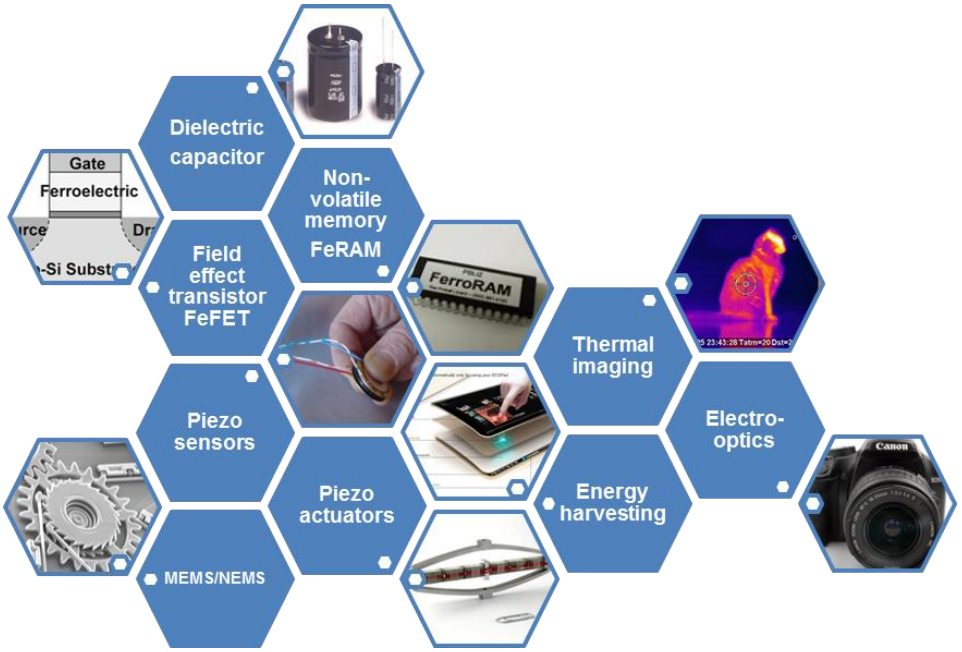

Figure 1.14. Application ranges of ferroelectric, piezoelectric and pyroelectric materials.

Significant efforts have been made recently to achieve high efficiency ferroelectric memory devices, through the assistance of nanostructuring.[13,18,20,87,90,133,196,251-255] Different types of nanodevice architectures with improved features have been realised, based on the reversible polarisation of the ferroelectrics, *e.g.* switchable remnant polarisation in a ferroelectric material is applied in FeRAM.[247] By scaling down the size of individual memory cells, the storage efficiency of FeRAMs can be greatly improved.[87] Shen *et al.*[157] explored the potential application of horizontally-aligned arrays of PZT nanowires for multi-bit storage applications. In addition, the ferroelectric polarisation can be coupled directly to the channel of a field effect transistor (FET), to form ferroelectric FET or FeFET, in which the direction of the polarisation determines the on-off state of the device.[13,255] Recently there has been significant interest in nanostructured ferroelectric polymers, especially PVDF-TrFE copolymers, for non-volatile memory cells owing to their cost effective production

and inherent flexibility.[131,133,253,254] For example, PVDF-TrFE based FeFETs with enhanced memory features were realised by nano confinement of the polymer within self-assembled organosilicate lamellae.[133] The reversible polarisation of ferroelectric materials could also be used to change the charge injection/transport properties of the material, and has the potential for memory storage.[12,18] A ferroelectric tunnel junction (FTJ) is working on this principle, where the electrical resistance at a FTJ can be tuned using orientation of ferroelectric polarization.[13,18,204,252,256-260] Chanthbouala *et al.*[252] have demonstrated FTJ-based solid state memory with high off/on ratios (100), and very low write power (~ 1×10^4 A cm^{-2}) using a 2 nm $BaTiO_3$ thin film (Figure 1.15). Apart from electronic applications, piezoelectric nanostructures, especially nanowires, have been studied extensively for their potential energy harvesting capabilities from collective mechanical movements.[261] Pyroelectric energy conversion also offers a way to convert waste heat directly into electricity and can be potentially used as an energy harvester.[249,250]

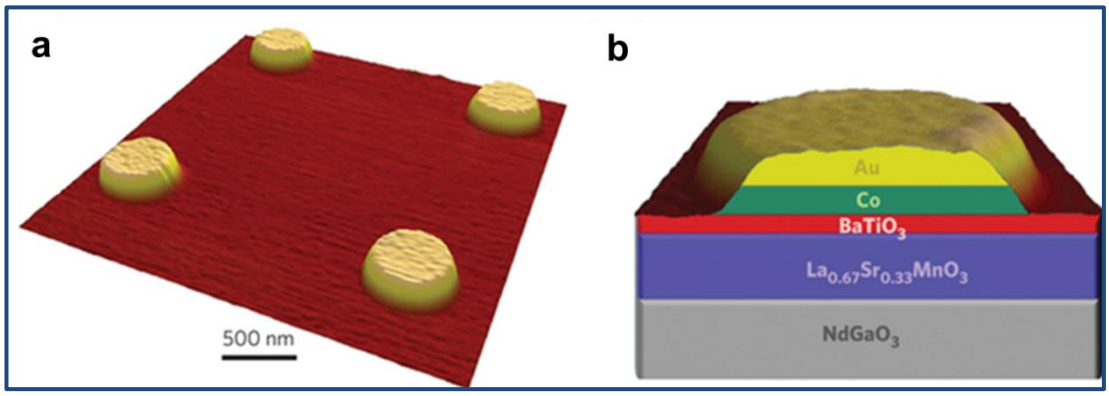

Figure 1.15. (a) AFM image of four typical FTJ nanodevices defined using electron-beam lithography. (b) Schematic of a gold (10 nm)/cobalt (10 nm)/$BaTiO_3$ (2 nm)/$La_{0.67}Sr_{0.33}MnO_3$ (30 nm) nanodevice on a (001) $NdGaO_3$ single-crystal substrate.[252]

Most of the applications mentioned above make use of either thin films or 1D ferroelectric nanostructures. Isolated ferroelectric nanoparticles also find use in a wide range of applications. For example, ferroelectric nanoparticles find extensive use as a filler material in polymer-nanocomposite based structures.[232,262] $BaTiO_3$ nanoparticle-based polymer nanocomposites are widely studied. Isolated super-paraelectric $BaTiO_3$ and $(Ba,Sr)TiO_3$ nanoparticles (8-12 nm) synthesised via a solvothermal process find use as a functional filler material in polymer composite based organic field effect transistors (OFETs).[232] Surface functionalisation is another active area of interest for ferroelectric nanoparticles.[263] Owing to the high surface energy of nanoparticles, their functionalisation using suitable organic moieties can add tunability to the dielectric and functional characteristics of ferroelectric nanocrystals.[240] In addition, the dispersion of ferroelectric nanoparticles in a polymer matrix can be improved by proper modification of the surface of ferroelectric nanoparticles, which in turn provides enhanced dielectric characteristics to the polymer nanocomposite.[262,264-266] Ferroelectric nanoparticle-filled polymer nanocomposites have also shown potential in applications such as dielectric energy storage, flexible thin-film dielectric capacitors[262,264-266] and flexible electrical energy generators[267].

1.8 Future Outlook of Nanoscale Ferroelectric Materials

The prospect for nanoscale ferroelectric materials is promising, as evident from the growing research articles in theory, fabrication and application aspects of these structures.[13,15-20,49,51,87,133] A basic understanding of the finite-size effect in nanoscale ferroelectric is a prerequisite for the development of new devices and hence more theoretical studies in this area would be highly advantageous.

Fabrication routes that have the capability of generating nanostructured patterns with predictable shapes and controlled dimensions, at desired locations on a substrate of interest, are critical for the integration of novel nanoferroelectric devices. For instance, the potential use of nanoimprint lithography[92,137,138,157] and self-assembled BCPs[189,191,268] to produce highly ordered patterns of nanostructures could be effectively exploited to achieve the above mentioned challenges. Efforts in enhancing the spatial resolution of current characterisation tools will also be required to tackle the future developments in nanoscale ferroelectric research.[41,45,212] Characterisation techniques such as PFM, SNDM,[42-44] TERS[45,47] and TEM[109,205,206,213] require special mention in this regard. The broad application spectrum of nanoscale ferroelectric materials spanning from memory devices to self-powered nanogenerators may fuel future interests in research and developments in this area. Progress in controlling ferroelectricity on the nanoscale offers great potential for nanoscale ferroelectric devices, especially FeFETs and FTJs.[16, 185, 245, 246, 251-255] The 2011 international technology road map for semiconductors (ITRS) has listed ferroelectric-based FTJs and FeFETs as two emerging memory technologies.[12] Moreover, the still advancing area of piezotronics offers immense possibilities in the creation of efficient self-powered microelectronic devices.[85,108,193,194,244,261,269]

1.9 Thesis Summary

Chapter 2 of this thesis provides an overview of the experimental methods and characterisation tools utilised to obtain the research data reported in the thesis. In particular, this chapter details the general principles of piezoresponse microscopy (PFM).

Chapter 3 highlights the fabrication of arrays of Sb_2S_3 nanowires, with variable diameters, using a solvent-less method employing AAO templates. A detailed account of the PFM characterisation, such as domain imaging and switching of polarisation, of the arrays of Sb_2S_3 nanowires is provided.

Chapter 4 details the preparation of vertically aligned SbSI nanorods and wire arrays using a surface-roughness assisted vapour-phase deposition method. The qualitative and quantitative nanoscale ferroelectric properties of these nanostructures are also discussed.

Chapter 5 highlights the fabrication of highly ordered arrays of PZT nanodots, using BCP self-assembled templates, and their ferroelectric characterisation using PFM.

Chapter 6 summarises the conclusions derived from the experimental results obtained in chapters 3, 4 and 5. The chapter also outlines the future prospect in fabrication and application aspects of ferroelectric nanostructures.

1.10 References

(1) Curie, J.; Curie, P. *Comptes Rendus de l'Académie des Sciences* **1880**, *91*, 294

(2) Curie, J.; Curie, P. *C R Acad Sci Gen.* **1880**, *91*, 383

(3) Valasek, J. *Ferroelectrics* **1971**, *2*, 239.

(4) Schrödinger, E. *S.B. Akad. Wiss. Wien* **1912**, *121*, 1937.

(5) Valasek, J. *Physical Review* **1921**, *17*, 475.

(6) Fousek, J. *Proceedings of the Ninth IEEE International Symposium on Applications of Ferroelectrics, ISAF '94.* **1994**, 1.

(7) Cross, L. E.; Newnham, R. E. History of Ferroelectrics. In *High technology ceramics: past, present, and future : the nature of innovation and change in ceramic technology*; Kingery, W. D., Lense, E., Eds.; American Ceramic Society: Westerville, OH, 1986; Vol. III; pp 289.

(8) Vonhippel, A.; Breckenridge, R. G.; Chesley, F. G.; Tisza, L. *Ind. Eng. Chem.* **1946**, *38*, 1097.

(9) Mitsui, T. Ferroelectrics and Antiferroelectrics. In *Springer Handbook of Condensed Matter and Materials Data*; Martienssen, W., Warlimont, H., Eds.; Springer Berlin Heidelberg, 2005; pp 903.

(10) Lines, M. E.; Glass, A. M. In *Principles and Applications of Ferroelectrics and Related Materials*; Oxford University Press: Oxford, 1977.

(11) Haertling, G. H. *J. Am. Ceram. Soc.* **1999**, *82*, 797.

(12) *The International Technology Roadmap for Semiconductors: 2011 Edition, Emerging research materials and Emerging research devices;* http://www.itrs.net/Links/2011ITRS/2011Chapters/2011ERM.pdf, http://www.itrs.net/Links/2011ITRS/2011Chapters/2011ERD.pdf.

(13) Bibes, M. *Nat Mater* **2012**, *11*, 354.

(14) Gregg, J. M. *physica status solidi (a)* **2009**, *206*, 577.

(15) Gruverman, A.; Kholkin, A. *Rep. Prog. Phys.* **2006**, *69*, 2443.

(16) Han, H.; Kim, Y.; Alexe, M.; Hesse, D.; Lee, W. *Adv. Mater.* **2011**, *23*, 4599.

(17) Handoko, A. D.; Goh, G. K. L. *Science of Advanced Materials* **2010**, *2*, 16.

(18) Ionescu, A. M. *Nat Nano* **2012**, *7*, 83.

(19) Rørvik, P. M.; Grande, T.; Einarsrud, M.-A. *Adv. Mater.* **2011**, *23*, 4007.

(20) Scott, J. F.; Morrison, F. D.; Miyake, M.; Zubko, P. *Ferroelectrics* **2006**, *336*, 237.

(21) Spaldin, N. A. *Science* **2004**, *304*, 1606.

(22) Kao, K. C. Chapter 4 - Ferroelectrics, Piezoelectrics, and Pyroelectrics. In *Dielectric Phenomena in Solids*; Academic Press: San Diego, 2004; pp 213.

(23) Electrical Properties-Ferroelectrics and Related Substances. In *Landolt-Börnstein - Group III Condensed Matter*; Shiozaki, Y., Nakamura, E., Mitsui, T., Eds.; Springer-Verlag, 2002; Vol. III/36a-c.

(24) Weil, R.; Nkum, R.; Muranevich, E.; Benguigui, L. *Phys. Rev. Lett.* **1989**, *62*, 2744.

(25) Polking, M. J.; Zheng, H.; Ramesh, R.; Alivisatos, A. P. *J. Am. Chem. Soc.* **2011**, *133*, 2044.

(26) Fatuzzo, E.; Nitsche, R.; Harbeke, G.; Ruppel, W.; Roetschi, H.; Merz, W. J. *Physical Review* **1962**, *127*, 2036.

(27) Lovinger, A. J. *Science* **1983**, *220*, 1115.

(28) Kinam, K.; Gitae, J.; Hongsik, J.; Sungyung, L. *Proceedings of the IEEE 2005 Custom Integrated Circuits Conference.* **2005**, 423.

(29) Fischer, D. As flexible as it gets: FRAM MCU. In *connectingindustry.com/electronics*, 2010; Vol. September 2010; pp 22.

(30) Yung, P.; Won-Jae, L.; Ho-Gi, K. *J. Phys.: Condens. Matter* **1997**, *9*, 9445.

(31) Ahn, C. H.; Rabe, K. M.; Triscone, J.-M. *Science* **2004**, *303*, 488.

(32) Fong, D. D.; Stephenson, G. B.; Streiffer, S. K.; Eastman, J. A.; Auciello, O.; Fuoss, P. H.; Thompson, C. *Science* **2004**, *304*, 1650.

(33) Naumov, I. I.; Bellaiche, L.; Fu, H. *Nature* **2004**, *432*, 737.

(34) Geneste, G.; Bousquet, E.; Junquera, J.; Ghosez, P. *Appl. Phys. Lett.* **2006**, *88*, 112906.

(35) Hong, J.; Fang, D. *Appl. Phys. Lett.* **2008**, *92*, 012906.

(36) Vilquin, B.; Gautier, B.; Brugere, A.; Moulet, J. S. *AIP Conference Proceedings* **2009**, *1173*, 129.

(37) Cao, G. *Nanostructures and Nanomaterials : Synthesis, Properties, and Applications*, 1 ed.; Imperial College Press: London, 2004; Vol. 1.

(38) Elisabeth, S. *J. Phys. D: Appl. Phys.* **2011**, *44*, 464003.

(39) Balke, N.; Bdikin, I.; Kalinin, S. V.; Kholkin, A. L. *J. Am. Ceram. Soc.* **2009**, *92*, 1629.

(40) Jesse, S.; Lee, H. N.; Kalinin, S. V. *Rev. Sci. Instrum.* **2006**, *77*, 073702.

(41) Maksymovych, P.; Huijben, M.; Pan, M.; Jesse, S.; Balke, N.; Chu, Y.-H.; Chang, H. J.; Borisevich, A. Y.; Baddorf, A. P.; Rijnders, G.; Blank, D. H. A.; Ramesh, R.; Kalinin, S. V. *Phys Rev B* **2012**, *85*, 014119.

(42) Tanaka, K.; Kurihashi, Y.; Uda, T.; Daimon, Y.; Odagawa, N.; Hirose, R.; Hiranaga, Y.; Cho, Y. *Jpn J Appl Phys* **2008**, *47*, 3311.

(43) Cho, Y. *J. Mater. Res.* **2011**, *26*, 2007.

(44) Cho, Y.; Kazuta, S.; Matsuura, K. *Appl. Phys. Lett.* **1999**, *75*, 2833.

(45) Lucas, M.; Riedo, E. *Rev. Sci. Instrum.* **2012**, *83*, 061101.

(46) Verma, P.; Ichimura, T.; Yano, T.; Saito, Y.; Kawata, S. *Laser & Photonics Reviews* **2010**, *4*, 548.

(47) Berweger, S.; Neacsu, C. C.; Mao, Y.; Zhou, H.; Wong, S. S.; Raschke, M. B. *Nat Nano* **2009**, *4*, 496.

(48) Pokropivny, V. V.; Skorokhod, V. V. *Materials Science and Engineering: C* **2007**, *27*, 990.

(49) Vrejoiu, I.; Alexe, M.; Hesse, D.; Gösele, U. *Adv. Funct. Mater.* **2008**, *18*, 3892.

(50) Vrejoiu, I.; Alexe, M.; Hesse, D.; Gosele, U. *Journal of Vacuum Science & Technology B* **2009**, *27*, 498.

(51) Zhu, X. *Recent Patents on Nanotechnology* **2009**, *3*, 42.

(52) Chen, Y.-Y.; Yu, B.-Y.; Wang, J.-H.; Cochran, R. E.; Shyue, J.-J. *Inorg. Chem.* **2008**, *48*, 681.

(53) Li, H.; Wu, H.; Lin, D.; Pan, W. *J. Am. Ceram. Soc.* **2009**, *92*, 2162.

(54) Ould-Ely, T.; Luger, M.; Kaplan-Reinig, L.; Niesz, K.; Doherty, M.; Morse, D. E. *Nat. Protocols* **2011**, *6*, 97.

(55) Urban, J. J.; Yun, W. S.; Gu, Q.; Park, H. *J. Am. Chem. Soc.* **2002**, *124*, 1186.

(56) Urban, J. J.; Spanier, J. E.; Ouyang, L.; Yun, W. S.; Park, H. *Adv. Mater.* **2003**, *15*, 423.

(57) Lu, X.; Kim, Y.; Goetze, S.; Li, X.; Dong, S.; Werner, P.; Alexe, M.; Hesse, D. *Nano Lett.* **2011**, *11*, 3202.

(58) Sun, W.; Pang, Y.; Li, J.; Ao, W. *Chem. Mater.* **2007**, *19*, 1772.

(59) Joshi, U. A.; Lee, J. S. *Small* **2005**, *1*, 1172.

(60) Zhu, Y.-F.; Zhang, L.; Natsuki, T.; Fu, Y.-Q.; Ni, Q.-Q. *ACS Applied Materials & Interfaces* **2012**, *4*, 2101.

(61) Zhan, H.; Yang, X.; Wang, C.; Chen, J.; Wen, Y.; Liang, C.; Greer, H. F.; Wu, M.; Zhou, W. *Cryst Growth Des* **2012**, *12*, 1247.

(62) Adireddy, S.; Lin, C.; Cao, B.; Zhou, W.; Caruntu, G. *Chem. Mater.* **2010**, *22*, 1946.

(63) Xia, F.; Liu, J.; Gu, D.; Zhao, P.; Zhang, J.; Che, R. *Nanoscale* **2011**, *3*, 3860.

(64) Yang, J.; Geng, B.; Ye, Y.; Yu, X. *CrystEngComm* **2012**, *14*, 2959.

(65) Hakuta, Y.; Ura, H.; Hayashi, H.; Arai, K. *Industrial & Engineering Chemistry Research* **2005**, *44*, 840.

(66) Edward, D. H.; Nicholas, A. P.; Bryan, D. H.; Nitin, P. P. *Nanotechnology* **2010**, *21*, 335601.

(67) Teresa Buscaglia, M.; Harnagea, C.; Dapiaggi, M.; Buscaglia, V.; Pignolet, A.; Nanni, P. *Chem. Mater.* **2009**, *21*, 5058.

(68) Ma, W.; Harnagea, C.; Hesse, D.; Gosele, U. *Appl. Phys. Lett.* **2003**, *83*, 3770.

(69) Ma, W.; Hesse, D.; Gösele, U. *Small* **2005**, *1*, 837.

(70) Wenhui, M.; Dietrich, H.; Ulrich, G. *Nanotechnology* **2006**, *17*, 2536.

(71) Luo, Y.; Szafraniak, I.; Nagarajan, V.; Wehrspohn, R. B.; Steinhart, M.; Wendorff, J. H.; Zakharov, N. D.; Ramesh, R.; Alexe, M. *Integrated Ferroelectrics* **2003**, *59*, 1513.

(72) Kristina, Ž.; Francisco, H.-R.; Joan Daniel, P.; Joan Ramon, M.; Aleksander, R.; Miran, Č. *Nanotechnology* **2011**, *22*, 385501.

(73) Maxim, F.; Ferreira, P.; Vilarinho, P. M.; Aimable, A.; Bowen, P. *Cryst Growth Des* **2010**, *10*, 3996.

(74) Deng, H.; Qiu, Y.; Yang, S. *J. Mater. Chem.* **2009**, *19*, 976.

(75) Mao, Y.; Banerjee, S.; Wong, S. S. *J. Am. Chem. Soc.* **2003**, *125*, 15718.

(76) Cai, Z.; Xing, X.; Yu, R.; Sun, X.; Liu, G. *Inorg. Chem.* **2007**, *46*, 7423.

(77) Rørvik, P. M.; Lyngdal, T.; Sæterli, R.; van Helvoort, A. T. J.; Holmestad, R.; Grande, T.; Einarsrud, M.-A. *Inorg. Chem.* **2008**, *47*, 3173.

(78) McQuaid, R. G. P.; McGilly, L. J.; Sharma, P.; Gruverman, A.; Gregg, J. M. *Nat Commun* **2011**, *2*, 404.

(79) McQuaid, R. G. P.; McMillen, M.; Chang, L. W.; Gruverman, A.; Gregg, J. M. *J. Phys.: Condens. Matter* **2012**, *24*, 024204.

(80) Schilling, A.; Bowman, R. M.; Catalan, G.; Scott, J. F.; Gregg, J. M. *Nano Lett.* **2007**, *7*, 3787.

(81) Qi, J. Q.; Wang, Y.; Ping Chen, W.; Tu Li, L.; Lai Wah Chan, H. *J. Solid State Chem.* **2005**, *178*, 279.

(82) Niederberger, M.; Garnweitner, G.; Pinna, N.; Antonietti, M. *J. Am. Chem. Soc.* **2004**, *126*, 9120.

(83) Chen, Y.; Chen, W.; Guo, F.; Li, M.-Y.; Liu, W.; Zhao, X.-Z. *Chinese Physics B* **2009**, *18*, 3922.

(84) Nelson, J. A.; Wagner, M. J. *J. Am. Chem. Soc.* **2002**, *125*, 332.

(85) Xu, S.; Hansen, B. J.; Wang, Z. L. *Nat Commun* **2010**, *1*, 93.

(86) Xu, G.; Jiang, W.; Qian, M.; Chen, X.; Li, Z.; Han, G. *Cryst Growth Des* **2008**, *9*, 13.

(87) Lee, W.; Han, H.; Lotnyk, A.; Schubert, M. A.; Senz, S.; Alexe, M.; Hesse, D.; Baik, S.; Gosele, U. *Nat Nano* **2008**, *3*, 402.

(88) Clemens, S.; et al. *Nanotechnology* **2009**, *20*, 075305.

(89) Bernal, A.; Tselev, A.; Kalinin, S.; Bassiri-Gharb, N. *Adv. Mater.* **2012**, *24*, 1160.

(90) Alexe, M.; Harnagea, C.; Hesse, D.; Gosele, U. *Appl. Phys. Lett.* **1999**, *75*, 1793.

(91) Huang, C.-K.; Chen, Y.-H.; Liang, Y.-C.; Wu, T.-B.; Chen, H.-L.; Chao, W.-C. *Electrochem. Solid-State Lett.* **2006**, *9*, C51.

(92) Shen, Z. K.; Chen, Z. H.; Li, H.; Qu, X. P.; Chen, Y.; Liu, R. *Appl. Surf. Sci.* **2011**, *257*, 8820.

(93) Li, Z.-D.; Shen, Z.-K.; Hui, W.-Y.; Qiu, Z.-J.; Qu, X.-P.; Chen, Y.-F.; Liu, R. *Microelectron. Eng.* **2011**, *88*, 2037.

(94) Szafraniak, I.; Harnagea, C.; Scholz, R.; Bhattacharyya, S.; Hesse, D.; Alexe, M. *Appl. Phys. Lett.* **2003**, *83*, 2211.

(95) Chu, M.-W.; Szafraniak, I.; Scholz, R.; Harnagea, C.; Hesse, D.; Alexe, M.; Gosele, U. *Nat Mater* **2004**, *3*, 87.

(96) Dawber, M.; Szafraniak, I.; Alexe, M.; Scott, J. F. *J. Phys.: Condens. Matter* **2003**, *15*, L667.

(97) Szafraniak, I.; Chu, M. W.; Harnagea, C.; Scholz, R.; Hesse, D.; Alexe, M. *Integrated Ferroelectrics* **2004**, *61*, 231.

(98) Torres, M.; Ricote, J.; Pardo, L.; Calzada, M. L. *Integrated Ferroelectrics* **2008**, *99*, 95.

(99) Roelofs, A.; Schneller, T.; Szot, K.; Waser, R. *Appl. Phys. Lett.* **2002**, *81*, 5231.

(100) Zhang, X. Y.; Zhao, X.; Lai, C. W.; Wang, J.; Tang, X. G.; Dai, J. Y. *Appl. Phys. Lett.* **2004**, *85*, 4190.

(101) Kim, Y.; Han, H.; Kim, Y.; Lee, W.; Alexe, M.; Baik, S.; Kim, J. K. *Nano Lett.* **2010**, *10*, 2141.

(102) Scott, J. F.; Fan, H. J.; Kawasaki, S.; Banys, J.; Ivanov, M.; Krotkus, A.; Macutkevic, J.; Blinc, R.; Laguta, V. V.; Cevc, P.; Liu, J. S.; Kholkin, A. L. *Nano Lett.* **2008**, *8*, 4404.

(103) Kim, J.; Yang, S. A.; Choi, Y. C.; Han, J. K.; Jeong, K. O.; Yun, Y. J.; Kim, D. J.; Yang, S. M.; Yoon, D.; Cheong, H.; Chang, K. S.; Noh, T. W.; Bu, S. D. *Nano Lett.* **2008**, *8*, 1813.

(104) Pantel, D.; Goetze, S.; Hesse, D.; Alexe, M. *ACS Nano* **2011**, *5*, 6032.

(105) Hernandez-Sanchez, B. A.; Chang, K.-S.; Scancella, M. T.; Burris, J. L.; Kohli, S.; Fisher, E. R.; Dorhout, P. K. *Chem. Mater.* **2005**, *17*, 5909.

(106) Chen, X.; Xu, S.; Yao, N.; Shi, Y. *Nano Lett.* **2010**, *10*, 2133.

(107) Shiyou, X.; Yong, S.; Sang-Gook, K. *Nanotechnology* **2006**, *17*, 4497.

(108) Wu, W.; Bai, S.; Yuan, M.; Qin, Y.; Wang, Z. L.; Jing, T. *ACS Nano* **2012**.

(109) McGilly, L. J.; Gregg, J. M. *Nano Lett.* **2011**, *11*, 4490.

(110) Nagarajan, V.; Stanishevsky, A.; Ramesh, R. *Nanotechnology* **2006**, *17*, 338.

(111) Zhu, R.; Zhu, K.; Qiu, J.; Bai, L.; Ji, H. *Mater. Res. Bull.* **2010**, *45*, 969.

(112) Hou, L.; Hou, Y.-D.; Song, X.-M.; Zhu, M.-K.; Wang, H.; Yan, H. *Mater. Res. Bull.* **2006**, *41*, 1330.

(113) JingBing, L.; Hao, W.; YuDong, H.; ManKang, Z.; Hui, Y.; Masahiro, Y. *Nanotechnology* **2004**, *15*, 777.

(114) Anokhin, A.; Lyanguzov, N.; Roshal', S.; Yuzyuk, Y.; Wang, W. *Physics of the Solid State* **2011**, *53*, 1867.

(115) Buscaglia, M. T.; Sennour, M.; Buscaglia, V.; Bottino, C.; Kalyani, V.; Nanni, P. *Cryst Growth Des* **2011**, *11*, 1394.

(116) Gu, H.; Hu, Z.; Hu, Y.; Yuan, Y.; You, J.; Zou, W. *Colloids and Surfaces A: Physicochemical and Engineering Aspects* **2008**, *315*, 294.

(117) Zhou, D.; Gu, H.; Hu, Y.; Qian, Z.; Hu, Z.; Yang, K.; Zou, Y.; Wang, Z.; Wang, Y.; Guan, J.; Chen, W. *J. Appl. Phys.* **2010**, *107*, 094105.

(118) Minghua, T.; Wei, S.; Feng, Y.; Jun, Z.; Guangjun, D.; Jianwei, H. *Nanotechnology* **2009**, *20*, 385602.

(119) Shaislamov, U.; Yang, J.-M.; Yang, B. *Physica E: Low-dimensional Systems and Nanostructures* **2012**, *44*, 1649.

(120) Das, R.; Khan, G. G.; Mandal, K. *J. Appl. Phys.* **2012**, *111*, 104115.

(121) Zhang, X. Y.; Dai, J. Y.; Lai, C. W. *Prog. Solid State Chem.* **2005**, *33*, 147.

(122) Dutta, D. P.; Jayakumar, O. D.; Tyagi, A. K.; Girija, K. G.; Pillai, C. G. S.; Sharma, G. *Nanoscale* **2010**, *2*, 1149.

(123) Wang, L.; Teleki, A.; Pratsinis, S. E.; Gouma, P. I. *Chem. Mater.* **2008**, *20*, 4794.

(124) Zhou, H.; Park, T.-J.; Wong, S. S. *J. Mater. Res.* **2006**, *21*, 2941.

(125) Nowak, M.; Szperlich, P.; Bober, Ł.; Szala, J.; Moskal, G.; Stróż, D. *Ultrason. Sonochem.* **2008**, *15*, 709.

(126) Nowak, M.; Kauch, B.; Szperlich, P.; Stróz, D.; Szala, J.; Rzychon, T.; Bober, L.; Toron, B.; Nowrot, A. *Ultrason. Sonochem.* **2010**, *17*, 487.

(127) Varghese, J.; Barth, S.; Keeney, L.; Whatmore, R. W.; Holmes, J. D. *Nano Lett.* **2012**, *12*, 868.

(128) Polking, M. J.; Urban, J. J.; Milliron, D. J.; Zheng, H.; Chan, E.; Caldwell, M. A.; Raoux, S.; Kisielowski, C. F.; Ager, J. W.; Ramesh, R.; Alivisatos, A. P. *Nano Lett.* **2011**, *11*, 1147.

(129) Son, J. Y.; Shin, Y.-S.; Song, S.-W.; Shin, Y.-H.; Jang, H. M. *The Journal of Physical Chemistry C* **2011**, *115*, 14077.

(130) Hu, Z.; Tian, M.; Nysten, B.; Jonas, A. M. *Nat Mater* **2009**, *8*, 62.

(131) Liu, Y.; Weiss, D. N.; Li, J. *ACS Nano* **2009**, *4*, 83.

(132) Hong, C.-C.; Huang, S.-Y.; Shieh, J.; Chen, S.-H. *Macromolecules* **2012**, *45*, 1580.

(133) Kang, S. J.; Bae, I.; Shin, Y. J.; Park, Y. J.; Huh, J.; Park, S.-M.; Kim, H.-C.; Park, C. *Nano Lett.* **2010**, *11*, 138.

(134) Martín, J.; Mijangos, C.; Sanz, A.; Ezquerra, T. A.; Nogales, A. *Macromolecules* **2009**, *42*, 5395.

(135) Lutkenhaus, J. L.; McEnnis, K.; Serghei, A.; Russell, T. P. *Macromolecules* **2010**, *43*, 3844.

(136) Hernandez, B. A.; Chang, K.-S.; Fisher, E. R.; Dorhout, P. K. *Chem. Mater.* **2002**, *14*, 480.

(137) Guo, L. J. *Adv. Mater.* **2007**, *19*, 495.

(138) Fang, J.-R.; Shen, Z.-K.; Yang, S.; Lu, Q.; Li, J.; Chen, Y.-F.; Liu, R. *Microelectron. Eng.* **2011**, *88*, 2033.

(139) Ishikawa, K.; Nomura, T.; Okada, N.; Takada, K. *Jpn J Appl Phys 1* **1996**, *35*, 5196.

(140) Ishikawa, K.; Yoshikawa, K.; Okada, N. *Phys Rev B* **1988**, *37*, 5852.

(141) Mohanty, D.; Chaubey, G. S.; Yourdkhani, A.; Adireddy, S.; Caruntu, G.; Wiley, J. B. *RSC Advances* **2012**, *2*, 1913.

(142) Meldrum, F. C.; Cölfen, H. *Chem. Rev.* **2008**, *108*, 4332.

(143) Li, Y.; Qian, F.; Xiang, J.; Lieber, C. M. *Mater. Today* **2006**, *9*, 18.

(144) Barth, S.; Hernandez-Ramirez, F.; Holmes, J. D.; Romano-Rodriguez, A. *Prog. Mater Sci.* **2010**, *55*, 563.

(145) Colinge, J.-P.; Lee, C.-W.; Afzalian, A.; Akhavan, N. D.; Yan, R.; Ferain, I.; Razavi, P.; O'Neill, B.; Blake, A.; White, M.; Kelleher, A.-M.; McCarthy, B.; Murphy, R. *Nat Nano* **2010**, *5*, 225.

(146) Hakim, M. M. A.; Lombardini, M.; Sun, K.; Giustiniano, F.; Roach, P. L.; Davies, D. E.; Howarth, P. H.; de Planque, M. R. R.; Morgan, H.; Ashburn, P. *Nano Lett.* **2012**, *12*, 1868.

(147) Liu, X.; Long, Y.-Z.; Liao, L.; Duan, X.; Fan, Z. *ACS Nano* **2012**, *6*, 1888.

(148) Xia, Y.; Yang, P.; Sun, Y.; Wu, Y.; Mayers, B.; Gates, B.; Yin, Y.; Kim, F.; Yan, H. *Adv. Mater.* **2003**, *15*, 353.

(149) Hu, J. T.; Odom, T. W.; Lieber, C. M. *Acc. Chem. Res.* **1999**, *32*, 435.

(150) Weber, B.; Mahapatra, S.; Ryu, H.; Lee, S.; Fuhrer, A.; Reusch, T. C. G.; Thompson, D. L.; Lee, W. C. T.; Klimeck, G.; Hollenberg, L. C. L.; Simmons, M. Y. *Science* **2012**, *335*, 64.

(151) Limmer, S. J.; Seraji, S.; Forbess, M. J.; Wu, Y.; Chou, T. P.; Nguyen, C.; Cao, G. Z. *Adv. Mater.* **2001**, *13*, 1269.

(152) Cho, S. B.; Oledzka, M.; Riman, R. E. *J. Cryst. Growth* **2001**, *226*, 313.

(153) Yun, W. S.; Urban, J. J.; Gu, Q.; Park, H. *Nano Lett.* **2002**, *2*, 447.

(154) Magrez, A.; Vasco, E.; Seo, J. W.; Dieker, C.; Setter, N.; Forró, L. *The Journal of Physical Chemistry B* **2005**, *110*, 58.

(155) Jung, J. H.; Lee, M.; Hong, J.-I.; Ding, Y.; Chen, C.-Y.; Chou, L.-J.; Wang, Z. L. *ACS Nano* **2011**, *5*, 10041.

(156) Shen, Z.; Qu, X.; Chen, Y.; Liu, R. *ACS Nano* **2011**, *5*, 6855.

(157) Shen, Z.; Chen, Z.; Lu, Q.; Qiu, Z.; Jiang, A.; Qu, X.; Chen, Y.; Liu, R. *Nanoscale Research Letters* **2011**, *6*, 474.

(158) Rabenau, A. *Angewandte Chemie International Edition in English* **1985**, *24*, 1026.

(159) Szperlich, P.; Nowak, M.; Bober, L.; Szala, J.; Stroz, D. *Ultrason. Sonochem.* **2009**, *16*, 398.

(160) Stanishevsky, A.; Aggarwal, S.; Prakash, A. S.; Melngailis, J.; Ramesh, R. *Journal of Vacuum Science & Technology B: Microelectronics and Nanometer Structures* **1998**, *16*, 3899.

(161) Ganpule, C. S.; Stanishevsky, A.; Su, Q.; Aggarwal, S.; Melngailis, J.; Williams, E.; Ramesh, R. *Appl. Phys. Lett.* **1999**, *75*, 409.

(162) Marshall, J. M.; Dunn, S.; Whatmore, R. W. *Integrated Ferroelectrics* **2004**, *61*, 223.

(163) Martin, C. R. *Science* **1994**, *266*, 1961.

(164) Routkevitch, D.; Tager, A. A.; Haruyama, J.; Almawlawi, D.; Moskovits, M.; Xu, J. M. *Ieee Transactions on Electron Devices* **1996**, *43*, 1646.

(165) Bae, C.; Yoo, H.; Kim, S.; Lee, K.; Kim, J.; Sung, M. A.; Shin, H. *Chem. Mater.* **2008**, *20*, 756.

(166) Schwirn, K.; Lee, W.; Hillebrand, R.; Steinhart, M.; Nielsch, K.; Gösele, U. *ACS Nano* **2008**, *2*, 302.

(167) Yadlovker, D.; Berger, S. *Phys Rev B* **2005**, *71*, 184112.

(168) Alexe, M.; Hesse, D.; Schmidt, V.; Senz, S.; Fan, H. J.; Zacharias, M.; Gosele, U. *Appl. Phys. Lett.* **2006**, *89*, 172907.

(169) Lee, J.-S.; Lee, B.-I.; Joo, S.-K. *Integrated Ferroelectrics* **2000**, *31*, 149.

(170) Nguyen, T. D.; Nagarah, J. M.; Qi, Y.; Nonnenmann, S. S.; Morozov, A. V.; Li, S.; Arnold, C. B.; McAlpine, M. C. *Nano Lett.* **2010**, *10*, 4595.

(171) Piner, R. D.; Zhu, J.; Xu, F.; Hong, S.; Mirkin, C. A. *Science* **1999**, *283*, 661.

(172) Son, J. Y.; Shin, Y.-H.; Ryu, S.; Kim, H.; Jang, H. M. *J. Am. Chem. Soc.* **2009**, *131*, 14676.

(173) Harnagea, C.; Alexe, M.; Schilling, J.; Choi, J.; Wehrspohn, R. B.; Hesse, D.; Gosele, U. *Appl. Phys. Lett.* **2003**, *83*, 1827.

(174) Alexe, M.; Hesse, D. *J Mater Sci* **2006**, *41*, 1.

(175) Hulteen, J. C.; Van Duyne, R. P. *Journal of Vacuum Science & Technology A: Vacuum, Surfaces, and Films* **1995**, *13*, 1553.

(176) Ma, W.; Hesse, D. *Appl. Phys. Lett.* **2004**, *85*, 3214.

(177) Waegner, M.; Suchaneck, G.; Gerlach, G. *Integrated Ferroelectrics* **2011**, *123*, 75.

(178) Byrne, D.; Schilling, A.; Scott, J. F.; Gregg, J. M. *Nanotechnology* **2008**, *19*, 165608.

(179) Cojocaru, C. V.; Harnagea, C.; Pignolet, A.; Rosei, F. *IEEE Transactions on Nanotechnology* **2006**, *5*, 470.

(180) Shin, H.-J.; Choi, J. H.; Yang, H. J.; Park, Y. D.; Kuk, Y.; Kang, C.-J. *Appl. Phys. Lett.* **2005**, *87*, 113114.

(181) Lu, X.; Kim, Y.; Goetze, S.; Li, X.; Dong, S.; Werner, P.; Alexe, M.; Hesse, D. *Nano Lett.* **2011**, 3202.

(182) Rodriguez, B. J.; Gao, X. S.; Liu, L. F.; Lee, W.; Naumov, II; Bratkovsky, A. M.; Hesse, D.; Alexe, M. *Nano Lett.* **2009**, *9*, 1127.

(183) Lee, W.; Alexe, M.; Nielsch, K.; Gösele, U. *Chem. Mater.* **2005**, *17*, 3325.

(184) Kim, Y.; Kumar, A.; Tselev, A.; Kravchenko, I. I.; Han, H.; Vrejoiu, I.; Lee, W.; Hesse, D.; Alexe, M.; Kalinin, S. V.; Jesse, S. *ACS Nano* **2011**, *5*, 9104.

(185) Kim, Y.; Kumar, A.; Ovchinnikov, O.; Jesse, S.; Han, H.; Pantel, D.; Vrejoiu, I.; Lee, W.; Hesse, D.; Alexe, M.; Kalinin, S. V. *ACS Nano* **2011**, *6*, 491.

(186) Kim, H.-C.; Park, S.-M.; Hinsberg, W. D. *Chem. Rev.* **2009**, *110*, 146.

(187) Kim, J. K.; Yang, S. Y.; Lee, Y.; Kim, Y. *Prog. Polym. Sci.* **2010**, *35*, 1325.

(188) Hamley, I. W. *Nanotechnology* **2003**, *14*, R39.

(189) Herr, D. J. C. *J. Mater. Res.* **2011**, *26*, 122.

(190) Park, S.-M.; Liang, X.; Harteneck, B. D.; Pick, T. E.; Hiroshiba, N.; Wu, Y.; Helms, B. A.; Olynick, D. L. *ACS Nano* **2011**, *5*, 8523.

(191) Jeong, J. W.; Park, W. I.; Do, L.-M.; Park, J.-H.; Kim, T.-H.; Chae, G.; Jung, Y. S. *Advanced Materials* **2012**, n/a.

(192) Akcoltekin, E.; Peters, T.; Meyer, R.; Duvenbeck, A.; Klusmann, M.; Monnet, I.; Lebius, H.; Schleberger, M. *Nat Nano* **2007**, *2*, 290.

(193) Wang, Z. L. *Adv. Mater.* **2012**, Early view.

(194) Wang, Z. L. *Adv. Mater.* **2012**, *24*, 280.

(195) Wang, Z. L.; Song, J. *Science* **2006**, *312*, 242.

(196) Scott, J. F. *Ferroelectrics* **2005**, *314*, 207.

(197) Lin, Y.; Liu, Y.; Sodano, H. A. *Appl. Phys. Lett.* **2009**, *95*, 122901.

(198) Im, B.; Jun, H.; Lee, K. H.; Lee, S.-H.; Yang, I. K.; Jeong, Y. H.; Lee, J. S. *Chem. Mater.* **2010**, *22*, 4806.

(199) Hwichan, J.; Badro, I.; Kyung Hee, L.; Il Kyu, Y.; Yoon Hee, J.; Jae Sung, L. *Nanotechnology* **2012**, *23*, 135602.

(200) Chen, Y.-Z.; Liu, T.-H.; Chen, C.-Y.; Liu, C.-H.; Chen, S.-Y.; Wu, W.-W.; Wang, Z. L.; He, J.-H.; Chu, Y.-H.; Chueh, Y.-L. *ACS Nano* **2012**, *6*, 2826.

(201) Im, B.; Jun, H.; Lee, K. H.; Lee, J. S. *CrystEngComm* **2011**, *13*, 7212.

(202) Kalinin, S. V.; et al. *Rep. Prog. Phys.* **2010**, *73*, 056502.

(203) Gruverman, A.; Kalinin, S. V. Piezoresponse force microscopy and recent advances in nanoscale studies of ferroelectrics. In *Frontiers of Ferroelectricity*, 2007; pp 107.

(204) Bocher, L.; Gloter, A.; Crassous, A.; Garcia, V.; March, K.; Zobelli, A.; Valencia, S.; Enouz-Vedrenne, S.; Moya, X.; Marthur, N. D.; Deranlot, C.; Fusil, S.; Bouzehouane, K.; Bibes, M.; Barthélémy, A.; Colliex, C.; Stéphan, O. *Nano Lett.* **2011**, *12*, 376.

(205) Jia, C.-L.; Mi, S.-B.; Urban, K.; Vrejoiu, I.; Alexe, M.; Hesse, D. *Nat Mater* **2008**, *7*, 57.

(206) Nelson, C. T.; Gao, P.; Jokisaari, J. R.; Heikes, C.; Adamo, C.; Melville, A.; Baek, S.-H.; Folkman, C. M.; Winchester, B.; Gu, Y.; Liu, Y.; Zhang, K.; Wang, E.; Li, J.; Chen, L.-Q.; Eom, C.-B.; Schlom, D. G.; Pan, X. *Science* **2011**, *334*, 968.

(207) Schilling, A.; Byrne, D.; Catalan, G.; Webber, K. G.; Genenko, Y. A.; Wu, G. S.; Scott, J. F.; Gregg, J. M. *Nano Lett.* **2009**, *9*, 3359.

(208) Jesse, S.; Baddorf, A. P.; Kalinin, S. V. *Appl. Phys. Lett.* **2006**, *88*, 062908.

(209) Dunn, S.; Whatmore, R. W. *J. Eur. Ceram. Soc.* **2002**, *22*, 825.

(210) Dunn, S.; Zhang, Q.; Whatmore, R. W. *Integrated Ferroelectrics* **2002**, *46*, 87.

(211) Rodriguez, B. J.; Jesse, S.; Alexe, M.; Kalinin, S. V. *Adv. Mater.* **2008**, *20*, 109.

(212) Ivry, Y.; Chu, D.; Durkan, C. *Appl. Phys. Lett.* **2009**, *94*, 162903.

(213) Polking, M. J.; Han, M.-G.; Yourdkhani, A.; Petkov, V.; Kisielowski, C. F.; Volkov, V. V.; Zhu, Y.; Caruntu, G.; Alivisatos, A. P.; Ramesh, R. *Nature Materials* **2012**, *11*, 700.

(214) Shiratori, Y.; Pithan, C.; Dornseiffer, J.; Waser, R. *Journal of Raman Spectroscopy* **2007**, *38*, 1300.

(215) Shiratori, Y.; Pithan, C.; Dornseiffer, J.; Waser, R. *Journal of Raman Spectroscopy* **2007**, *38*, 1288.

(216) Tenne, D. A.; Turner, P.; Schmidt, J. D.; Biegalski, M.; Li, Y. L.; Chen, L. Q.; Soukiassian, A.; Trolier-McKinstry, S.; Schlom, D. G.; Xi, X. X.; Fong, D. D.; Fuoss, P. H.; Eastman, J. A.; Stephenson, G. B.; Thompson, C.; Streiffer, S. K. *Phys. Rev. Lett.* **2009**, *103*, 177601.

(217) Tenne, D. A.; Bruchhausen, A.; Lanzillotti-Kimura, N. D.; Fainstein, A.; Katiyar, R. S.; Cantarero, A.; Soukiassian, A.; Vaithyanathan, V.; Haeni, J. H.; Tian, W.; Schlom, D. G.; Choi, K. J.; Kim, D. M.; Eom, C. B.; Sun, H. P.; Pan, X. Q.; Li, Y. L.; Chen, L. Q.; Jia, Q. X.; Nakhmanson, S. M.; Rabe, K. M.; Xi, X. X. *Science* **2006**, *313*, 1614.

(218) Kretschmer, R.; Binder, K. *Phys Rev B* **1979**, *20*, 1065.

(219) Alexe, M.; Harnagea, C.; Visinoiu, A.; Pignolet, A.; Hesse, D.; Gosele, U. *Scripta Mater.* **2001**, *44*, 1175.

(220) Dawber, M.; Chandra, P.; Littlewood, P. B.; Scott, J. F. *J. Phys.: Condens. Matter* **2003**, *15*, L393.

(221) Shaw, T. M.; Trolier-McKinstry, S.; McIntyre, P. C. *Annu. Rev. Mater. Sci.* **2000**, *30*, 263.

(222) Tybell, T.; Ahn, C. H.; Triscone, J. M. *Appl. Phys. Lett.* **1999**, *75*, 856.

(223) Jiang, B.; Peng, J. L.; Bursill, L. A.; Zhong, W. L. *J. Appl. Phys.* **2000**, *87*, 3462.

(224) Kohiki, S.; Takada, S.; Shimizu, A.; Yamada, K.; Higashijima, H.; Mitome, M. *J. Appl. Phys.* **2000**, *87*, 474.

(225) Junquera, J.; Ghosez, P. *Nature* **2003**, *422*, 506.

(226) Zhong, W. L.; Wang, Y. G.; Zhang, P. L.; Qu, B. D. *Phys Rev B* **1994**, *50*, 698.

(227) Wang, Y. G.; Zhong, W. L.; Zhang, P. L. *Phys Rev B* **1995**, *51*, 17235.

(228) Wang, Y. G.; Zhong, W. L.; Zhang, P. L. *Solid State Commun.* **1994**, *92*, 519.

(229) Sun, W. *J. Appl. Phys.* **2006**, *100*, 083503.

(230) Basun, S. A.; Cook, G.; Reshetnyak, V. Y.; Glushchenko, A. V.; Evans, D. R. *Phys Rev B* **2011**, *84*, 024105.

(231) Hoshina, T.; Kakemoto, H.; Tsurumi, T.; Wada, S.; Yashima, M. *J. Appl. Phys.* **2006**, *99*, 054311.

(232) Huang, L.; Jia, Z.; Kymissis, I.; O'Brien, S. *Adv. Funct. Mater.* **2010**, *20*, 554.

(233) Singh, S. *Advanced Science Letters* **2012**, *11*, 39.

(234) Smith, M. B.; Page, K.; Siegrist, T.; Redmond, P. L.; Walter, E. C.; Seshadri, R.; Brus, L. E.; Steigerwald, M. L. *J. Am. Chem. Soc.* **2008**, *130*, 6955.

(235) Son, J. Y.; Jung, I. *J. Am. Ceram. Soc.* **2012**, *95*, 480.

(236) Suyal, G.; Colla, E.; Gysel, R.; Cantoni, M.; Setter, N. *Nano Lett.* **2004**, *4*, 1339.

(237) Naumov, I. I.; Fu, H. *Phys. Rev. Lett.* **2005**, *95*, 247602.

(238) Spanier, J. E.; Kolpak, A. M.; Urban, J. J.; Grinberg, I.; Ouyang, L.; Yun, W. S.; Rappe, A. M.; Park, H. *Nano Lett.* **2006**, *6*, 735.

(239) Rabe, K.; Dawber, M.; Lichtensteiger, C.; Ahn, C.; Triscone, J.-M. Modern Physics of Ferroelectrics: Essential Background Physics of Ferroelectrics. In *Physics of Ferroelectrics: A Modern Perspective*; Springer Berlin / Heidelberg, 2007; Vol. 105; pp 1.

(240) Beier, C. W.; Cuevas, M. A.; Brutchey, R. L. *Langmuir* **2009**, *26*, 5067.

(241) Li, D.; Zhao, M. H.; Garra, J.; Kolpak, A. M.; Rappe, A. M.; Bonnell, D. A.; Vohs, J. M. *Nat Mater* **2008**, *7*, 473.

(242) Louis, L.; Gemeiner, P.; Ponomareva, I.; Bellaiche, L.; Geneste, G.; Ma, W.; Setter, N.; Dkhil, B. *Nano Lett.* **2010**, *10*, 1177.

(243) Yasinov, R.; Nitzani, M.; Berger, S. *Ferroelectrics* **2009**, *390*, 153

(244) Qi, Y.; Kim, J.; Nguyen, T. D.; Lisko, B.; Purohit, P. K.; McAlpine, M. C. *Nano Lett.* **2011**, *11*, 1331.

(245) Lines, M. E.; Glass, A. M. Applications of Ferroelectrics. In *Principles and Applications of Ferroelectrics and Related Materials*; Oxford University Press: Oxford, 1977; pp 559.

(246) Setter, N.; Damjanovic, D.; Eng, L.; Fox, G.; Gevorgian, S.; Hong, S.; Kingon, A.; Kohlstedt, H.; Park, N. Y.; Stephenson, G. B.; Stolitchnov, I.; Taganstev, A. K.; Taylor, D. V.; Yamada, T.; Streiffer, S. *J. Appl. Phys.* **2006**, *100*, 051606.

(247) Hadnagy, D. Making ferroelectric memories. In *The Industrial Physicist*; American Institute of Physics, 1999; Vol. 5; pp 26.

(248) Whatmore, R. W. *Ferroelectrics* **1991**, *118*, 241.

(249) Fang, J.; Frederich, H.; Pilon, L. *J. Heat Transfer* **2010**, *132*, 092701.

(250) Lang, S. B. *Phys. Today* **2005**, *58*, 31.

(251) Scott, J. F. *Integrated Ferroelectrics* **2000**, *31*, 139.

(252) Chanthbouala, A.; Crassous, A.; Garcia, V.; Bouzehouane, K.; Fusil, S.; Moya, X.; Allibe, J.; Dlubak, B.; Grollier, J.; Xavier, S.; Deranlot, C.; Moshar, A.; Proksch, R.; Mathur, N. D.; Bibes, M.; Barthelemy, A. *Nat Nano* **2012**, *7*, 101.

(253) Das, S.; Appenzeller, J. *Nano Lett.* **2011**, *11*, 4003.

(254) Kusuma, D. Y.; Nguyen, C. A.; Lee, P. S. *The Journal of Physical Chemistry B* **2010**, *114*, 13289.

(255) Hoffman, J.; Pan, X.; Reiner, J. W.; Walker, F. J.; Han, J. P.; Ahn, C. H.; Ma, T. P. *Adv. Mater.* **2010**, *22*, 2957.

(256) Lee, D.; Yang, S. M.; Kim, T. H.; Jeon, B. C.; Kim, Y. S.; Yoon, J.-G.; Lee, H. N.; Baek, S. H.; Eom, C. B.; Noh, T. W. *Adv. Mater.* **2012**, *24*, 402.

(257) Bilc, D. I.; Novaes, F. D.; Íñiguez, J.; Ordejón, P.; Ghosez, P. *ACS Nano* **2012**, *6*, 1473.

(258) Maksymovych, P.; Morozovska, A. N.; Yu, P.; Eliseev, E. A.; Chu, Y.-H.; Ramesh, R.; Baddorf, A. P.; Kalinin, S. V. *Nano Lett.* **2011**, *12*, 209.

(259) Ko, H.; Ryu, K.; Park, H.; Park, C.; Jeon, D.; Kim, Y. K.; Jung, J.; Min, D.-K.; Kim, Y.; Lee, H. N.; Park, Y.; Shin, H.; Hong, S. *Nano Lett.* **2011**, *11*, 1428.

(260) Gruverman, A.; Wu, D.; Lu, H.; Wang, Y.; Jang, H. W.; Folkman, C. M.; Zhuravlev, M. Y.; Felker, D.; Rzchowski, M.; Eom, C. B.; Tsymbal, E. Y. *Nano Lett.* **2009**, *9*, 3539.

(261) Qi, Y.; Jafferis, N. T.; Lyons, K.; Lee, C. M.; Ahmad, H.; McAlpine, M. C. *Nano Lett.* **2010**, *10*, 524.

(262) Zhou, T.; Zha, J.-W.; Cui, R.-Y.; Fan, B.-H.; Yuan, J.-K.; Dang, Z.-M. *ACS Applied Materials & Interfaces* **2011**, *3*, 2184.

(263) Garrity, K.; Kolpak, A. M.; Ismail-Beigi, S.; Altman, E. I. *Adv. Mater.* **2010**, *22*, 2969.

(264) Almadhoun, M. N.; Bhansali, U. S.; Alshareef, H. N. *J. Mater. Chem.* **2012**, *22*, 11196.

(265) Kim, P.; Doss, N. M.; Tillotson, J. P.; Hotchkiss, P. J.; Pan, M.-J.; Marder, S. R.; Li, J.; Calame, J. P.; Perry, J. W. *ACS Nano* **2009**, *3*, 2581.

(266) Li, J.; Claude, J.; Norena-Franco, L. E.; Seok, S. I.; Wang, Q. *Chem. Mater.* **2008**, *20*, 6304.

(267) Park, K.-I.; Lee, M.; Liu, Y.; Moon, S.; Hwang, G.-T.; Zhu, G.; Kim, J. E.; Kim, S. O.; Kim, D. K.; Wang, Z. L.; Lee, K. J. *Adv. Mater.* **2012**, *24*, 2999.

(268) Tavakkoli K. G., A.; Gotrik, K. W.; Hannon, A. F.; Alexander-Katz, A.; Ross, C. A.; Berggren, K. K. *Science* **2012**, *336*, 1294.

(269) Cha, S.; Kim, S. M.; Kim, H.; Ku, J.; Sohn, J. I.; Park, Y. J.; Song, B. G.; Jung, M. H.; Lee, E. K.; Choi, B. L.; Park, J. J.; Wang, Z. L.; Kim, J. M.; Kim, K. *Nano Lett.* **2011**, *11*, 5142.

Chapter 2

Experimental Methods

2.1 Preparation of Tris(diethyldithiocarbamate) Antimony (III)

All chemicals used in the synthesis were high purity and used without any further purification: antimony trichloride ($SbCl_3$, Alfa Aesar UK, 99.9 %), sodium diethyldithiocarbamate trihydrate ($Na(S_2CNEt_2)_2$, Sigma-Aldrich, ≥98 %), anhydrous methanol (Sigma-Aldrich, 99.8 %), dichloromethane (DCM, Sigma-Aldrich, ≥99.9 %), anhydrous benzene (Sigma-Aldrich, 99.8 %), *n*-hexane (Sigma-Aldrich, ≥97 %). In a typical procedure, a soultion of 1.14 g of $SbCl_3$ (0.005 mol in 25 ml of methanol) was added to a solution containing 3.38 g of sodium diethyldithiocarbamate trihydrate (0.015 mol in methanol) drop wise with constant stirring. The solution was stirred at room temperature for 1 hr until a yellow precipitate of $Sb(S_2CNEt_2)_3$ was formed (Figure 2.1). The precipitate was washed with methanol, filtered and dried overnight at 60 °C (Yield, ~90 %). The compound was re-crystallized from dichloromethane and the melting point of the compound was noted to be 170 °C[1].

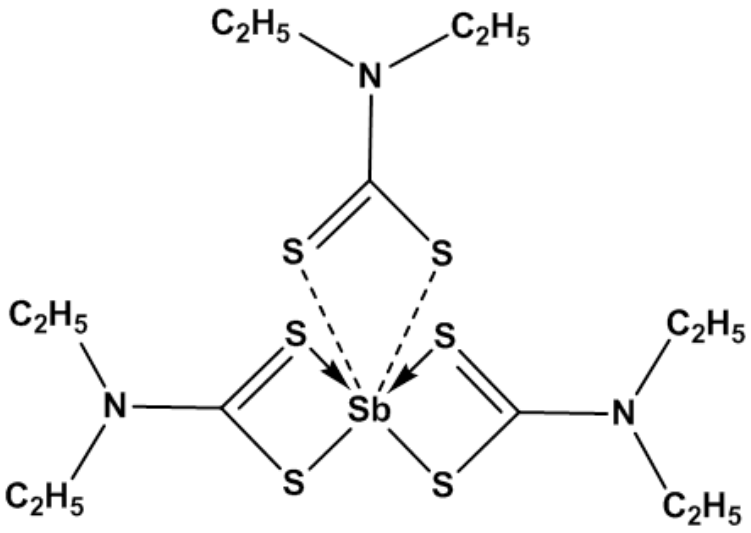

Figure 2.1. Chemical structure of tris(diethyldithiocarbamate) antimony (III), $Sb(S_2CNEt_2)_3$.

2.2 Preapartion of Anodic Aluminium Oxide (AAO) Templates

All the materials used for the fabrication of AAO templates were of high purity and used as received. Al foil (0.5 mm thick, 99.999 %) and lead foil (2 mm, 99.9 %) were purchased from Goodfellow Cambridge Limited, England. Oxalic acid (98 %), copper (II) chloride (97 %), chromium (III) chloride (95 %), phosphoric acid (70 %), sulphuric acid (98 %) and potassium hydroxide (90 %) were purchased from Sigma-Aldrich. AAO templates with mean pore diameter 200 nm were purchased from Whatmann UK. Templates with mean pore diameters 100 and 50 nm were prepared electrochemically by an anodisation process of an aluminium foil, as first described by Masuda and Fukuda in 1995.[2,3,4] The AAO templates were fabricated by a three step process as described below:

(i) *Substrate preparation*. High purity Al foil was cut into circular disks of ~ 15 mm diameter and ultrasonically cleaned in acetone for 30 min at room temperature. The disks were flattened under a pressure of ~ 5000 MPa using a bench-top press and then annealed under vacuum at 450 °C for 5 hr.

(ii) *Anodisation*. Anodisation was carried out in a custom built electrochemical cell, where Al discs were inserted inside the circular slots provided in the cell with the lead counter electrode held at the centre of the cell. The lead electrode was partially immersed in the electrolyte in the electrochemical cell and anodisation was carried out at a constant potential using a dc power supply (*Thurlby Thandar Instruments model EX752M*). In the electrochemical cell, Al discs serve as the anode and lead foil act as the cathode. Anodisation of Al discs was carried out in two stages. For 100 nm AAOs, the 1st anodisation was carried out in 0.3 M oxalic acid at 40 V for 6 hr. at room temperature. The first stage anodisation for 50 nm AAOs was carried out

in 20 wt. % H_2SO_4 at 25 V for 6 hr. at 0 °C. The passive oxide film which forms at the surface of the Al discs was chemically removed by submerging the discs in a solution of chromic acid (5 wt. %) and phosphoric acid (1.8 wt. %) at 60 °C overnight in an air oven. The second stage anodisation of chemically treated 100 and 50 nm AAOs were carried out under similar conditions to the first but over a time period of 16 hr.

(iii) *Post-treatment*. After the anodisation, the aluminium metal present on the back side of the AAOs was removed using a saturated solution of $CuCl_2$ and the oxide barrier layer was removed by treatment with 1.0 M KOH for 20 min. The pores of the AAO templates were widened by immersing the templates in 5 wt. % H_3PO_4. Templates were then dried at 60 °C overnight in an air oven for further use.

As seen in Figure 2.2 an AAO membrane contains a high density of nanopores of between 10^9 and 10^{12} pores per cm^2, which can act as a template for the generation of nanostructures. The thickness of free-standing AAO membranes can be varied from 20 nm to about 300 micrometers. There are some key attributes that make AAO an attractive templating material for 1D nanostructures:[3,4]

- Excellent control over the length and diameter of the nanstructures
- Highly ordered pores with density as high as 10^{11} cm^{-2} and high aspect ratios ranging from 300 to 3000
- Variety of deposition methods can be utilised to fill the pores
- Thermal stability upto 800 °C

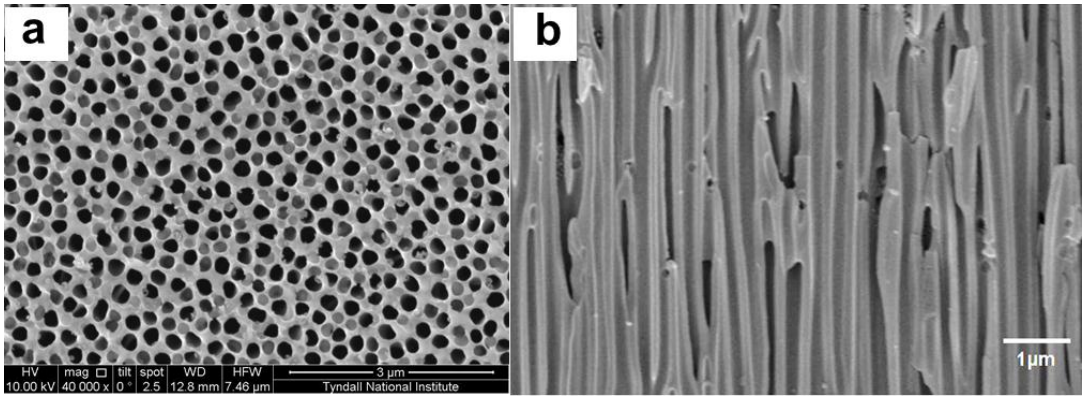

Figure 2.2. SEM images of a 200 nm AAO membrane: (a) plan-view image showing the pores in the membrane and (b) cross-sectional image showing vertical channels in the membrane.

Various approaches, including electrochemical and electroless deposition, sol–gel and chemical vapour deposition have been utilised to produce a range of inorganic nanowires, including metals, metal oxides and semiconductors within the channels of AAO membranes.[3,4] The nanostructures formed were released by either partially or fully etching the membranes using H_3PO_4 or NaOH.[3,4] Sb_2S_3 nanowires formed inside AAO template were released by immersing the template in 0.5 M NaOH for 10 min. at room temperature.

2.2.1 Solventless preparation of arrays of antimony sulphide nanowires

Zhang *et al.*[5] reported a pressure injection process for growing arrays of single crystal nanowires of low melting point metals inside the channels of AAO membranes. Xu *et al.*[6] prepared highly oriented single crystalline Bi_2S_3 nanowires by melting a solid single source precursor inside the channels of AAO membranes under vacuum. Some of the advatages of solventless pressure-injection methods compared to vapour deposition and hydrothermal methods are: (i) low temperature

synthesis, (ii) the absence of solvent and (iii) good control over the size of nanowires.[6]

AAO membranes, with a thickness ~ 50 μm and nominal pore diameters of ~200, 100 and 50 nm, were used as templates to prepare arrays of Sb_2S_3 nanowires. In a typical experiment, an AAO membrane was placed on top of 0.1 g $Sb(S_2CNEt_2)_3$ powder, in a quartz tube and subsequently decomposed under vacuum. The tube was placed inside a block heater and the temperature of the block was raised from room temperature to 180 °C (melting point of the SSP), at a ramp rate of 10 °C min^{-1} with a holding time of 30 min, under vacuum (0.133 Pa). The reaction vessel was decoupled from the pumping system, sealed and the temperature of the block was increased to 300 °C, at a ramp rate of 5 °C min^{-1} and kept for 30 min at this temperature; where the SSP decomposes to form Sb_2S_3. After cooling to room temperature, the membrane was washed with isopropanol and used for further analysis. A schematic illustration of the experimental setup used in the solvent-less pressure-injection method is shown in Figure 2.3.

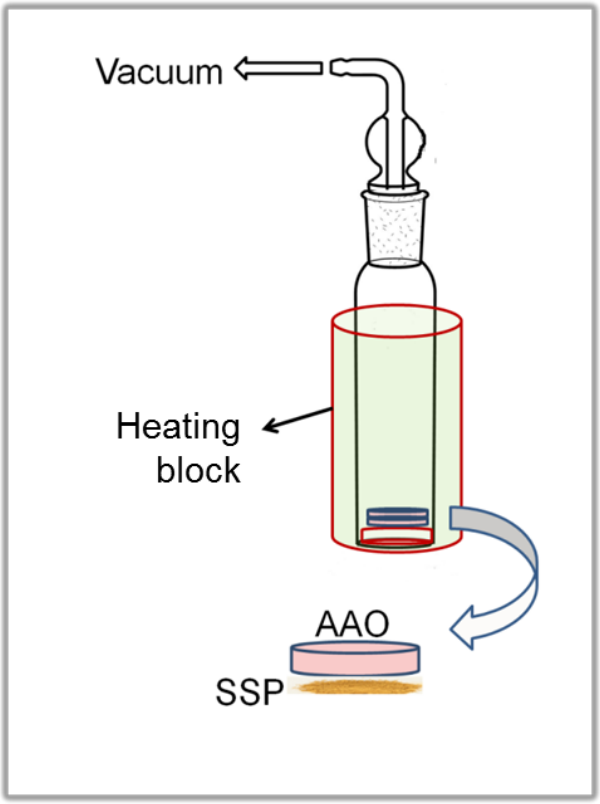

Figure 2.3. Schematic showing equipment used in the solventless synthesis of Sb_2S_3 nanowires within the pores of AAO templates.

2.3 Vapour Phase Growth of SbSI Nanorods

AAO/Ti/Si substrates were prepared by anodisation[2] of Al/Ti/Si substrates (layer thickness: Al 100 nm; Ti 10 nm). Anodisation was carried out in a custom built electrochemical cell with Al/Ti/Si substrate held at a constant separation of 6 cm from the lead counter electrode. The substrate and the lead electrode were partially immersed in the electrolyte (0.3 M oxalic acid) in the electrochemical cell and anodised at a constant potential (40 V) using a dc power supply (*Thurlby Thandar Instruments model EX752M*), at 4 °C for 8 minutes. The substrate was then kept in 5 wt. % phosphoric acid for 5 min to widen the pores, followed by washing using water.

Arrays of SbSI nanorods were synthesised on AAO/Ti/Si substrates by the vapour phase deposition of a mixture of Sb_2S_3 (0.10 g) and SbI_3 powders (0.11 g) with a molar ratio of 1:0.8. The deposition was carried out in a two-zone tube furnace with the source placed in the middle of a quartz tube, while the substrate was placed downstream at an optimum distance of ~15 cm from the source, as shown in Figure 2.4. The quartz tube was then evacuated (0.013 Pa) for 1 hr. to attain a steady vacuum and then sealed. The source and substrate zone temperature were then raised to 400 and 250 °C respectively, at a heating ramp rate of 1 °C min^{-1} and the deposition was carried out for 1 hr. A control experiment was conducted with a Si (001) substrate under similar conditions.

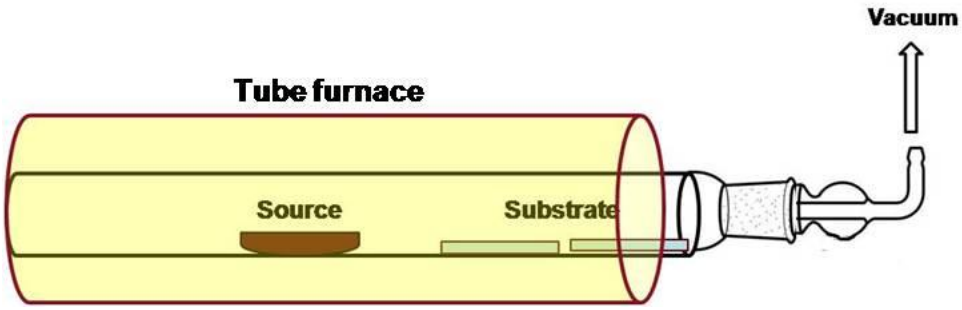

Figure 2.4. Schematic of the apparatus used for the vapour phase growth of SbSI nanorods.

In addition, surface roughened conducting Pt/Ti/Si substrates (layer thickness: Pt, 300 nm and Ti, 100 nm) were used for growing vertically oriented SbSI nanowire arrays. Surface roughness on Pt/Ti/Si substrates was introduced by ultrasonicating the substrates in isopropanol for 30 min. in a sonication bath (*Model Qi-200, Ultrawave Ltd., Cardiff, UK.*) with an operating frequency 40 kHz and an

ultrasonication power 200 W. The substrates were then dried in an air oven at 60 °C overnight. Vapour deposition was carried out under similar condition as with in AAO/Ti/Si substrate. A control experiment was conducted with a smooth Pt/Ti/Si substrate to examine the influence of surface roughness of the substrate on the alignment of nanowires formed.

2.4 Fabrication of Arrays of Lead Zirconate Titanate Nanodots

The diblock copolymer polystyrene-*b*-poly(ethylene oxide) (PS-*b*-PEO) was purchased from Polymer Source and used without further purification. Lead zirconate titanate (PZT) nanodots, of various diameters and spacing, were obtained using two different number average molecular weights (M_n) of PS-*b*-PEO: PZT (42-11, M_n, PS = 42 kg mol^{-1}; M_n, PEO = 11.5 kg mol^{-1}; M_w/M_n = 1.07]M_w: weight-average molecular weight]) and PZT (32-11, M_n, PS = 32 kg mol^{-1}; M_n, PEO = 11 kg mol^{-1}; M_w/M_n = 1.06). N-doped silicon substrates were used for the deposition of the arrays of PZT nanodots. Substrates were cleaned by ultrasonication in acetone and toluene, for 30 min in each solvent, and dried under N_2. PS-*b*-PEO was dissolved in toluene to yield a 0.9 wt. % polymer solution at room temperature. The PS-*b*-PEO thin film was formed by spin coating the polymer solution (3000 rpm for 30 s) onto the substrate. The film was then exposed to toluene vapour (solvent annealing: 3 ml toluene taken in a glass vial placed at the bottom of a closed glass bottle) at 50 °C for 2 hr. After this process, the film was immersed in ethanol at 40 °C for 15 hr. to obtain self-assembled films with long-range order. These self-assembled PS-*b*-PEO thin films were used as templates for the deposition of PZT precursor solutions.

PZT precursor solutions was formulated using lead (II) acetate ($Pb(CH_3COO)_2 \cdot 3H_2O$), Zirconium (IV) acetylacetonate or Zr(acac) and titanium (IV) isopropoxide as starting materials. The transferring, weighing and mixing of the chemicals was done inside an inert atmosphere glove-box to avoid hydrolysis. Lead acetate (0.158 mmol; an excess of 10 % lead acetate was used in order to compensate for the loss of Pb during annealing) was dissolved in 2 ml of glacial acetic acid. Zr(acac) (0.042 mmol) and titanium isopropoxide (0.099 mmol) were dissolved in 8 ml of anhydrous ethanol. This solution was mixed with the acidified lead acetate solution to obtain a PZT precursor solution with a Zr/Ti ratio of 30/70. Dilute solutions of titanium isopropoxide (0.015 mmol) in anhydrous ethanol were then spin coated (6000 rpm for 10 s) onto the PS-*b*-PEO template and left at room temperature overnight to obtain a thin amorphous layer of TiO_2; which helps to prevent the diffusion of Pb into the Si substrate and also enhances the formation of pervoskite PZT.[7] The PZT precursor solution was then spin coated onto this PS-*b*-PEO film at 3000 rpm for 30 s. In order to oxidise the precursor and to remove the polymer, UV/Ozone treatment **(***PSD Pro Series Digital UV Ozone System; Novascan Technologies, Inc., USA***)** was carried out on precursor-loaded templates for 2 hr. Further crystallisation of the PZT nanodots was achieved by annealing the peroxidised samples at 600 °C for 1 hr.

2.5 PFM analysis of Sb_2S_3-AAO Samples

The ferroelectric and piezoelectric properties of individual nanowires inside the pores of AAO membranes were analysed by SS-PFM (*MFP-3D™ software, Asylum Research, Santa Barbara, CA*) using a conductive cantilever (*AC240TM Pt coated*

silicon probe, Olympus). All of the cantilevers used were calibrated to obtain accurate quantitative piezoelectric responses. PFM requires an extremely smooth surface, so the samples first needed to be polished manually and then by Argon ions. A *Gatan Model 691 Precision Ion Polishing System (PIPS™)* was used polish the surface of AAO template samples. The templates were polished using a beam of ions accelerated to 5 kV and an incident angle of 5° to get a final sample thickness of ~ 10 µm. In PFM the electric field inside the sample was generated by the conducting tip and a large back electrode. A 500 nm thick layer of gold, which acted as a back electrode, was evaporated onto one of the polished sides of the Sb_2S_3-AAO samples using *Edwards thermal evaporator (Edwards 306, UK)*. A schematic illustration of the PFM measurement is shown in Figure 2.5.

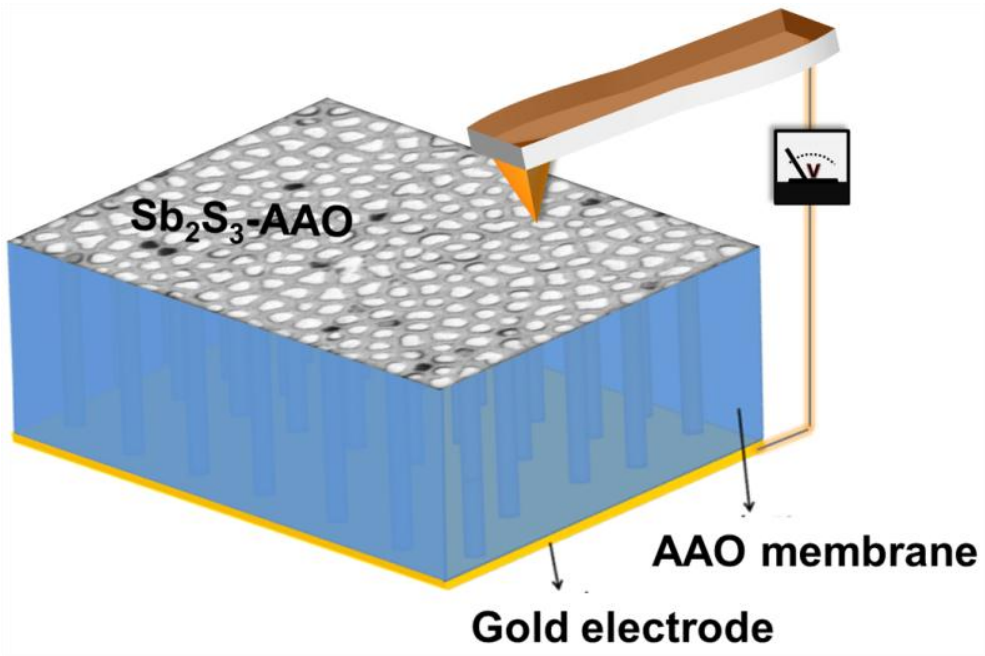

Figure 2.5. Schematic illustration of vertical PFM measurements on Sb_2S_3 nanowires formed inside an AAO membrane.

2.5.1 Acquisition of polarisation-electric field (*P-E*) hysteresis loops

P-E hysteresis measurements were performed on Sb_2S_3-AAO samples. 500 nm thick gold electrodes (0.02 cm^2) were deposited on top of Sb_2S_3-AAO membrane. *P–E* hysteresis loops of Sb_2S_3-AAO samples were measured using a *Precision work station (Radiant Technologies)* at a frequency of 500 Hz. Similarly, *P–E* loop of SbSI nanowire arrays deposited on Pt/Ti/Si substrate was measured at a frequency of 1 kHz.

2.6 Structural and Morphological Characterisation Techniques

2.6.1 X-ray diffraction analysis

X-ray diffraction (XRD) is a structural characterisation technique based on the constructive interference of elastically scattered X-rays in a crystal.[8] XRD occurs when the interplanar distance *d* in a crystal is of the order of the wavelength λ of the X-ray radiation, usually the Cu K_α emission line with a wavelength of 1.54 Å. Diffraction at an angle θ then occurs when Bragg's law is satisfied. Bragg's law is given in equation 2.4 where *n* is an integer value.

$$n\lambda = 2d\sin\theta \qquad (2.1)$$

A plot of diffraction intensity against angle of reflection (2θ) produces a diffraction pattern from which the crystallographic structure of materials can be determined. X-ray diffraction patterns were collected on a *Philips X'Pert diffractometer* using Cu $K_{\alpha 1}$ radiation with an anode current of 35 mA and an accelerating voltage of 40 kV over the angle range 2θ = 10 to 60°, using step sizes of 0.01-0.03 and scan rates 0.05 to 0.2.

2.6.2 Electron microscopy analysis

Electron microscopy is capable of imaging materials at very high magnifications, > 10^6 times.[9] The high resolution capabilities of electron microscopy are due primarily to the very short wavelengths of electrons employed, typically 50 pm – 1nm for SEM and 4 – 15 pm for TEM. Samples of Sb_2S_3 nanowires were analysed using a *FEI 630 NanoSEM,* operated at 5 to 20 kV. High resolution TEM images and selected area electron diffraction (SAED) patterns[10] ([110] zone axis) of Sb_2S_3 nanowires were obtained using a *FEI-TITAN field emission TEM* operated at 300 kV. Energy dispersive X-ray analysis, also known as EDS, EDX or EDAX, is a technique used in conjunction with electron microscopy to identify the elemental composition of a sample or small area of interest on the sample. During EDX analysis, a sample is exposed to an electron beam inside a SEM or TEM. These electrons collide with the electrons within the sample, causing some of them to be knocked out of their orbits. The vacated positions are filled by higher energy electrons which emit characteristic x-rays in the process. By analysing the emitted x-rays, the elemental composition of the sample can be determined. The elemental compositions of Sb_2S_3 nanowires were obtained using a *FEI-TITAN field emission TEM* fitted with an *Oxford INCA EDX detector*. The morphologies and elemental compositions of SbSI and PZT nanodot samples were analysed using a *FEI Quanta 650 FEG-SEM* fitted with an *Oxford INCA EDX detector*. High resolution TEM analysis of SbSI and PZT samples was performed on a *JEOL-JEM 2100 TEM* operated at 200 kV, fitted with an *Oxford INCA EDX detector*. The SAED patterns of SbSI nanowires formed on AAO/Ti/Si and Pt/Ti/Si substrates were obtained along the [010] and [100] zone axes respectively.

2.6.3 X-ray photoelectron spectroscopy

X-ray photoelectron spectroscopy (XPS) is a surface analysis (between 50-70 Å) technique used to determine quantitative atomic composition and chemical environment of a material.[11] XPS analysis is capable of quantifying a material's composition as accurate as ~ 0.1 at%, as well as providing valuable information on the oxidation states of elements present in a material. XPS analysis of PZT nanodot samples was performed on a *VSW Atomtech system* with twin anode (Al/Mg) X-ray source. Survey spectra were collected at a pass-energy of 100 eV, step size of 0.7 eV and a dwell time of 100 μs. Core-level spectra were acquired as an average of 15 scans at a pass-energy of 50 eV, step size of 0.2 eV and a dwell time of 100 μs. The core-level spectra of each element were deconvoluted and fitted using *VSW spectra presenter software (version 8.0-B-2).*

2.7 References

(1) Lalia-Kantouri, M.; Manoussakis, G. *J. Therm. Anal. Calorim.* **1984**, *29*, 1151.

(2) Masuda, H.; Fukuda, K. *Science* **1995**, *268*, 1466.

(3) Martin, C. R. *Science* **1994**, *266*, 1961.

(4) Routkevitch, D.; Tager, A. A.; Haruyama, J.; Almawlawi, D.; Moskovits, M.; Xu, J. M. *Ieee Transactions on Electron Devices* **1996**, *43*, 1646.

(5) Zhang, Z.; Gekhtman, D.; Dresselhaus, M. S.; Ying, J. Y. *Chem. Mater.* **1999**, *11*, 1659.

(6) Xu, J.; Petkov, N.; Wu, X.; Iacopino, D.; Quinn, A. J.; Redmond, G.; Bein, T.; Morris, M. A.; Holmes, J. D. *Chemphyschem* **2007**, *8*, 235.

(7) Muralt, P.; Maeder, T.; Sagalowicz, L.; Hiboux, S.; Scalese, S.; Naumovic, D.; Agostino, R. G.; Xanthopoulos, N.; Mathieu, H. J.; Patthey, L.; Bullock, E. L. *J. Appl. Phys.* **1998**, *83*, 3835.

(8) Kittel, C.; McEuen, P. *Introduction to solid state physics*; Wiley New York, 1996; Vol. 7.

(9) Yao, N.; Wang, Z. L. *Handbook of microscopy for nanotechnology*; Kluwer Academic Pub, 2005.

(10) Lou, W.; Chen, M.; Wang, X.; Liu, W. *Chem. Mater.* **2007**, *19*, 872.

(11) Vickerman, J. C.; Gilmore, I. S. *Surface analysis: the principal techniques*; Wiley Online Library, 1997.

Chapter 3

Nanoscale Ferroelectric and Piezoelectric Properties of Sb_2S_3 Nanowire Arrays

3.1 Abstract

This chapter discusses the synthesis and characterisation of vertically oriented arrays of antimony sulphide (Sb_2S_3) nanowires. Single crystalline arrays of Sb_2S_3 nanowires, with a preferred <001> orientation, was synthesised using anodic aluminium oxide templates by a solventless method; using the single source precursor, antimony (III) tris(diethyldithiocarbamate). The piezoelectric and ferroelectric switching behaviour in individual Sb_2S_3 nanowires was demonstrated, for the first time, using piezoresponse force microscopy. Sb_2S_3 nanowires showed a maximum piezo coefficient, $d_{33(eff)}$, around 2 pm V^{-1}. In addition, an enhancement in the spontaneous polarisation of the Sb_2S_3 nanowires was observed compared to bulk Sb_2S_3 single crystals, due to the defect-free, single-crystalline nature of the nanowires synthesised. The ferroelectric switching in Sb_2S_3 nanowires was found to occur via a 180° domain reversal due to the preferred orientation of the nanowires along the polar *c*-axis.

3.2 Background

3.2.1 Antimony sulphide (Sb_2S_3)

Recent advances in nano-ferroelectrics, especially their synthesis and characterisation, have provided an impetus for the development of novel nanoscale ferroelectric/piezoelectric materials and devices.[1-4] Most of the interest in nanoscale ferroelectric research has primarily focused on perovskite-based complex oxide materials,[1-3] while non-oxide based ferroelectric materials so far have been left unexplored. Antimony sulphide or stibnite (Sb_2S_3) has been widely studied over the past decade due to its high photoconductivity.[5] The band gap of Sb_2S_3 is between 1.88 to 2.5 eV, covering the visible and near-infrared region of the solar spectrum.[6]

The excellent optical properties of Sb_2S_3 make it a potential candidate for photocatalytic[7] and solar cell electrode applications[8,9]. Theoretical simulations show that the highly anisotropic ion polarisability in sulphides can generate ferroelectric phase transitions.[10] Calculations of the polarisability constants of Sb_2S_3 show that a stibnite-type (Sb_2S_3) structure is favourable for a ferroelectric phase transition.[10] Grigas *et al.* reported that Sb_2S_3 exhibits two ferroelectric phase transitions at 292 and 420 K.[11] The structural change from D_{2h}^{16} to C_{2v}^{9} accounts for the phase transition at 420 K, but no structural change has been reported for the 292 K transition.[6,11] Sb_2S_3 is polar at room temperature and the structure contains infinite ribbons of $(Sb_4S_6)_n$ along the *c*-axis.[6] These $(Sb_4S_6)_n$ chains are linked by a '2_1' screw axis in such a way that the antimony in one chain is connected to the sulphur in the neighbouring chain.[6,12] The origin of ferroelectricity in Sb_2S_3 is associated with the small dipole changes in the coordination sphere of Sb and S atoms along the *c*-axis in the $(Sb_4S_6)_n$ chains.[10,11,13] Due to the anisotropy of the $(Sb_4S_6)_n$ chains along the *c*-axis the observed polarisation is largely anisotropic, which was demonstrated by Grigas and Karpus.[10,11,13] This anisotropy in the dielectric behaviour of Sb_2S_3 sparked my interest to explore the ferroelectric and piezoelectric behaviour of this material at the nanoscale, as potentially *c*-axis-oriented single crystalline Sb_2S_3 nanowires could show highly anisotropic ferroelectric and even piezoelectric properties.

3.2.2 Synthesis of antimony sulphide nanostructures

Although the synthesis and characterisation of various types of Sb_2S_3 nanostructures have been the basis of numerous studies,[14-16] no data have been reported on their nanoscale ferroelectric or piezoelectric behaviour. Among

ferroelectric nanostructures, one-dimensional (1D) structures such as nanowires, nanorods and nanotubes have been widely explored from both theoretical and application viewpoints.[17-20] Studies on the size-dependant properties in ferroelectrics have revealed that 1D nanostructures can enhance or reduce the ferroelectric and piezoelectric response depending on their size and morphology, defects, crystal structure, ferroelectric domain structure *etc.*[18,19] A doubling of the spontaneous polarisation was observed in Rochelle salt nanowires, with a diameter of 30 nm, compared to the bulk due to the uniform polarisation orientation and single crystalline nature of the wires. Precise chemical composition, high crystallinity and uniform geometry are required for defined ferroelectric material properties at the nanoscale.[21]

Preparative routes to Sb_2S_3 nanostructures have included chemical bath deposition,[22] hydrothermal,[16] solvothermal,[23] atomic layer deposition[14] and physical vapour deposition[15] using various precursors. Although the synthesis of various types of Sb_2S_3 1D nanostructures have been the basis of numerous studies,[14,16,23] no work has been reported on the production of arrays of nanowires/rods of Sb_2S_3. Template-directed, 'bottom-up' synthesis is a facile strategy for fabricating nanowires,[24] as their physical dimensions can be precisely controlled and monodisperse samples can be harvested in large quantity. Porous membranes with monodisperse cylindrical pores are used as templates, such as anodic aluminium oxide (AAO), and track-etched polycarbonate membranes.[25,26] AAO template-assisted methods have shown promising possibilities for preparing 1D nanostructures including metal chalcogenides.[14] This approach can provide good control over the lengths and diameters of nanowires, with the potential to generate large arrays of nanostructures

with controlled morphologies.[25] AAO templating is adaptable to a variety of material and device applications. Potential applications of nanowires produced in AAO membranes include electronic and solar power devices.[27] For instance, template grown nanowires have been used to produce arrays of ferroelectric nanocapacitors.[28] AAO membranes have also been used to produce thin-film transistors elements through a combination of sol-gel and electrodeposition methods.[24]

This chapter describes the synthesis of arrays of Sb_2S_3 nanowires within the cylindrical pores of AAO templates (Sb_2S_3-AAO), by a solventless technique utilising the single-source precursor (SSP) antimony (III) tris(diethyldithiocarbamate), $Sb(S_2CNEt_2)_3$. The procedures for synthesising the single-source precursor and the subsequent Sb_2S_3 nanowires were discussed in detail in Chapter 2, Sections 2.1 and 2.2. AAO membranes with nominal pore diameters of ~200 nm, 100 and 50 nm were used as templates to prepare arrays of Sb_2S_3 nanowires. The template-based approach to synthesise arrays of Sb_2S_3 nanowires allows good control over the morphology and geometry of the nanowires.[24] In addition, the use of a template eliminates the agglomeration of nanowires in an ordered array, making it possible to address the ferroelectric functionality of individual Sb_2S_3 nanowires on a one to one basis. The ferroelectric and piezoelectric characteristics of Sb_2S_3 nanowire arrays were studied using Piezoresponse force Microscopy (PFM) as described in Chapter 2, Section 2.5.2.

3.3 Results and Discussion

3.3.1 Thermogravimetric analysis of $Sb(S_2CNEt_2)_3$

Figure 3.1 shows the thermogravimetric analysis (TGA) decomposition profile of the SSP, $Sb(S_2CNEt_2)_3$ under a N_2 atmosphere. The decomposition occurred in a single stage, with the onset of decomposition starting at ~200 °C. The observed residual mass (33 %) for the SSP at 335 °C (theoretical for 0.5 mol Sb_2S_3: 32 %) showed that Sb_2S_3 was the major decomposition product.[29] Based on the TGA data, the optimal decomposition temperature for the SSP was chosen as 300°C.

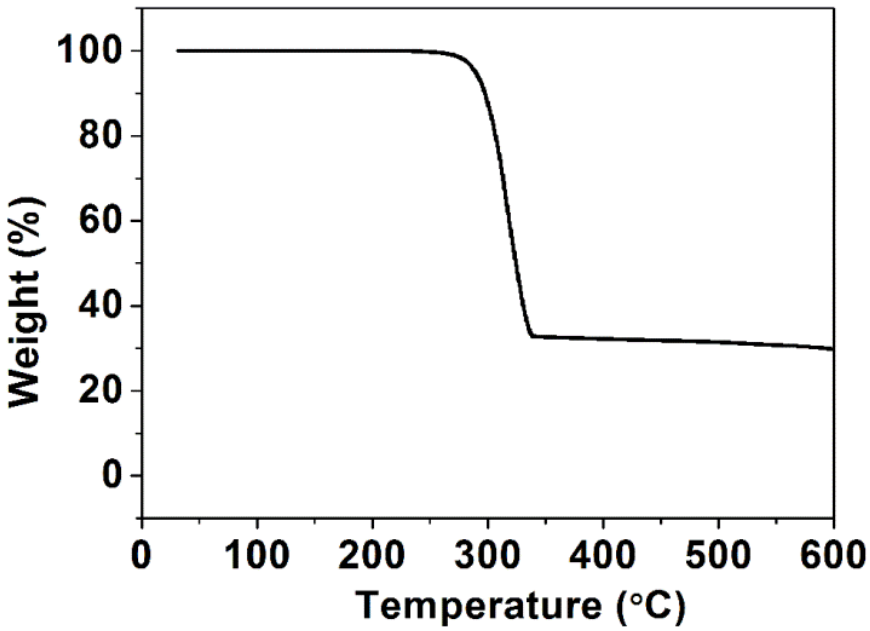

Figure 3.1. TGA data showing the decomposition profile of the $Sb(S_2CNEt_2)_3$in a N_2 atmosphere.

3.3.2 Morphological analysis

The as-synthesised Sb_2S_3-AAO samples generated showed extended growth of Sb_2S_3 nanowires from the AAO pores, as evident from the SEM images (Figures 3.2(a) and 3.2(b)). Figures 3.2(c) and 3.2(d) show that some of the nanowires tended

to merge into Sb_2S_3 microcrystallites when they reach the AAO-air interface (marked in dotted white circle in Figure 3.2(c)).

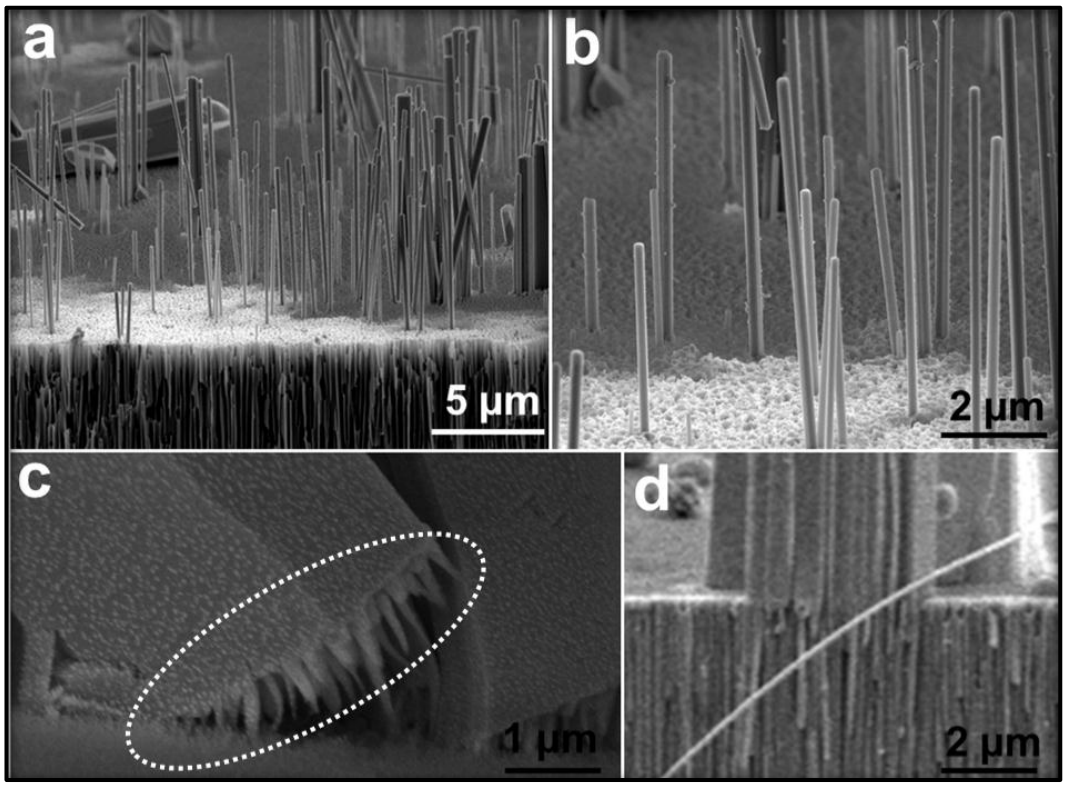

Figure 3.2. SEM images of (a) and (b) Sb_2S_3 nanorods formed on the surface of a 200 nm AAO template surface, highlighting the extended growth of Sb_2S_3 of crystallites from the pores. (c) The interface between an Sb_2S_3 microcrystallite and the AAO surface (dotted white circle shows nanowires up-rooted from the AAO pores) and (d) cross-section of AAO pores filled with Sb_2S_3 nanowires.

In order to expose the Sb_2S_3 nanowires formed inside the AAO pores, and to obtain a smooth surface, the as-synthesised Sb_2S_3-AAO samples were first manually polished followed by Argon ion beam milling. The resulting smooth surfaces on the Sb_2S_3-AAO samples were ideal for PFM analysis. Figure 3.3(a) shows a top-down view of

Sb_2S_3 nanowires, with a mean diameter of approximately 200 nm, within the pores of an AAO template after polishing. Regions with white contrast are Sb_2S_3 filled AAO pores. Cross sections of the samples, thickness 10 μm, were used to analyse the extent of filling of the channels within the membranes with Sb_2S_3 nanowires (Figure 3.3(b)).

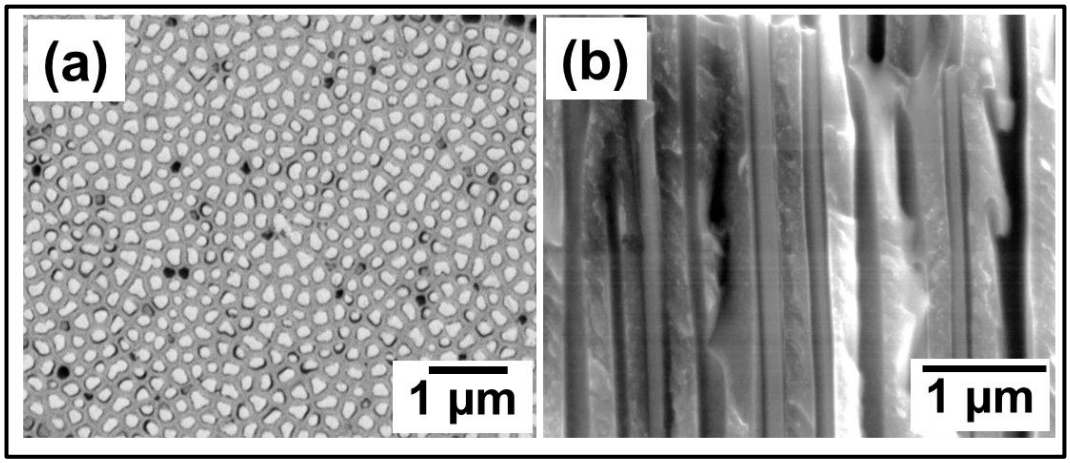

Figure 3.3. SEM images of Sb_2S_3-AAO samples (mean nanowire diameter of 200 nm): (a) plan-view of polished surface and (b) cross-sectional view.

The Sb_2S_3 nanostructures showed radial dimensions in accordance with the nominal channel width of the AAO templates used, *i.e.* mean diameters of 50, 100 and 200 nm (Figure 3.4). The Lorentzian diameter distribution of the Sb_2S_3 nanowires formed inside the AAO templates showed a diameter distribution of 199 ± 16 nm (Figure 3.4(d)), 93 ± 9 nm (Figure 3.4(e)), and 51 ± 6 nm (Figure 3.4(f)) for 200, 100 and 50 nm diameter AAO membranes respectively. The nanowire diameter distributions were calculated from plan-view SEM images of polished Sb_2S_3-AAO samples (Figures 3.4(a), 3.4(b) and 3.4(c)). The extent of pore filling by the Sb_2S_3 nanowires was ~ 80 % across a 50 μm × 50 μm area and length wise ~90 % along a

10 μm long pores, irrespective of the pore diameter, with densities 1.0×10^9, 7.6×10^8, and 4.0×10^8 nanowires per cm^2 for 50, 100 and 200 nm Sb_2S_3-AAO samples respectively.

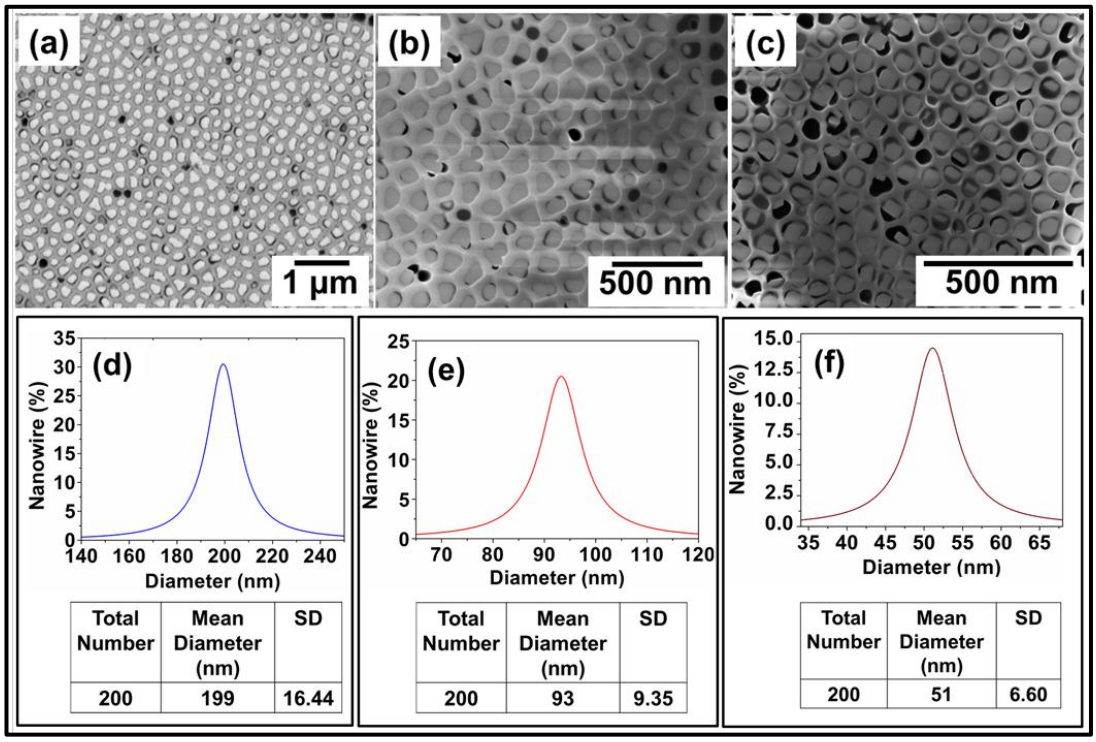

Figure 3.4. Plan-view SEM images of surface polished Sb_2S_3-AAO samples with different mean nanowire diameters: (a) 200 nm, (b) 100 nm and (c) 50 nm. (d), (e) and (f) illustrate the Lorentzian diameter distribution of Sb_2S_3 nanowires inside the 200, 100 and 50 nm AAO membranes, respectively.

3.3.3 Structural and compositional analysis

The crystal structure and phase purity of the materials were characterised by X-ray diffraction (XRD) analysis and performed on polished Sb_2S_3-AAO samples. The XRD pattern shown in Figure 3.5(a) can be indexed to an orthorhombic Sb_2S_3 phase (JCPDS file No: 42-1393), displaying a high intensity reflection at 47.5° from the (002) planes; an indication of the preferred *c*-axis-oriented growth of the Sb_2S_3

nanowires within the pores of the AAO template. Energy dispersive X-ray (EDX) analysis confirmed the chemical composition of the Sb_2S_3 nanowires (Figure 3.5(b)) to be 40.5 and 59.5 at. % for Sb and S respectively, which is close to the theoretical values (Sb 40 %, S 60 %) for Sb_2S_3. The Cu peaks in the EDX spectrum originate from the TEM grid.

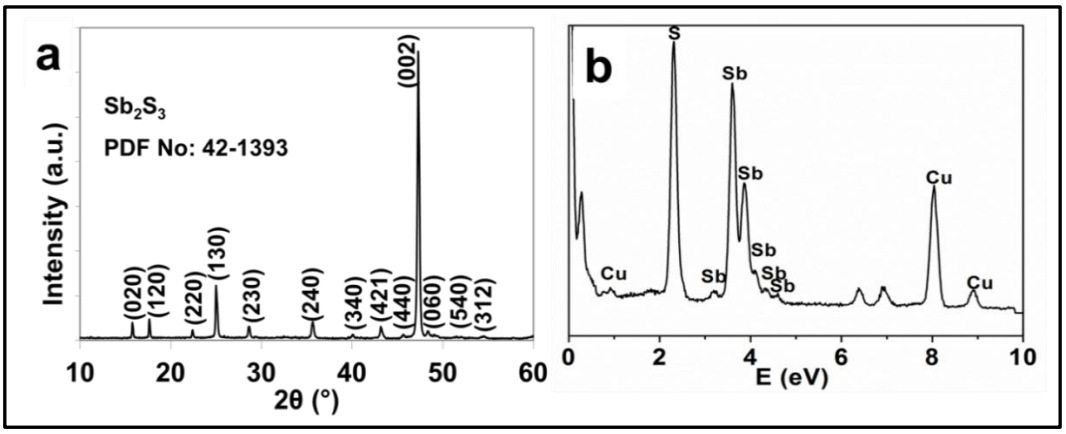

Figure 3.5. (a) XRD pattern of a polished Sb_2S_3-AAO sample, indexed to the orthorhombic Sb_2S_3 structure (JCPDS file No: 42-1393) and (b) EDX spectra of an isolated 200 nm Sb_2S_3 nanowire after removal from an AAO template.

The single crystalline growth of Sb_2S_3 nanowires along the *c*-axis was further confirmed by high resolution TEM analysis. Figures 3.6(a, d, e) show TEM images of 200, 100 and 50 nm Sb_2S_3 nanowires liberated from AAO templates. 200 nm Sb_2S_3 nanowires showed single crystalline nature with a <001> growth direction along the *c*-axis, which supports the XRD data. The presence defects and lattice dislocations were spotted in the TEM images of 100 and 50 nm nanowires.

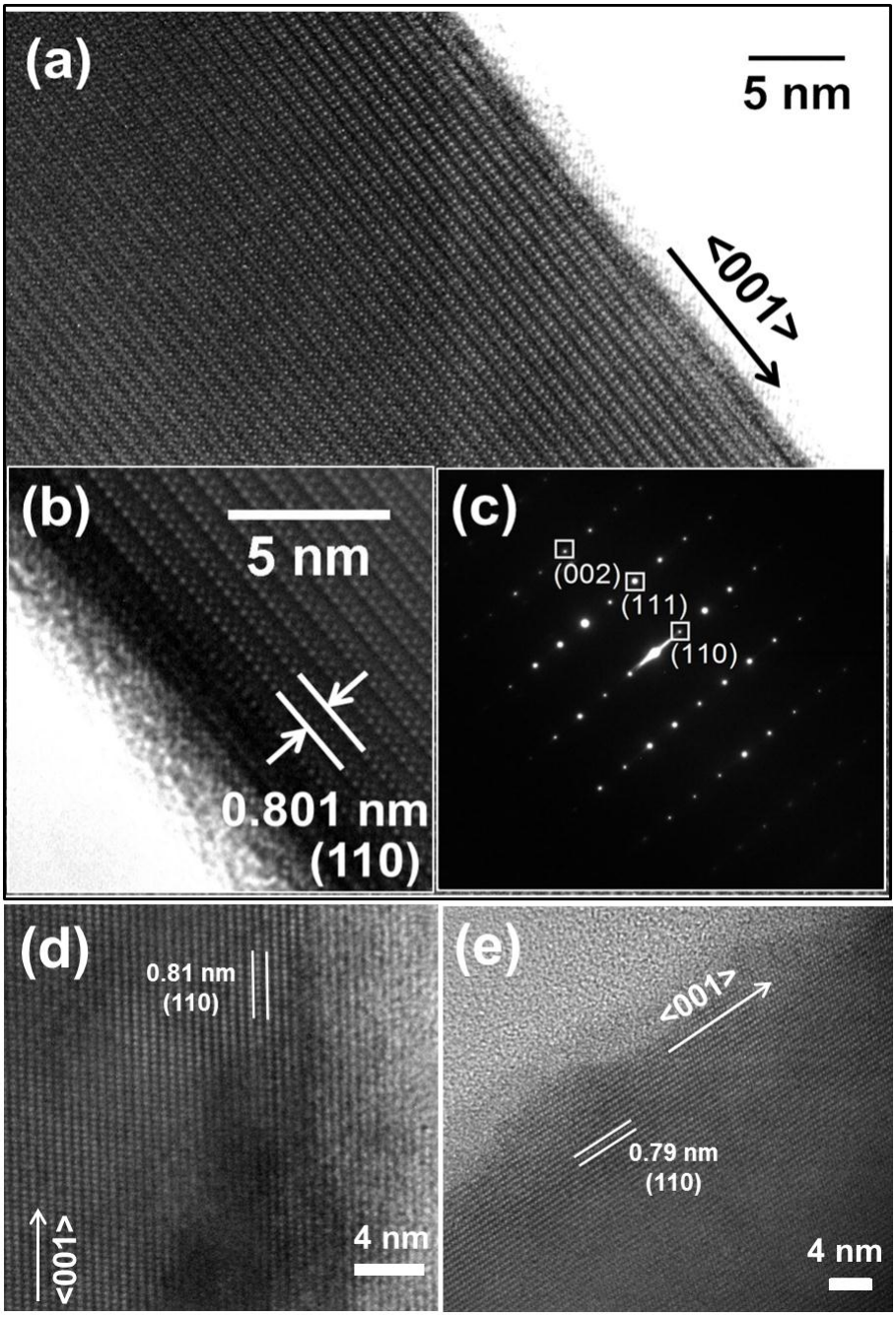

Figure 3.6. (a, d, e) High resolution TEM images of Sb_2S_3 nanowires, liberated from an AAO template with a nominal diameter of 200, 100 and 50 nm respectively, showing a preferred <001> orientation, (b) magnified TEM image of 200 nm nanowire and (c) SAED pattern of the Sb_2S_3 nanowire, obtained in the [110] zone axis, showing the single crystalline nature of the nanowire; the lattice planes shown in SAED pattern can be indexed to orthorhombic Sb_2S_3.

The reflection planes parallel to the Sb_2S_3 nanowire axis shows a lattice fringe spacing of 0.801 nm (Figure 3.6(b)) corresponds to the inter-planar *d*-spacing between the (110) planes of orthorhombic Sb_2S_3.[6] The selected area electron diffraction (SAED) pattern obtained from a Sb_2S_3 nanowire, shown in Figure 3.6(c), in the [110] zone-axis further validates the single crystalline nature of the Sb_2S_3 nanowires; confirming the *c*-axis oriented growth of the nanowires. The lattice planes shown in SAED pattern can be indexed to orthorhombic Sb_2S_3.[6]

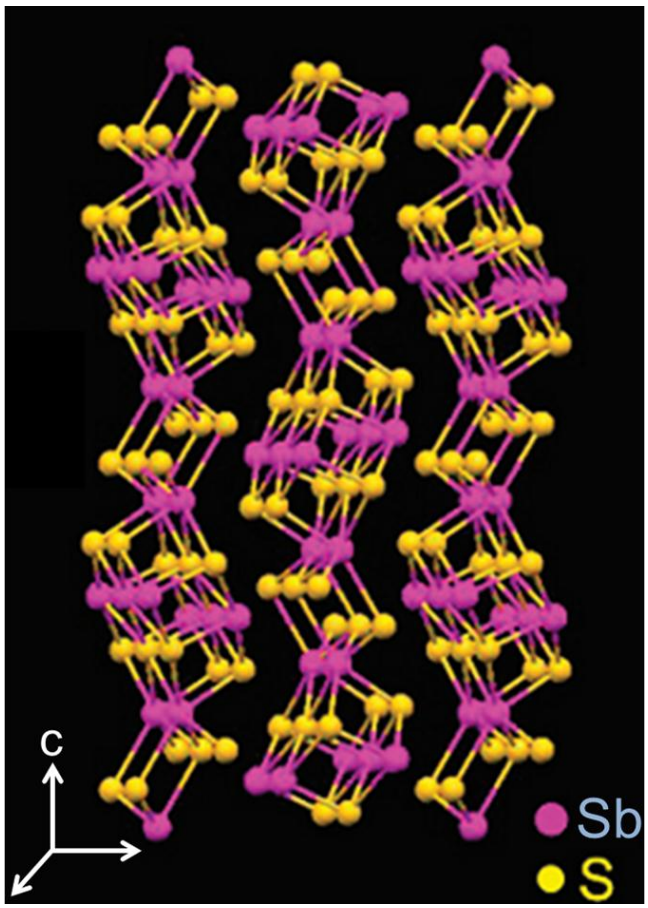

Figure 3.7. Schematic illustration of the crystal structure of Sb_2S_3.[6]

The templating effect of AAO pores drives the formation of single crystalline Sb_2S_3 nanowires. The pores assist the inherent 1D growth of Sb_2S_3 along the *c*-axis. The reason for 1D growth of Sb_2S_3 can be understood from its orthorhombic crystal structure, which usually crystallises as rod, needle, straw or acicular-type morphologies. Crystalline Sb_2S_3 composed of two infinite chains of $(Sb_4S_6)_n$ along the *c*-axis (Figure 3.7), are linked by a '2_1' screw axis (space group of Sb_2S_3 is $Pna2_1$) in such a way that the antimony in one chain connects to the sulphur in the neighbouring chain by a weak van der Waal's bond.[6,12] Thus the bonding between these chains is considerably weaker in the *a*-*b* plane than that within the *c*-plane. This weaker bonding in the *a*-*b* plane leads to a cleavage along the planes parallel to the *c*-axis, *i.e.* (100) or (010) planes, as these planes will have the lowest surface energy compared to the (001) plane.[12,30] As a result Sb_2S_3 tends to grow along the [001] direction and eventually forms into a 1D nanostructure.

3.3.4 Nanoscale ferroelectric and piezoelectric properties of Sb_2S_3 nanowire arrays: PFM analysis

Knowledge of piezo and ferroelectric properties at the nanoscale is a prerequisite to exploit the potential of piezo/ferroelectric nanostructures. PFM has emerged as an effective tool to analyse the electromechanical and ferroelectric response of nanostructured piezo/ferroelectric materials.[31-33] The piezo and ferroelectric responses of Sb_2S_3 nanowires were investigated using piezoresponse force microscopy (PFM). In PFM, an electric field is applied to the sample across a conducting tip and a large back electrode. A schematic representation of the

experimental set-up of PFM analysis on a Sb_2S_3-AAO sample is illustrated in Figure 3.8.

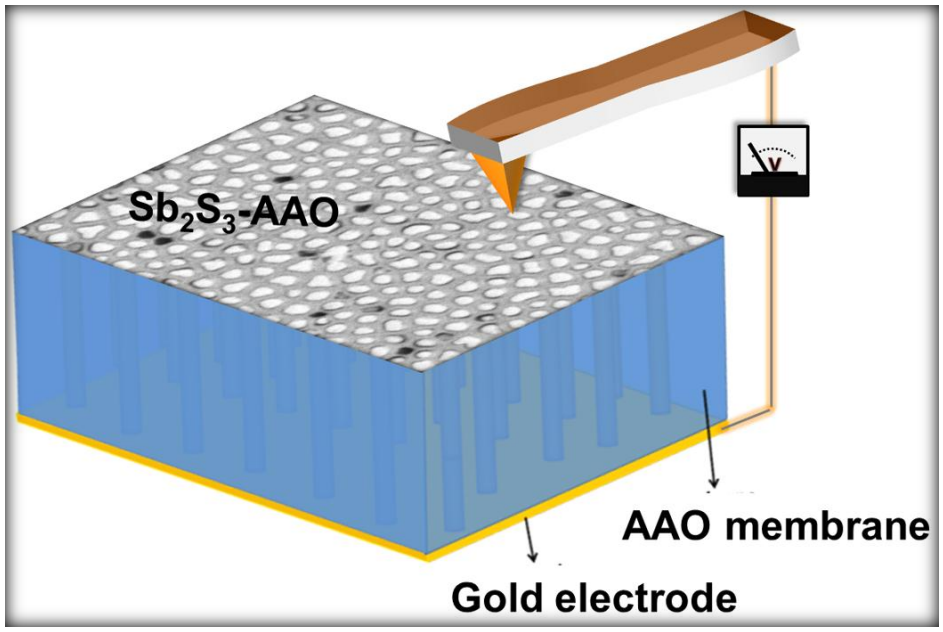

Figure 3.8. Schematic illustration of vertical PFM measurement on a Sb_2S_3-AAO sample.

The conducting PFM tip is brought into contact with the Sb_2S_3-AAO sample surface in contact mode and a dc bias is applied to a small area to induce polarisation on the sample through the probe. In sequence an ac electric field is applied to the same area to detect the magnitude of the piezoelectric response. PFM can provide high special resolution and high localisation of an electric field at the interface between the tip and the ferroelectric surface. The PFM tip will deflect in response to the piezo activity of the material, which either expands or contracts in response to the applied bias. The magnitude and sign of the PFM response can be translated into images. The ferroelectric and piezoelectric functionality of individual Sb_2S_3 nanowires inside

AAO membranes was demonstrated using PFM measurements (in contact mode) on arrays of Sb_2S_3 nanowires in AAO templates along their *c*-axis, at room temperature.

In order to align the polarisation of Sb_2S_3 nanowires, an axial bias voltage of ± 44 V was applied to a 2.5 × 2.5 μm^2 surface area of the Sb_2S_3-AAO samples, between the back electrode and the conducting tip of the PFM in contact mode. Figure 3.9 shows the PFM height profile, the resulting piezo-response amplitude and the phase signal of Sb_2S_3-AAO samples with various mean diameters. The PFM amplitude image is a direct measure of the piezoelectric response of the material. The Sb_2S_3 nanowires, irrespective of their diameter, showed positive domains (white contrast) in the amplitude signal which is a clear indication of the piezo-response in the nanowires due to the out-of plane polarisation of the nanowires. Sb_2S_3 nanowires inside AAO pores with diameters 200, 100 and 50 nm showed a maximum vibration amplitude of ~500, ~350 and ~100 pm, respectively. The piezo amplitude response observed in the Sb_2S_3 nanowires is the contribution from the two oppositely (180°) oriented dipoles (↑↓) along the polar *c*-axis, within the probing volume underneath the tip. 200, 100 and 50 nm Sb_2S_3 nanowires showed out-of plane polarisation (Figure 3.9, piezo amplitude response) meaning that the polarisation was parallel and aligned with the applied electric field, causing a local expansion of the nanowires.[31] Some of the Sb_2S_3 nanowires, regardless of their diameter, showed no piezo response which may be due to the poor accessibility of the PFM tip over the nanowire inside the AAO pores.

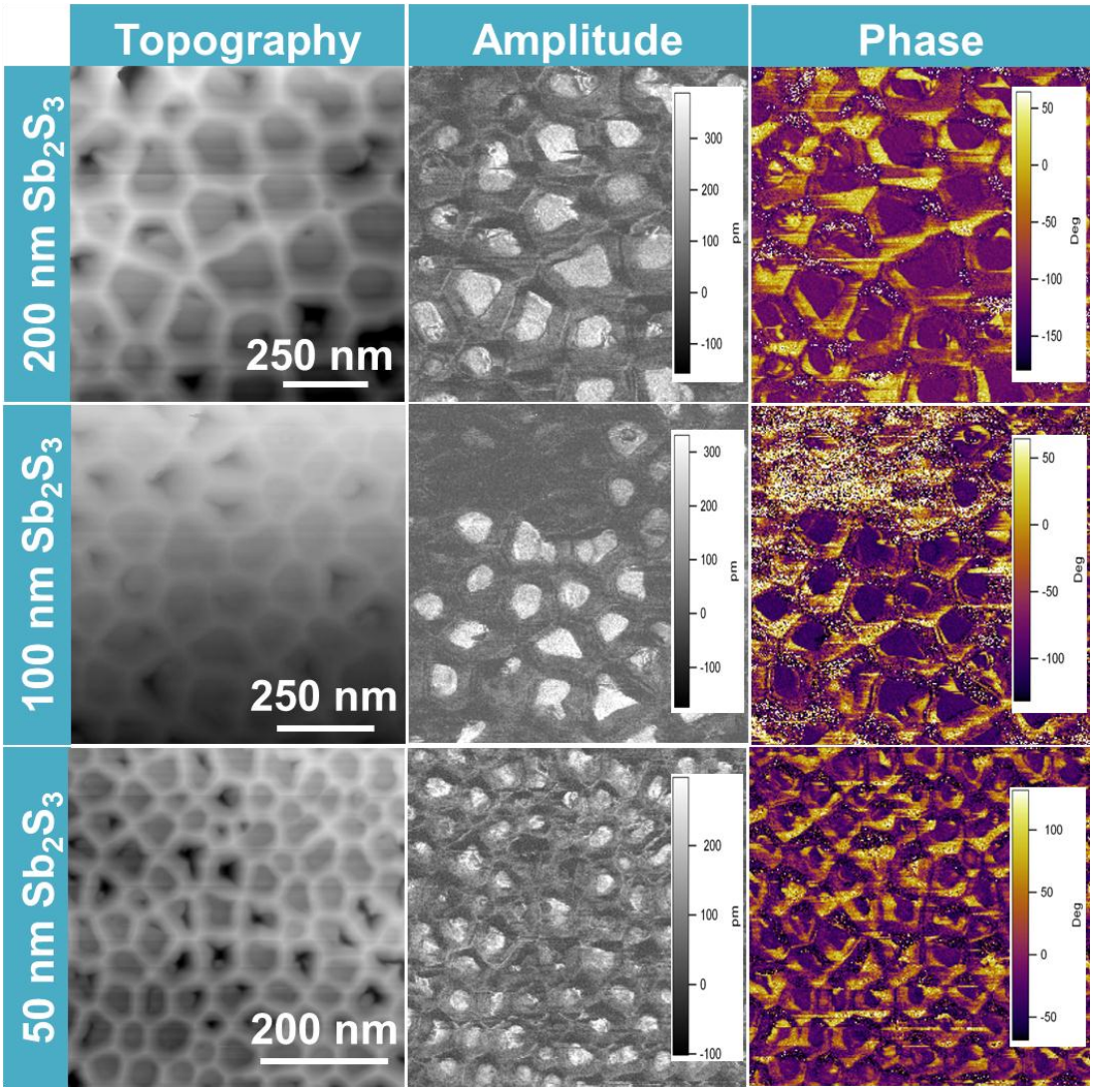

Figure 3.9. PFM images showing topography, amplitude and phase profiles of Sb_2S_3-AAO samples with various mean diameters.

The PFM phase images of Sb_2S_3 nanowires with various diameters (Figure 3.9, phase images) clearly showed a high percentage of uniformly polarised nanowires with single ferroelectric domains; the size of these domains limited by the diameter of the nanowires. The reason for the existence of monodomains can be attributed to the single crystalline (<001> oriented) low defect nature of the Sb_2S_3 nanowires synthesised, as evident from the high resolution TEM images. As *c*-axis (<001>

direction) is the polar axis of the Sb_2S_3 nanowires, a high percentage of ↑ and ↓ polarised 180° domains were formed along the *c*-axis of Sb_2S_3 nanowires.[34-36]

In addition, detailed examination of PFM phase images of Sb_2S_3-AAO samples (Figure 3.10) revealed the presence of multi-domain ferroelectric structure in some of the nanowires. The plausible explanation for the multi-domain nature of some the nanowires is possibly due to the presence of defects on the surface of the nanowires.[31,37]

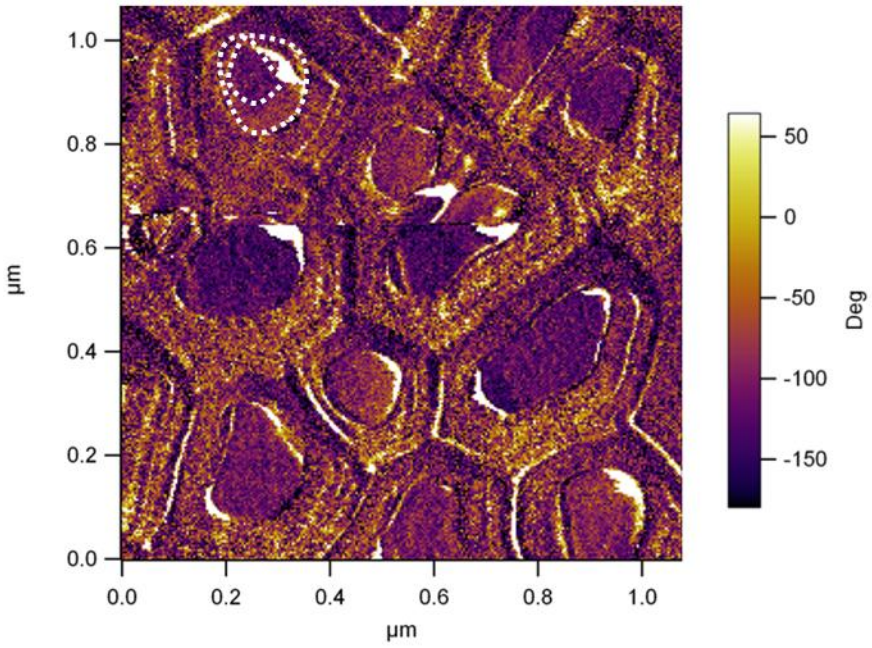

Figure 3.10. PFM phase image of a 200 nm Sb_2S_3-AAO sample showing the presence of multi-domain ferroelectric structure. (The dotted enclosed area represents different domains present on a single nanowire)

3.3.4.1 Ferroelectric and piezoelectric hysteresis loop acquisition

The characteristic of ferroelectric materials is the switching of the polarisation under the application and removal of an electric field.[38] PFM in the imaging mode

(Figure 3.9) only gives the qualitative information on domain patterns and their evolution. However an extended version of PFM, called the switching spectroscopy PFM (SS-PFM) quantitatively addresses the local piezoelectric and ferroelectric switching behaviour in nano-ferroelectrics.[39-41] SS-PFM involves the acquisition of hysteresis loops from a small area (~20 nm^2),[31,32] by positioning the conducting PFM tip at a given location on the surface, to induce local ferroelectric domain nucleation and growth by the application of an electrical field; the signal in turn generates a ferroelectric and piezoelectric hysteresis loop of the specified area. In this work, the piezoelectric hysteresis loops were obtained by positioning the conductive PFM tip on the centre of a chosen Sb_2S_3 nanowire within an AAO pore and an ac voltage of 3.4 V was applied, whilst biasing ± 44 V dc voltages across the nanowire between the PFM tip and the gold back electrode. Applying a small ac voltage through the PFM tip to an individual Sb_2S_3 nanowire inside an AAO pore leads to local structural deformation along the *c*-axis due to a converse piezoelectric effect. The resulting strain and polarisation response from the nanowire surface are detected by the PFM tip to generate a piezoelectric and ferroelectric hysteresis loop respectively. The amplitude of the detected piezoelectric vibration from a Sb_2S_3 nanowire is a direct measure of the piezoelectric coefficient of the nanowire whereas the phase of the signal relates to the polarisation direction present in the nanowires.

The remnant phase and piezo switching hysteresis observed in Sb_2S_3 nanowires with various diameters are shown in Figures 3.11(a) and 3.11(b) respectively. Figure 3.11(a) shows the phase-voltage hysteresis loops obtained for Sb_2S_3-AAO samples with mean diameters of 200, 100 and 50 nm. The square-shaped phase hysteresis loops obtained for all of the Sb_2S_3-AAO samples exhibit a 180° domain reversal

(↑↓), which is a signature of the presence of ferroelectricity in the Sb_2S_3 nanowires.[37,39,40] The180° phase reversal of the polarisation during the voltage sweep is an indication of switchable ferroelectricity in Sb_2S_3 nanowires. The origin of ferroelectricity in Sb_2S_3 nanowires at room temperature can be explained by the polar C_{2v}^9 symmetry of the orthorhombic Sb_2S_3 crystal.[6,11] The polarisation results from small structural changes in the co-ordination sphere of Sb and S atoms within the two $(Sb_4S_6)_n$ chains along the *c*-axis (Figure 3.7), thus the associated change in polarisation will be confined to one direction in space along the polar axis of Sb_2S_3 nanowires.[11,13,42] The phase hysteresis of 200 nm Sb_2S_3 nanowires showed an asymmetry with reference to the phase, this may be caused by the surface charges at the back electrode and the nanowire interface.[43]

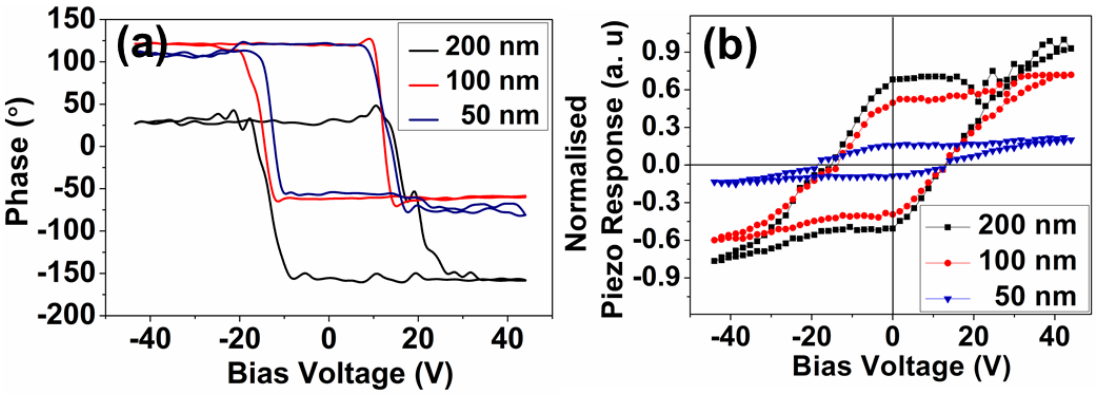

Figure 3.11. SS-PFM hysteresis loops acquired from an individual Sb_2S_3 nanowire inside AAO pores various diameters: (a) phase-voltage hysteresis and (b) piezo response-voltage hysteresis.

Sb_2S_3 nanowires also displayed piezoelectric behaviour. The normalised piezo-response hysteresis loop obtained for Sb_2S_3-AAO samples of various diameters is

shown in Figure 3.11(b). 200 and 100 nm Sb_2S_3-AAO samples showed well defined piezoelectric switching hysteresis, while 50 nm samples displayed very weak piezo switching. The depolarisation field on the 50 nm nanowire may be higher due to the higher surface area of the nanowire, which could hamper the ferroelectric polarisation.[37] It is also noted that the surface of polished 50 nm samples was found to be rougher than the 100 and 200 nm samples, which may have created significant perturbations on the tip across the surface. This roughness thus may have caused a decrease in the tip-surface contact quality, which in turn affects the PFM hysteresis loop acquisition.[31,40] A study by Zhang *et al.* on PZT-AAO samples highlighted the possible influence of nanowire-AAO wall interfaces on the PFM piezo-response signal.[44] The reason for the reduced piezoelectric coefficient and polarisation in the thinnest Sb_2S_3 nanowires is not fully conclusive and need further detailed study. The forward (+) and reverse (-) domain nucleation voltage or coercive bias (Figure 3.11(b)) of ~ ±20 V, can be attributed to the domain nucleation below the PFM tip at the Sb_2S_3-AAO surface.[40]

3.3.4.2 Quantification of the piezo and ferroelectric responses

The piezoelectric response of a material is expressed by its piezoelectric constants, d_{ij}, where i=1, 2, 3, j=1,..,6, which quantifies the volume change when the material is subject to an electric field.[21] The piezoelectric constant d_{33} represents the electromechanical response in the z-direction when an electric field is applied in the same direction and is typically calculated from SS-PFM amplitude signals.[31] A quantitative measure of the piezoresponse of the Sb_2S_3 nanowires synthesised was obtained by calculating piezoelectric coefficients from the SS-PFM piezo amplitude

hysteresis loops, as shown Figure 3.11(b). The measured piezoelectric coefficient, which is designated as $d_{33(eff)}$ ('effective' d_{33} coefficient) represents the electromechanical response from a Sb_2S_3 nanowire inside an AAO pore in the *z*-direction when an electric field is applied in the same direction.[31] The maximum piezoelectric coefficient [$d_{33(eff)}$] can be calculated using the equation, $d_{33} = A/ V_{ac}Q_f$; where A is the maximum amplitude, V_{ac} is the applied AC drive voltage and Q_f is the quality factor of the cantilever (obtained during SS-PFM hysteresis loop acquisition and dependent on the tip-sample surface interaction) that describes the energy losses in the measured system.[31] Typical Q_f values in air for PFM cantilevers range from 10 to 100.[45] The cantilever in contact with the surface has a resonance defined by the mechanical properties of the cantilever and the stiffness of the tip-sample contact. This resonance can have a high quality factor (Q_f) for typical PFM samples that effectively amplifies the piezo signal by a factor of ~Q_f near the resonance frequency of the tip. The gain in the signal from the Q_f -factor when operating near resonance improves the signal to noise ratio for the PFM amplitude and the phase. For samples with small piezo coefficients, this is potentially a very important effect and could mean the difference between only noise and a measurable signal.[45]

Table 3.1. The calculated maximum piezoelectric coefficient $d_{33(eff)}$ obtained for Sb_2S_3 nanowires with various diameter.

Sample Sb_2S_3-AAO	Maximum amplitude, pm	Voltage, V_{ac}	Quality factor, Q_f	Maximum $d_{33(eff)}$, pm V^{-1}
200 nm	496	3.3	75.2	2.0
100 nm	357	3.3	60.0	1.8
50 nm	150	3.3	56.5	0.8

The calculated maximum piezoelectric coefficient $d_{33(eff)}$ for the Sb_2S_3 nanowires with various diameters is given in Table 3.1. The 200 and 100 nm Sb_2S_3 nanowires showed $d_{33(eff)}$ values around 2 pm V^{-1}, while the piezo coefficient obtained for 50 nm nanowires was relatively low at around 0.8 pm V^{-1}. The low piezoresponse from 50 nm nanowires can be attributed to the presence of defects present in the nanowires as evident from TEM investigation. There is no report so far on quantification of piezoresponses from bulk Sb_2S_3 single crystals. The $d_{33(eff)}$ value obtained for Sb_2S_3 nanowires was very weak compared to other common piezoelectric nanowires, such as $(PbZr_{1-x}T_x)O_3$, ZnO and $BaTiO_3$, which are in the range of 10 to 100 pm V^{-1}, [46-48] due to the small structural changes which occur during the ferroelectric phase transition in Sb_2S_3.[11]

3.3.4.3 PFM domain switching experiments

Domain switching under the application of an external field is a signature characteristic of switchable ferroelectricity.[21,31,38] PFM is a powerful technique for probing the nucleation, growth and switching of ferroelectric domains in nanoscale ferroelectrics.[3,31,37] Figure 3.12 illustrates the switched ferroelectric domain images of Sb_2S_3-AAO under the application of an external bias, which provides conclusive evidence for the presence of switchable ferroelectricity in Sb_2S_3 nanowires. Figures 3.12(a) and 3.12(b) represents topography and PFM phase images of a Sb_2S_3-AAO sample before switching. Domain switching was observed in the Sb_2S_3 nanowires at an applied bias of -33 V was applied, as seen by the change in the colour contrast in the PFM phase image (Figure 3.12(c)). The application of an opposite bias of +33 V on the same area reversed the domain structure in the nanowires (Figure 3.12(d)). To confirm the effect of the applied bias on the domain switching characteristics, an

increased bias of ±44 V was applied to the nanowires (Figures 3.12(f) and 3.12(g)). The uniform colour contrast observed in the PFM phase image after applying a bias of -44 V (Figure 3.12(f)) indicates complete switching of the nanowire to a stable opposite polarisation state.

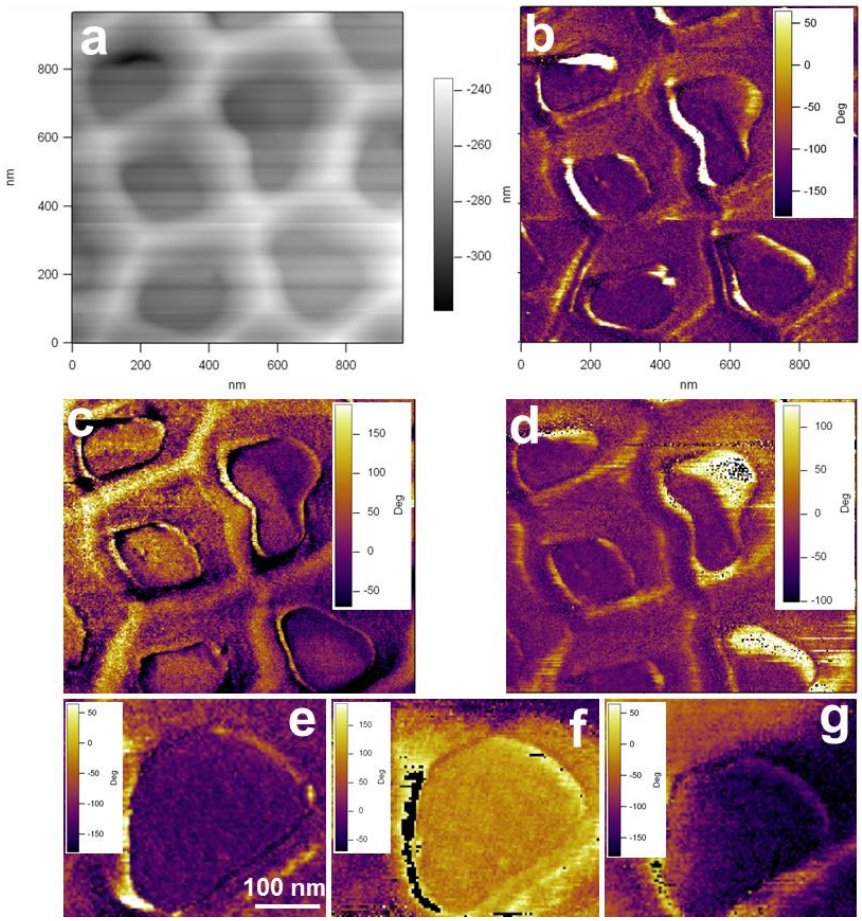

Figure 3.12. Ferroelectric domain switching in a selected area of a 200 nm Sb_2S_3-AAO sample: (a) topographic image, (b) PFM phase image before switching, (c) after switching, by applying –33 V, (d) after applying + 33 V, (e) PFM phase image of a selected Sb_2S_3 nanowire before ferroelectric domain switching, (f) after switching of the nanowire by applying –44 V, and (g) after applying + 44 V.

Piezoresponse microscopy can be readily used to investigate the kinetics of domain relaxation and depolarisation in a ferroelectric material.[49] The stability of the

polarisation state of a ferroelectric sample is of importance for applications such as ferroelectric memory. The process of switching back ferroelectric domains to their original state with time is called the polarisation loss.[49] Figure 3.13 illustrates the polarisation loss observed in a Sb_2S_3-AAO sample studied by PFM phase imaging. The Sb_2S_3-AAO sample was selectively switched by applying +33 V, as shown in image Figure 3.13. The Sb_2S_3 nanowires showed an almost full polarisation loss within in 16 minutes, which would be unfavourable for memory applications.

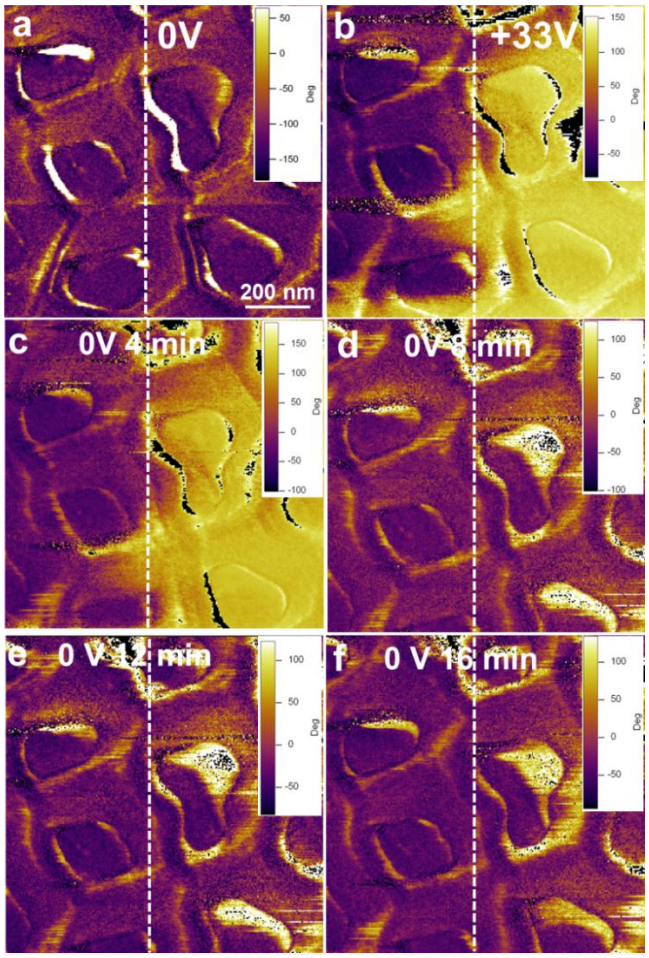

Figure 3.13. Ferroelectric domain polarization loss at various time intervals in 200 nm Sb_2S_3-AAO nanowire arrays: (a) at 0 V, (b) after poling with +33 V, (c, d, e and f) at 0 V after 4, 8, 12 and 16 min. respectively.

3.3.5 Bulk ferroelectric measurements on arrays of Sb_2S_3-AAO nanowires

The presence of ferroelectricity in arrays of Sb_2S_3-AAO nanowires (Gold/Sb_2S_3-AAO/Gold capacitor geometry) was further confirmed by polarisation-electric field (*P-E*) hysteresis loop measurement. This 'nanowire bulk' measurement allowed accurate determination of spontaneous polarisation (P_s) of Sb_2S_3 nanowires inside the AAO membrane. The well-defined *P-E* hysteresis loop obtained for the nanowires (Figure 3.14), irrespective of the diameter, is conclusive evidence of the presence of ferroelectricity in the Sb_2S_3 nanowires and further supports the data obtained from PFM analysis. The shape of the *P-E* loop showed incomplete saturation of the hysteresis, an indication of 'still growing' domains.[38] This type of unsaturation is usual in weak ferroelectric materials and much higher fields are typically required to switch the domain polarisation.[38] Sb_2S_3 nanowires with a mean diameter of 200 nm showed a maximum spontaneous polarisation (P_s) of ~1.6 μC cm^{-2} while nanowires with a mean diameter of 50 nm displayed a P_s value of ~1 μC cm^{-2}. 50 nm nanowires were showing a narrow hysteresis, which may be due to the increase in depolarisation field created on the surface that tends to destabilise the ferroelectric polarisation.[37] A material is said to be spontaneously polarised when the electric field (*E*) is zero but its polarisation (*P*) is a non-zero value.[50] Spontaneous polarisation is estimated by taking the intercept of the polarisation axis with the extrapolated linear segment of the polarisation reversal region (Figure 3.14).

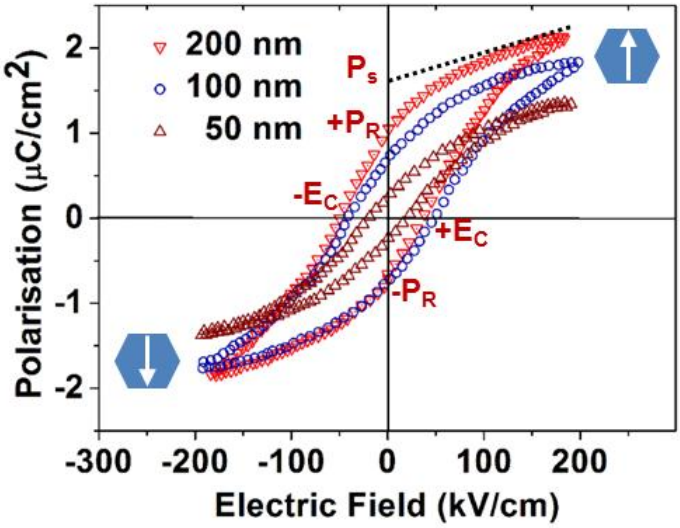

Figure 3.14. Polarisation-electric field (*P-E*) hysteresis loops for Sb_2S_3-AAO samples with various mean diameters.

The spontaneous polarisation observed in Sb_2S_3 nanowires was small (~ 1.6 μC cm^{-2}) compared to other common perovskite-based ferroelectric nanowires such as PZT nanowires (~ 30 μC cm^{-2}).[51] During polarisation switching, in perovskite ferroelectrics, displacement of atoms causes polarity changes in the whole lattice, which results in a massive polarisation, *i.e.* via a displacement mechanism.[21] In contrast, the polarisation reversal in bulk Sb_2S_3 is a result of an order-disorder transition in the $(Sb_4S_6)_n$ chains which creates only a small polar distortion of the lattice and results in a weak spontaneous polarisation.[10,11,13] The same reasoning can be applied to the weak piezoelectric behaviour of Sb_2S_3 nanowires. Sb_2S_3 nanowires, irrespective of their diameter, show a remnant polarisation ($\pm P_R$) and coercive field of switching ($\pm E_c$), obtained from the *P-E* loop (Figure 3.14), of approximately 1 μC cm^{-2} and ±50 kV cm^{-2} respectively. Remnant polarisation ($\pm P_R$) is the polarisation remaining in a ferroelectric material when the polarisation field is reduced to zero. The electric field applied antiparallel to the polarisation switches the polarisation

from the positive ($+P_R$) and negative remnant responses ($-P_R$) and the difference between these two remnant states is the remnant switchable response present in the material, *i.e.* $[(+P_R) - (-P_R)]$.[40,50] Coercive field ($\pm E_c$) is the electric field required to bring polarisation (P) back to zero.

Significantly the spontaneous polarisation observed in our Sb_2S_3 nanowires showed an enhancement compared to the bulk. At room temperature bulk Sb_2S_3 showed a spontaneous polarisation of ~ 0.9 μC cm^{-2}, which means the polarisation, is almost doubled in the nanowires.[6] A similar enhancement was observed in Rochelle salt single crystalline nanowires formed within the pores of AAO membranes[35], where the enhancement was attributed to the presence of multiple nanodomains with uniform orientation along the direction of the applied electric field. Morozovska *et al.*[19], in their study on ferroelectricity enhancement in confined nanorods, proposed that the ferroelectric property enhancement in nanowires and nanorods was due to the long-range interactions along the polar axis.[19,36] Also a uniform crystallographic orientation will enhance the uniform alignment of ferroelectric nanodomains.[35] In the Sb_2S_3 nanowires, the formation of 180° domains with polarisation directions pointing along +*z* and –*z* directions leads to a decrease in the depolarising field which enhances the spontaneous polarisation, especially noticeable in 1D ferroelectrics.[52] The single crystalline nature of the Sb_2S_3 nanowires (*c*- axis oriented) and their long range order inside AAO templates aligned the dipoles preferentially along the *c*-axis of nanowires, especially in 200 nm nanowires.

3.4 Conclusions

The bottom-up templating strategy, using AAO templates combined with a solventless approach, has proven to be a facile way to synthesise single crystalline arrays of Sb_2S_3 nanowires with controlled dimensions. Additionally, the use of AAO templates eliminates the agglomeration of Sb_2S_3 nanowires and hence allowing the ferroelectric functionality of individual nanowires to be probed by PFM techniques. PFM analysis showed that most of the Sb_2S_3 nanowires formed single ferroelectric domain (180°) structures due to the preferential alignment of dipoles along their polar axis; owing to the preferential growth of nanowires along the *c*-axis. Also, PFM switching studies demonstrated the reversible switching capabilities of individual and groups of Sb_2S_3 nanowires. The relative instability of ferroelectric domains in the Sb_2S_3 nanowires was revealed using time-varied PFM phase imaging studies. In summary, this work demonstrated the controlled synthesis of various diameter single crystalline Sb_2S_3 nanowires with switchable ferroelectric and piezoelectric properties.

3.5 References

(1) Scott, J. F.; Morrison, F. D.; Miyake, M.; Zubko, P. *Ferroelectrics* **2006**, *336*, 237.

(2) Gruverman, A.; Kholkin, A. *Rep. Prog. Phys.* **2006**, *69*, 2443.

(3) Han, H.; Kim, Y.; Alexe, M.; Hesse, D.; Lee, W. *Adv. Mater.* **2011**, *23*, 4599.

(4) Vilquin, B.; Gautier, B.; Brugere, A.; Moulet, J. S. *AIP Conference Proceedings* **2009**, *1173*, 129.

(5) Ibuki, S.; Yoshimatsu, S. *J. Phys. Soc. Jpn.* **1955**, *10*, 549.

(6) Semiconductors: Non-Tetrahedrally Bonded Elements and Binary Compounds I. In *Landolt-Börnstein - Group III Condensed Matter*; Madelung, O., Rössler, U., Schulz, M., Eds.; Springer-Verlag, 1998; Vol. III/17E-17F-41C.

(7) Han, Q.; Sun, S.; Sun, D.; Zhu, J.; Wang, X. *RSC Advances* **2011**, *1*, 1364.

(8) Lim, C.-S.; Im, S. H.; Rhee, J. H.; Lee, Y. H.; Kim, H.-J.; Maiti, N.; Kang, Y.; Chang, J. A.; Nazeeruddin, M. K.; Gratzel, M.; Seok, S. I. *J. Mater. Chem.* **2012**, *22*, 1107.

(9) Moon, S.-J.; Itzhaik, Y.; Yum, J.-H.; Zakeeruddin, S. M.; Hodes, G.; Grätzel, M. *The Journal of Physical Chemistry Letters* **2010**, *1*, 1524.

(10) Grigas, J. *Microwave dielectric spectroscopy of ferroelectrics and related materials* Gordon and Breach Publishers: Amsterdam B.V., 1996; Vol. 9.

(11) Grigas, J. *Ferroelectrics* **1978**, *20*, 173.

(12) Arun, P.; Vedeshwar, A. G. *J Mater Sci* **1996**, *31*, 6507.

(13) Grigas, J.; Talik, E.; Lazauskas, V. *Phase Transitions: A Multinational Journal* **2002**, *75*, 323.

(14) Bin Yang, R.; Bachmann, J.; Reiche, M.; Gerlach, J. W.; Gosele, U.; Nielsch, K. *Chem. Mater.* **2009**, *21*, 2586.

(15) Bin Yang, R.; Bachmann, J.; Pippel, E.; Berger, A.; Woltersdorf, J.; Gosele, U.; Nielsch, K. *Adv. Mater.* **2009**, *21*, 3170.

(16) Bao, H. F.; Cui, X. Q.; Li, C. M.; Song, Q. L.; Lu, Z. S.; Guo, J. *J Phys Chem C* **2007**, *111*, 17131.

(17) Scott, J. F. *Ferroelectrics* **2005**, *316*, 13.

(18) Morozovska, A. N.; Glinchuk, M. D.; Eliseev, E. A. *Phase Transitions* **2007**, *80*, 71.

(19) Morozovska, A. N.; Eliseev, E. A.; Glinchuk, M. D. *Phys Rev B* **2006**, *73*.

(20) Kim, J.; Yang, S. A.; Choi, Y. C.; Han, J. K.; Jeong, K. O.; Yun, Y. J.; Kim, D. J.; Yang, S. M.; Yoon, D.; Cheong, H.; Chang, K. S.; Noh, T. W.; Bu, S. D. *Nano Lett.* **2008**, *8*, 1813.

(21) Haertling, G. H. *J. Am. Ceram. Soc.* **1999**, *82*, 797.

(22) Mane, R. S.; Lokhande, C. D. *Mater. Chem. Phys.* **2000**, *65*, 1.

(23) Han, Q. F.; Chen, L.; Wang, M. J.; Yang, X. J.; Lu, L. D.; Wang, X. *Mater Sci Eng B-Adv* **2010**, *166*, 118.

(24) Routkevitch, D.; Tager, A. A.; Haruyama, J.; Almawlawi, D.; Moskovits, M.; Xu, J. M. *Ieee Transactions on Electron Devices* **1996**, *43*, 1646.

(25) Hernandez-Velez, M. *Thin Solid Films* **2006**, *495*, 51.

(26) Martin, C. R. *Science* **1994**, *266*, 1961.

(27) Goodey, A. P.; Eichfeld, S. M.; Lew, K.-K.; Redwing, J. M.; Mallouk, T. E. *J. Am. Chem. Soc.* **2007**, *129*, 12344.

(28) Evans, P. R.; Zhu, X.; Baxter, P.; McMillen, M.; McPhillips, J.; Morrison, F. D.; Scott, J. F.; Pollard, R. J.; Bowman, R. M.; Gregg, J. M. *Nano Lett.* **2007**, *7*, 1134.

(29) Khwaja, M. A.; Cardwell, T. J.; Magee, R. J. *Anal. Chim. Acta* **1973**, *64*, 9.

(30) Ma, J.; Duan, X.; Lian, J.; Kim, T.; Peng, P.; Liu, X.; Liu, Z.; Li, H.; Zheng, W. *Chemistry – A European Journal* **2010**, *16*, 13210.

(31) Balke, N.; Bdikin, I.; Kalinin, S. V.; Kholkin, A. L. *J. Am. Ceram. Soc.* **2009**, *92*, 1629.

(32) Gruverman, A.; Kalinin, S. V. Piezoresponse force microscopy and recent advances in nanoscale studies of ferroelectrics. In *Frontiers of Ferroelectricity*, 2007; pp 107.

(33) Elisabeth, S. *J. Phys. D: Appl. Phys.* **2011**, *44*, 464003.

(34) Wang, Z.; Hu, J.; Yu, M.-F. *Appl. Phys. Lett.* **2006**, *89*, 263119.

(35) Yadlovker, D.; Berger, S. *Phys Rev B* **2005**, *71*, 184112.

(36) Morozovska, A. N.; Eliseev, E. A.; Glinchuk, M. D. *Physica B: Condensed Matter* **2007**, *387*, 358.

(37) Kalinin, S. V.; et al. *Rep. Prog. Phys.* **2010**, *73*, 056502.

(38) Rabe, K. A.; Dawber, M.; Lichtensteiger, C.; Ahn, C. H.; Triscone, J. M. Modern physics of ferroelectrics: Essential background. In *Physics of Ferroelectrics: A Modern Perspective*; Rabe, K. M., Ahn, C. H., Triscone, J. M., Eds.; Springer-Verlag Berlin: Berlin, 2007; Vol. 105; pp 1.

(39) Jesse, S.; Baddorf, A. P.; Kalinin, S. V. *Appl. Phys. Lett.* **2006**, *88*, 062908.

(40) Jesse, S.; Lee, H. N.; Kalinin, S. V. *Rev. Sci. Instrum.* **2006**, *77*, 073702.

(41) Rodriguez, B. J.; Jesse, S.; Alexe, M.; Kalinin, S. V. *Adv. Mater.* **2008**, *20*, 109.

(42) Petzelt, J.; Grigas, J. *Ferroelectrics* **1973**, *5*, 59.

(43) Zhang, X. Y.; Zhao, X.; Lai, C. W.; Wang, J.; Tang, X. G.; Dai, J. Y. *Appl. Phys. Lett.* **2004**, *85*, 4190.

(44) Zhang, X. Y.; Zhao, X.; Lai, C. W.; Wang, J.; Tang, X. G.; Dai, J. Y. *Appl. Phys. Lett.* **2004**, *85*, 4190.

(45) *PFM application note 10, Asylum Research CA.*

(46) Fujisawa, H.; Kuri, R.; Shimizu, M.; Kotaka, Y.; Honda, K. *Appl. Phys. Express* **2009**, *2*.

(47) Wang, Z.; Suryavanshi, A. P.; Yu, M.-F. *Appl. Phys. Lett.* **2006**, *89*, 082903.

(48) Zhao, M.-H.; Wang, Z.-L.; Mao, S. X. *Nano Lett.* **2004**, *4*, 587.

(49) Kholkin, A.; Kalinin, S.; Roelofs, A.; Gruverman, A. Review of Ferroelectric Domain Imaging by Piezoresponse Force Microscopy. In *Scanning Probe Microscopy: Electrical and Electromechanical Phenomena at the Nanoscale*; Kalinin, S., Gruverman, A., Eds.; Springer New York, 2007; pp 173.

(50) Damjanovic, D. Chapter 4 - Hysteresis in Piezoelectric and Ferroelectric Materials. In *The Science of Hysteresis*; Academic Press: Oxford, 2006; pp 337.

(51) Xu, S.; Hansen, B. J.; Wang, Z. L. *Nat Commun* **2010**, *1*, 93.

(52) Naumov, I. I.; Bellaiche, L.; Fu, H. *Nature* **2004**, *432*, 737.

Chapter 4

Surface Roughness Assisted Growth of Vertically Oriented Ferroelectric SbSI Nanorods

4.1 Abstract

The catalyst-free synthesis and characterisation of arrays of *c*-axis oriented antimony sulphoiodide nanorods, formed on the surface of anodic aluminium oxide (AAO) substrates by vapour phase deposition, is reported in this Chapter. The surface roughness of the AAO substrate plays a decisive role in the orientation control of the SbSI nanorods produced. The as-grown SbSI nanorods were single crystalline and <001> oriented, as revealed from the X-ray diffraction and transmission electron microscopy analysis. Switching spectroscopy-piezoresponse force microscopy experiments demonstrated, for the first time, the presence of switchable ferroelectricity and piezoelectricity in individual SbSI nanorods. The ferroelectric switching in SbSI nanorods was found to occur via a 180° ferroelectric domain reversal due to the preferred orientation of the nanorods along the polar *c*-axis.

4.2 Background

4.2.1 Antimony sulphoiodide (SbSI)

Most of the research in nanoscale ferroelectrics and piezoelectrics has been focused primarily on oxide based perovskite materials,[1,2] with less focus given to non-oxide based systems. Many interesting ferroelectric and piezoelectric characteristics of non-oxide based systems have been reported in the literature in general,[3] among these antimony sulphoiodide (SbSI) draws attention due to its unusually high dielectric, piezoelectric and photoconducting properties.[4] SbSI is a semiconductor ferroelectric material which belongs to the V-VI-VII class of compounds and was widely studied during the 1960s and 1970s.[5-10] It has a narrow band gap (E_g) ~ 1.9-2.0 eV[11] and a maximum absorption wavelength at ~ 630 to 640 nm.[12] Since SbSI crystals are sensitive to wavelengths in the near infrared region, its ferroelectric polarisation can be tuned by illumination and hence SbSI is also termed a photoferroelectric.[13-16] The Curie temperature (T_C) of SbSI falls near room temperature, ~ 22 °C.[4] Above T_C (paraelectric state) it possesses D_{2h}^{16} (Pnam) crystal symmetry, while below T_C (ferroelectric state) it has C_{2v}^{9} ($Pna2_1$) symmetry.[17] SbSI shows highly anisotropic behaviour in many of its functional properties, due to its crystal structure[18] with polar double chains of $[(SbSI)_\infty]_2$ which run parallel to the polar *c*-axis.[19] This anisotropy accounts for its superior functional characteristics, such as a high peak pyroelectric coefficient (6×10^{-2} C m^{-2} K^{-1}),[20] dielectric constant (~50,000),[4] refractive index (~4.5),[21] and piezoelectric coefficient (2000 pC N^{-1}),[10] along the polar axis in single crystalline form.[19] These versatile functional properties of SbSI could lead to its use in many applications such as ferroelectric memory,[22] thermal imaging,[23] non-linear optics,[24,25] and mechanical actuation[26].

4.2.2 Vertically aligned arrays of SbSI nanowires

Although promising for many potential uses,[22-26] the difficulty in obtaining vertically aligned phase pure SbSI single crystals has put severe constraints on its real applicability.[23] The International Technology Roadmap for Semiconductors (ITRS) has identified the need for new nanostructured ferroelectric materials with significantly improved properties to meet future technology requirements.[27] As all of the interesting functional properties of SbSI are maximised along the *c*-axis,[4,10,20,21] it would be ideal to make vertically *c*-axis oriented SbSI nanostructures to exploit these superior properties. Vapour deposition[28-32] and pulsed laser deposition[23,33] have been the most widely used methods for making SbSI crystals and thin films. Many of these methods[8,23] have been successful in making *c*-axis oriented thin films, but no attempts have been made so far to synthesise vertically-aligned SbSI nanostructures. SbSI nanorods and nanowires have been synthesised by hydrothermal[34,35] ball milling,[36] and sonochemical[37] routes. Most of the methods of preparing SbSI reported to date have resulted in randomly-oriented, large-grained, discontinuous films due to the large energy barrier for nucleation of SbSI on the substrates. The surface roughness of the substrate plays a crucial role in controlling the energy barrier for nucleation and the orientation of the nanostructures, especially nanowires and nanorods. Recently, vertically aligned arrays of ZnO nanorods were synthesised on chemically etched sapphire substrates by a catalyst-free vapour-solid (VS) growth.[38,39] The vertical alignment of ZnO was caused by the assistance of irregularities, or roughness, present on the surface of the sapphire substrate. The surface roughness of a substrate can act as nucleation centres which reduce the nucleation barrier, improving oriented growth.[38,39] Based on this hypothesis, the

inherent surface roughness of anodic aluminium oxide/titanium/silicon (AAO/Ti/Si) substrates was utilised in this study to assist the growth of vertically aligned SbSI nanorods by vapour phase deposition. In addition, surface roughened platinised silicon (Pt/Si) substrates were also used for the present study. The nanoscale piezoelectric and ferroelectric characteristics of SbSI nanorods were studied using piezoresponse force microscopy (PFM), allowing the ferroelectric and piezoelectric functionality of individual nanostructures to be characterised on an individual basis.

In this work, arrays of SbSI nanorods were synthesised on AAO/Ti/Si and surface roughened Pt/Si substrates by vapour-phase deposition of a mixture of Sb_2S_3 and SbI_3 powders. A control experiment was conducted with a Si (001) substrate under similar conditions.

4.3 Results and Discussion

4.3.1 Growth of SbSI nanorods on AAO/Ti/Si substrates

The change in morphology of the synthesised SbSI nanostructures as a function of temperature was examined by SEM and the images are shown in Figure 4.1. The surface morphology of a bare AAO surface on a Ti/Si substrate (Figure 4.1(a)) shows pores with diameters ranging between 20 to 50 nm, including grain boundaries. These pores and grain boundaries give the AAO its rough surface. SbSI forms by a gaseous phase reaction between Sb_2S_3 and SbI_3 at a source temperature of 400 °C to form $(SbI_3)_x(Sb_2S_3)_{1-x}$,[29,40] which is then transported across a temperature gradient onto an AAO/Ti/Si substrate. The onset of nucleation of SbSI starts near ~160 °C, under conditions close to the critical saturation for the condensation of $(SbI_3)_x(Sb_2S_3)_{1-x}$.[29,40] As shown in Figure 4.1(b), SbSI starts nucleating at a substrate

temperature of 170 °C, in the form of tiny islands of $(SbI_3)_x(Sb_2S_3)_{1-x}$ condensate,[29,40] with a mean lateral size of ~ 200 to 300 nm. As the substrate temperature is increased to 250 °C, vertically oriented SbSI nanorods, with a mean length of ~ 3 μm and diameter range between 150 to 300 nm, formed on the surface of the AAO/Ti/Si substrate (Figure 4.1(c)). The as synthesised arrays of SbSI nanorod films displayed a characteristic wine red colour. Upon increasing the substrate temperature to 275 °C, the SbSI nanorods tended to coalesce to form vertically oriented SbSI nanorod clusters with a mean length of ~ 3 μm and diameter of 600 nm (Figure 4.1(d)). The coverage and density of the vertical SbSI crystallites on the AAO/Ti/Si substrates increased as the substrate temperature is increased from 250 to 275 °C; since a higher temperature could increase the migration rate of SbSI species, promoting a high uniform distribution of SbSI on the surface.[41] Figure 4.1(e) shows the side-view of SbSI nanorods, clearly indicating that nucleation starts from the AAO surface. In this work, the optimum temperature to obtain phase pure SbSI was found to be 250 °C. Deposition temperatures lower and higher than 250 °C resulted in SbI_3-rich SbSI and non-stoichiometric SbSI respectively. Since no droplet of catalyst or any particle was observed on the tips of the SbSI nanorods (see inset Figure 4.1(c)), the growth process of SbSI nanorods occurred via a self-catalysed vapour-solid growth mechanism.

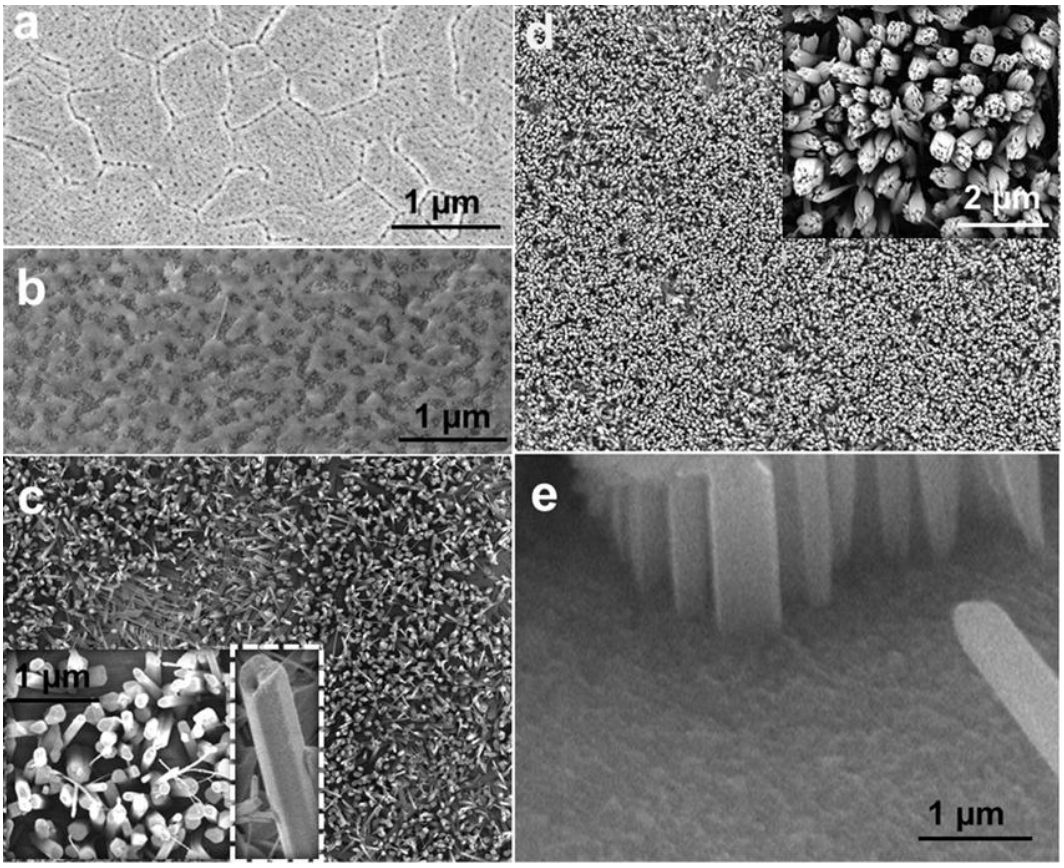

Figure 4.1. SEM images showing (a) a plan-view image of an AAO/Ti/Si substrate, (b) islands of $(SbI_3)_x(Sb_2S_3)_{1-x}$ formed at 170 °C on a AAO/Ti/Si substrate, (c) vertical SbSI nanorods formed at 250 °C, (d) vertical SbSI nanorod clusters formed at 275 °C and (e) side-view of SbSI nanorods formed on an AAO/Ti/Si substrate at 250 °C.

The phase purity of the as-synthesised SbSI nanorods was confirmed using XRD analysis. The XRD pattern of SbSI nanorods grown from an AAO/Ti/Si substrate, at a reaction temperature of 250 °C, is shown in Figure 4.2(a) and can be indexed to orthorhombic SbSI (space group, $Pna2_1$; PDF no. 88-2407), displaying a high intensity (002) reflection at 2θ = 44.3°; an indication of the predominant *c*-axis oriented growth of the SbSI nanorods formed.

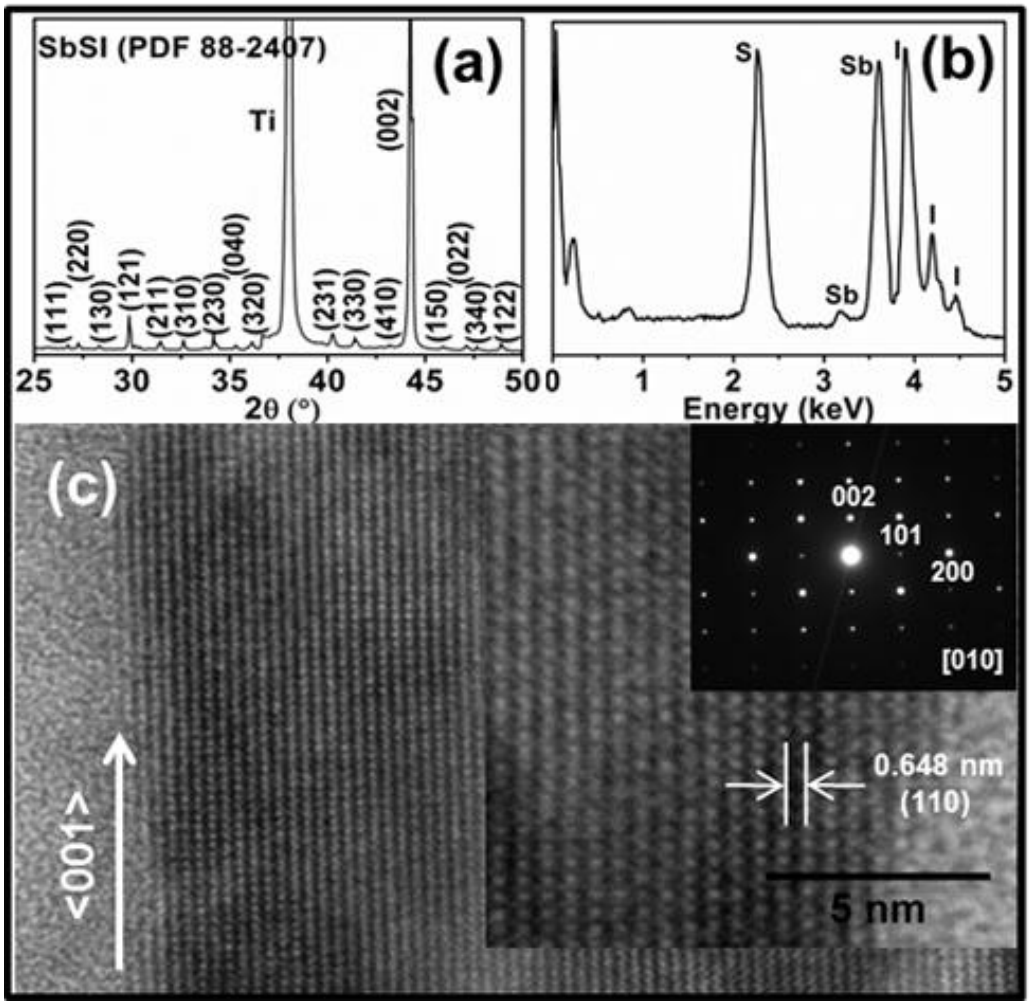

Figure 4.2. (a) XRD pattern of SbSI nanorods formed at 250 °C on an AAO/Ti/Si substrate, indexed to orthorhombic SbSI (PDF No: 88-2407), (b) EDX spectrum of an individual SbSI nanorod and (c) TEM image of a SbSI nanorod showing preferential <001> oriented growth (inset showing high resolution images of lattice fringes and SAED pattern obtained along [010] zone axis); the labelled lattice fringe spacing of 0.648 nm corresponds to the (110) lattice plane of SbSI.

TEM analysis of the SbSI nanorods (Figure 4.2(c)) revealed their single crystalline nature, with a predominant growth direction along the <001> axis, confirming that the *c*-axis is normal to the substrate plane. The measured lattice fringe spacing of

0.648 nm corresponds to the (110) plane of a SbSI nanorod. Selected area electron diffraction (SAED) was used to further confirm the *c*-axis orientation of the SbSI nanorod. The electron diffraction pattern, obtained in the [010] zone axis, (inset in Figure 4.2(c)) further reiterates the single crystalline nature and dominant <001> growth of the nanorods. The lattice fringe spacing and angles between planes in the SAED pattern can be indexed to orthorhombic SbSI. The composition of individual SbSI nanorods grown at 250 °C was determined by EDX analysis (Figure 4.2(b)). Quantitative EDX analysis showed that the as synthesised material composed of 33.9 % Sb, 34.0% S and 32.2% I; with an atomic ratio ($SbSI_{0.95}$) close to the expected stoichiometry (1:1:1).

The XRD pattern of the as-synthesised arrays of SbSI nanorods at 275 °C is shown in Figure 4.3(a). All diffraction peaks in the XRD pattern can be indexed to orthorhombic SbSI (PDF No. 88-2407). The high intensity reflection obtained from the (002) plane indicates the preferential c-axis oriented growth of the SbSI nanorods formed, similar to those synthesised at 250 °C. Quantitative EDX analysis (Figure 4.3(b)) showed that the nanorods formed at 275 °C was slightly non-stoichiometric, with a composition of $SbS_{0.9}I_{0.89}$, due to partial decomposition of SbSI.[28]

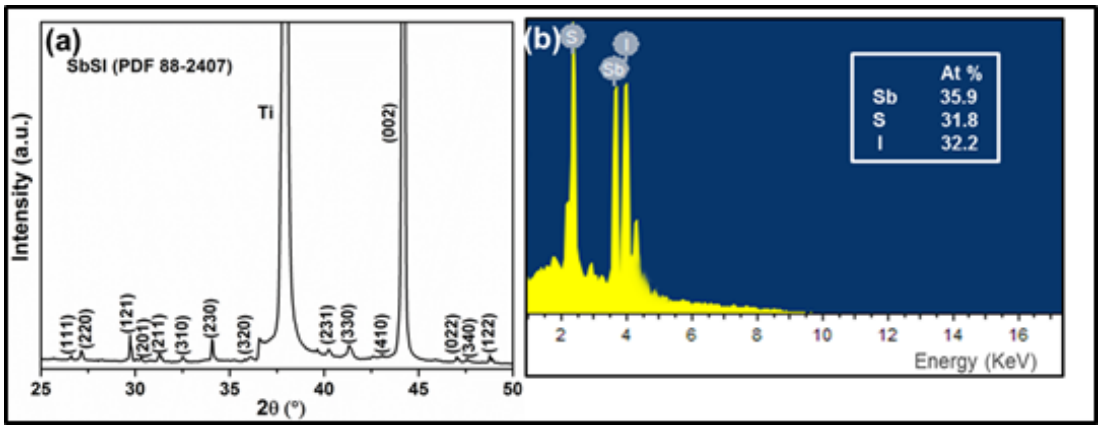

Figure 4.3. (a) XRD pattern of SbSI nanorods formed at 275 °C on AAO/Ti/Si substrate, indexed to the orthorhombic SbSI (JCPDS file No: 88-2407) and (b) EDX spectra of SbSI formed at 275 °C on AAO/Ti/Si substrate.

To study the influence of surface roughness on the alignment of SbSI nanorods, a control experiment was carried out using a Si (001) substrate (Figure 4.4(a)), under similar deposition conditions to those used with the AAO/Ti/Si substrates. Figure 4.4(b) shows an SEM image of SbSI formed on a Si substrate at a deposition temperature of 250 °C. Randomly oriented one dimensional (1D) SbSI crystallites, with lengths between ~ 5 to 7 μm and width between ~ 600 to 700 nm, were observed on the Si substrate, highlighting that the substrate surface plays a crucial role in orienting the SbSI nanostructures. SbSI crystallites formed on smooth Si substrates prefer to align parallel to the substrate plane (Figures 4.4(b) and 4.4(c)), compared to the perpendicular alignment observed with the rough AAO/Ti/Si substrates (Figure 4.1(c) and 4.1(d)). However, SbSI crystals deposited on Si and AAO/Ti/Si substrates had a similar composition and 1D morphology but differed in their alignment. The XRD pattern (Figure 4(d)) obtained for the deposited films on a Si substrate can be indexed to orthorhombic indexed to orthorhombic SbSI (PDF no:

74-2245), with a distinct peak at 2θ = 32.8°, corresponding to the (310) reflection plane.

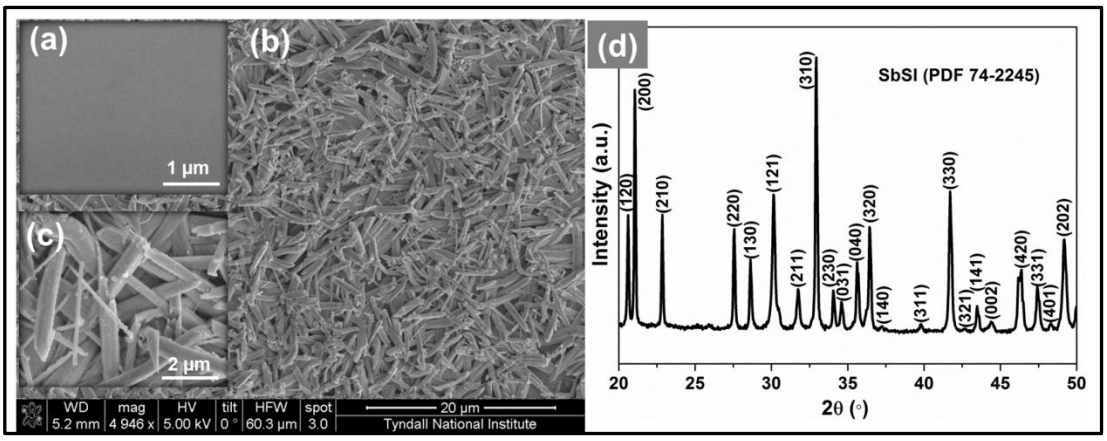

Figure 4.4. Plan-view SEM images of: (a) a bare Si (001) substrate, (b) SbSI nanorods formed on a Si substrate at a temperature of 250 °C, (c) zoomed-in image of SbSI crystallites and (d) XRD pattern of crystallites formed on a Si substrate, indexed to orthorhombic SbSI (PDF No: 74-2245).

The difference in the alignment of SbSI crystallites formed on AAO/Ti/Si compared to Si substrates can be explained by taking into account the surface roughness of these substrates. The pores and grain boundaries present on the surface of the AAO act as nucleation centres for the growth of SbSI. The rough surface of the AAO provides enough nucleation centres for the vertical growth of the SbSI compared to the smooth Si substrate, due to the lower critical energy required for nuclei formation on a rough substrate.[28,42] AFM surface roughness analysis showed that the as-synthesised AAO surface on Ti/Si substrates had a root mean square surface roughness of 9.03 ± 0.50 nm compared to 0.81 ± 0.02 nm for Si substrates. In comparison with the smooth Si substrate, an AAO/Ti/Si substrate provides more binding sites for the vertical growth of SbSI, accounting for the initial formation of

islands of $(SbI_3)_x(Sb_2S_3)_{1-x}$ (Figure 4.1(b)),[29,40] with no such deposition observed on Si substrates at the same temperature. These islands of $(SbI_3)_x(Sb_2S_3)_{1-x}$ act as nucleation centres for the vertical growth of SbSI nanorods. Once the nucleation occurs, the continued supply of incoming SbSI vapours result in 1D growth.[43] As seen in Figure 4.1(e), SbSI nanorods were nucleated and grown directly on the upper surface of the AAO template. Similar reasoning was applied for the formation of vertically aligned ZnO nanorods on chemically etched sapphire substrates,[38,39] SiC/AlSiC core-shell nanowires on AAO[44] membranes and V_2O_5 nanowires on chemically etched Si (001) substrates[43]. Due to the amorphous nature of AAO, the possibility of an epitaxial growth of SbSI can be excluded.

Furthermore, to compare the preferential orientation of the SbSI nanorods deposited on AAO/Ti/Si and Si substrates two XRD peaks of SbSI, (330) and (002), was studied. These peaks were chosen since the normal direction to the (002) plane corresponds to the *c*-axis and is parallel to the (330) plane, which is suitable to determine the vertical alignment of SbSI.[45] Figure 4.5 shows a comparison of the change in intensities of the (330) and (002) XRD peaks obtained for SbSI deposited, at 250 °C, on Si and AAO/Ti/Si substrates. The (330) and (002) diffraction peaks of SbSI appear at 41.6° and 44.3° (2θ) respectively. The peak intensity from the (002) diffraction plane of the SbSI crystals formed on a Si substrate (Figure 4.5(a)) was very weak compared to that from the nanorods formed on an AAO/Ti/Si substrate (Figure 4.5(b)). The high intensity (330) diffraction peak and low intensity (002) peak highlights that the *c*-axis of the SbSI crystallites grown on Si substrates are aligned parallel to the substrate plane. In contrast, XRD analysis of SbSI nanorods deposited on AAO/Ti/Si substrates showed intense (002) and weak (310) reflections

respectively, due to preferential vertical alignment of the SbSI nanorods along their *c*-axis. The appearance of a shoulder peak on the (002) reflection can be attributed to the tilted orientation of the nanowires with reference to the *c*-axis, which expose the other surface planes such as [100] or [110].

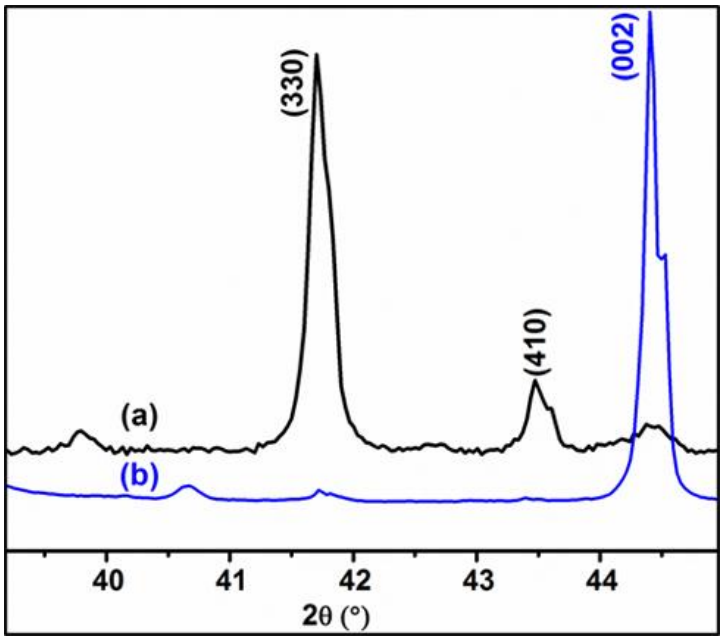

Figure 4.5. XRD patterns showing the influence of substrate on the degree of *c*-axis orientation of SbSI crystallites: (a) SbSI crystallites deposited on a Si substrate at 250 °C and (b) SbSI nanorods formed on AAO/Ti/Si substrate at 250 °C.

The 1D growth of the nanorods is attributed to the inherently fast growth of the SbSI crystal along their *c*-axis compared to their *a*-*b* planes.[19] This can be explained by taking into account the typical crystal structure of SbSI (Figure 4.6). The unit cell of SbSI contains double chains of $[(SbSI)_\infty]_2$ linked along the *z*-direction by a twofold screw axis (the orthorhombic structure of SbSI ($Pna2_1$) possess a 2_1 screw axis along the *z*-direction).[31,46] These chains act as 1D motifs along the [001] direction. In SbSI, the (001) planes have the highest surface energy and thus have the fastest

growth velocity.[31] Hence the growth of SbSI preferentially take place along the [001] direction, without the formation of 2D nuclei, giving it a 1D morphology.[31]

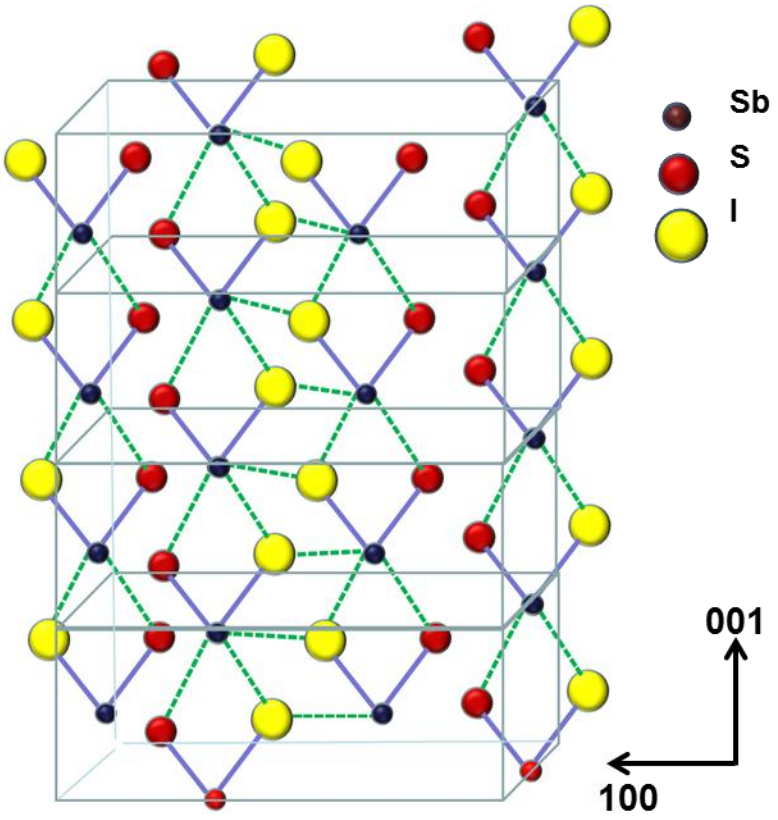

Figure 4.6. Crystal structure of SbSI viewed along the [010] direction.[46] The structure consists of double chains of $[(SbSI)_\infty]_2$ running along the *z*-direction. The Sb-S-I covalent bonds are indicated by solid lines and the weak van der Waals bonds between the chains by dashed lines.

One of the most influential factors determining the morphology of the SbSI crystals deposited on a given substrate, is the relative surface energies of various growth facets at the deposition conditions employed.[47] The inset in Figure 4.1(c) indicates that the SbSI nanorods are faceted. The reason for the faceting of the nanorods can be attributed to the polar nature of the SbSI crystals. Polar surfaces are generally

stabilised by surface reconstruction or faceting, by which they can reduce their surface energies.[47] During SbSI formation, after an initial period of nucleation, SbSI tends to form 1D structures because nanorod formation maximises the areas of the {110}, {010} and {100} facets, which have a lower surface energy compared to the high energy {002} facets.[30,48]

The nanoscale piezoelectric and ferroelectric properties of SbSI nanorods grown at 250 °C on AAO/Ti/Si substrates were studied, for the first time, using piezoresponse force microscopy (PFM) in contact mode. Compared to bulk techniques, PFM has the advantage of being able to visualise the ferroelectric domain dynamics, polarisation switching and quantification of piezoelectric responses of individual nanostructures.[49-52] The PFM ferroelectric and piezoelectric response obtained from a cluster of SbSI nanorods, 2.0 × 2.0 μm^2, dispersed on a conducting platinum substrate is shown in Figure 4.6. The PFM topography, piezoresponse amplitude and ferroelectric domain phase images obtained for SbSI nanorods are shown in Figures 4.7(a), 4.7(b) and 4.7(c) respectively. The piezoresponse can be clearly seen from the bright and dark amplitude contrast of the nanorods shown in Figure 4.7(b). The presence of the bright white contrast is evidence of piezoresponse in SbSI nanorods, due to an out-of-plane displacement along the polar *c*-axis. The PFM phase image (Figure 4.7(c)) of the SbSI nanorods clearly shows the presence of ferroelectric domains present in the material. Different orientations of the polar axis of adjacent domains in SbSI nanorods lead to a multi-domain contrast. This multi-domain structure is formed as a result of the differing level of polarity present in individual ferroelectric domains.[49]

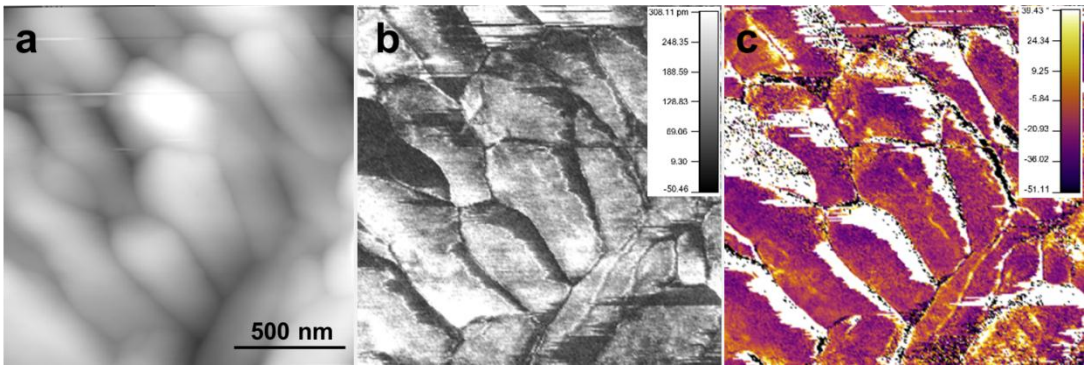

Figure 4.7. PFM images of SbSI nanorods dispersed on a conducting platinum substrate, showing: (a) height, (b) amplitude and (c) phase profiles SbSI nanorods grown at 250 °C on an AAO/Ti/Si substrate.

The primary feature of a ferroelectric material is the reversal of spontaneous polarisation under the application of an applied electric field. PFM has become a standard technique to analyse the local ferroelectric/piezoelectric switching properties of nanoscale materials.[49-51] An advanced version of PFM called switching spectroscopy PFM (SS-PFM) allows the acquisition of ferroelectric and piezoelectric switching hysteresis loops from a point on a nanostructure. In this study, hysteresis loops were obtained by positioning the conducting PFM tip on top of a SbSI nanorod and applying an AC voltage of 3.3 V, plus a DC bias of ±44 V, simultaneously across the nanorod and the back electrode. Figures 4.8(a) and 4.8(b) shows the phase and piezoresponse switching hysteresis obtained from a single SbSI nanorod, by positioning the tip in the centre of the top edge of the nanorod (Figure 4.8(a), red dot in the inset image). Positioning the tip on the (002) plane of the SbSI nanorod allowed the measurement of the piezoresponse along the polar *c*-axis. The square shape phase-voltage hysteresis (Figure 4.8(a)) curve obtained gives strong evidence for the presence of switchable ferroelectricity in SbSI nanorods. The 180° phase

difference observed during switching (Figure 4.8(a)) can be attributed to the presence of 180° ferroelectric polarisation present along the *c*-axis in the SbSI nanorod. Due to the <001> orientation of the SbSI nanorods, the polarisation changes occur mostly along the *c*-axis of the nanorods and thus results in the formation of two oppositely oriented (180°) ferroelectric domains along the polar axis. Similar results were reported in Chapter 3 for <001> oriented Sb_2S_3 nanowires.[53] Figure 4.8(b) depicts the normalised piezoresponse hysteresis response obtained for a SbSI nanorod, from the same location as that of the phase hysteresis. The inset image in Figure 4.8(b) shows the classical ferroelectric loop acquired from the SbSI nanorod, which is a signature of the presence of switchable piezoelectric response in the material.[50] The asymmetric nature of the hysteresis loop could be due to the clamping effect between the domains as well as due to the change in field distribution.[54]

The average effective piezoelectric coefficient d_{33}(eff) for the SbSI nanorods, calculated using equation[49,51], $d_{33} = A/V_{ac}Q_f$, where A is the maximum amplitude, V_{ac} is the applied AC voltage (3.3 V) and Q_f is the quality factor (obtained during the PFM measurement and depends solely on the tip-sample surface interaction), was found to be ~ 12 pm V^{-1}.[10] The difficulty related to positioning the PFM tip at a specific location on top of a SbSI nanorod surface, due to tip shift, put constraints on quantifying the piezoelectric response and limited my study to a qualitative view point. Figure 4.8(c) illustrates the changes observed in domains during ferroelectric switching of a single SbSI nanorod when a DC bias of ±44 V was applied. The applied bias induced a reversal of the ferroelectric domain structure and provides clear evidence for the presence of switchable ferroelectricity in the SbSI nanorods.

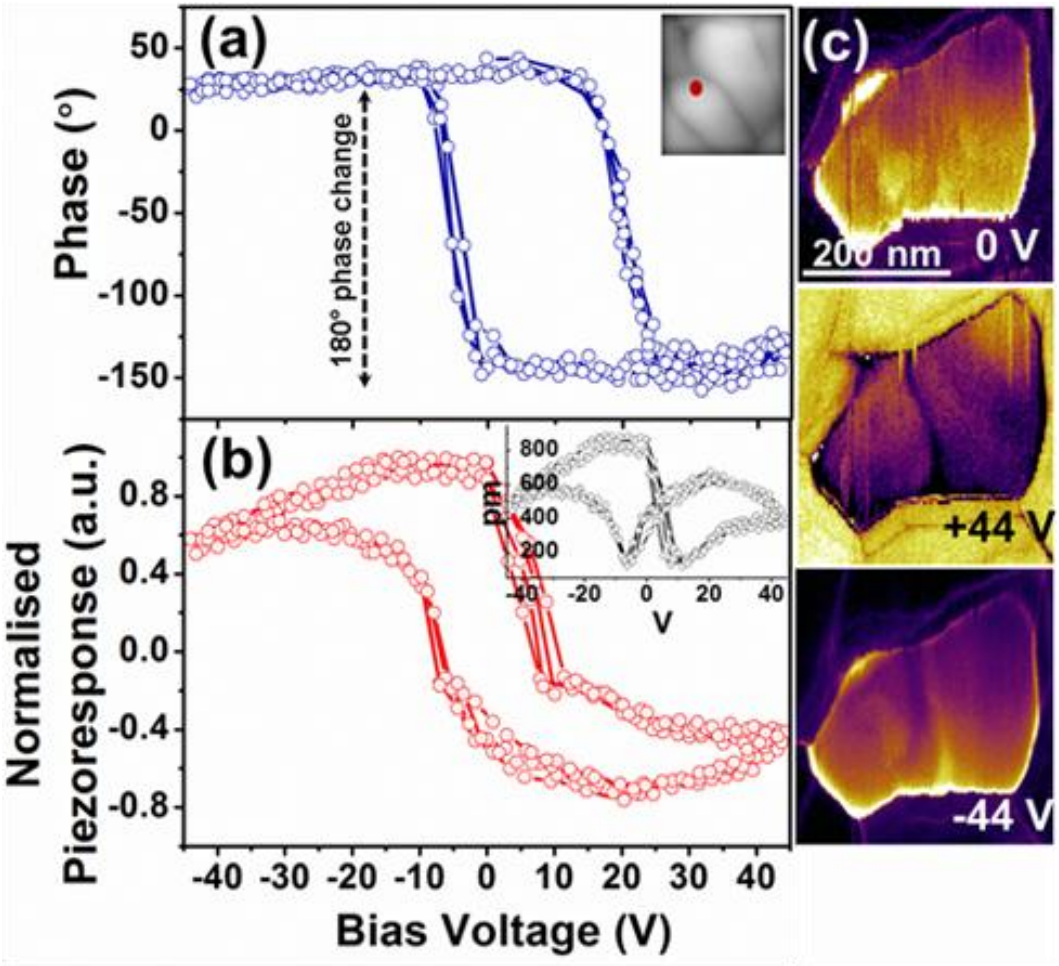

Figure 4.8. (a) SS-PFM ferroelectric phase-switching hysteresis, (the red dot in the inset image shows the location of the tip on the SbSI nanorod during the hysteresis loop acquisition), (b) normalised piezo-switching hysteresis (inset shows the actual butterfly shaped piezoresponse hysteresis loop), loops acquired from an individual SbSI nanorod and (c) SS-PFM ferroelectric phase images showing ferroelectric domain switching of a selected SbSI nanorod before and after domain switching, by applying a bias voltage of ±44V.

The presence of ferroelectricity in SbSI can be attributed to its orthorhombic structure with the polar space group $Pna2_1$, at room temperature. SbSI has a phase

transition or T_C of ~ 22 °C at which it undergoes a displacive ferroelectric phase transition from the ferroelectric $Pna2_1$ phase to the paraelectric Pnam phase.[4,18] The ferroelectric and piezoelectric switching, under the application of an applied bias in SbSI is associated with the alternating arrangement of polar double chains $[(SbSI)_\infty]_2$ parallel to the [001] axis.[18] The asymmetric arrangement of these double chains creates disorder of the Sb atoms and polarity in the SbSI crystal, which in turn results in unidirectional polarisation along the polar *c*-axis due to <001> orientation of the SbSI nanorods, accounting for their ferroelectric and piezoelectric behaviour.

4.3.2 Growth of arrays of SbSI nanowires on Pt/Si substrates

In addition to orienting SbSI nanostructures, for many applications it is desirable to integrate these nanostructures directly onto conducting substrates[33,55,22] For instance, Surthi *et al.* deposited SbSI on $Pt/Ti/SiO_2/Si$ [33] and $La_{0.67}Ca_{0.33}MnO_3$ (LCMO)/$NdGaO_3$ [22] substrates, where the Pt and LCMO layer acted as a bottom electrode respectively for electrical measurements. Some of the studies using conducting substrates for the growth of SbSI were successful in growing good quality *c*-axis oriented thin films for electrical measurements. Since most of the functional properties of SbSI are superior along its *c*-axis, the vertical alignment of SbSI 1D structures on conducting substrates may be advantageous for potential applications such as energy harvesting. As evident from the previous study with AAO/Ti/Si substrates, the surface state of the substrate has a great influence in aligning SbSI crystals. In this section of Chapter 4, the use of surface roughened conducting Pt/Ti/Si substrates for growing vertically oriented arrays of SbSI nanowires is discussed. Surface roughness on these substrates was achieved using

ultrasonication. A control experiment was carried out under similar condition using smooth Pt/Ti/Si substrates to prove the influence of surface roughness of the substrate on the alignment of nanowires formed.

The morphologies of SbSI formed on rough and smooth Pt/Ti/Si substrates are shown in Figure 4.9. The SEM images (Figure 4.9(a), (b) and (c)) show that a highly dense array of vertically aligned SbSI nanowires formed on a rough Pt/Ti/Si substrate. These arrays consist of uniform high aspect ratio (~ 140) nanowires with mean diameters ~ 50 nm and lengths up to 7 μm, having alignment angles approximately ±20° relative to the substrate normal. The cross-sectional SEM image (Figure 4.9(c)) revealed that SbSI nanowires grow directly from the substrate. While SbSI formed on smooth Pt/Ti/Si substrates showed (Figure 4.9(d) and (e)) thick film morphology, with randomly oriented 1D crystallites. This observation clearly illustrates the influence of the surface state of the substrate in aligning the SbSI and agrees with the previous results obtained for SbSI deposited on AAO/Ti/Si substrates. The inset in Figure 4.9(c) shows that the tips of the nanowires contain no droplets, which confirms that the growth of SbSI nanowires on rough Pt/Ti/Si substrates occurred via a catalyst-free vapour-solid growth mechanism.

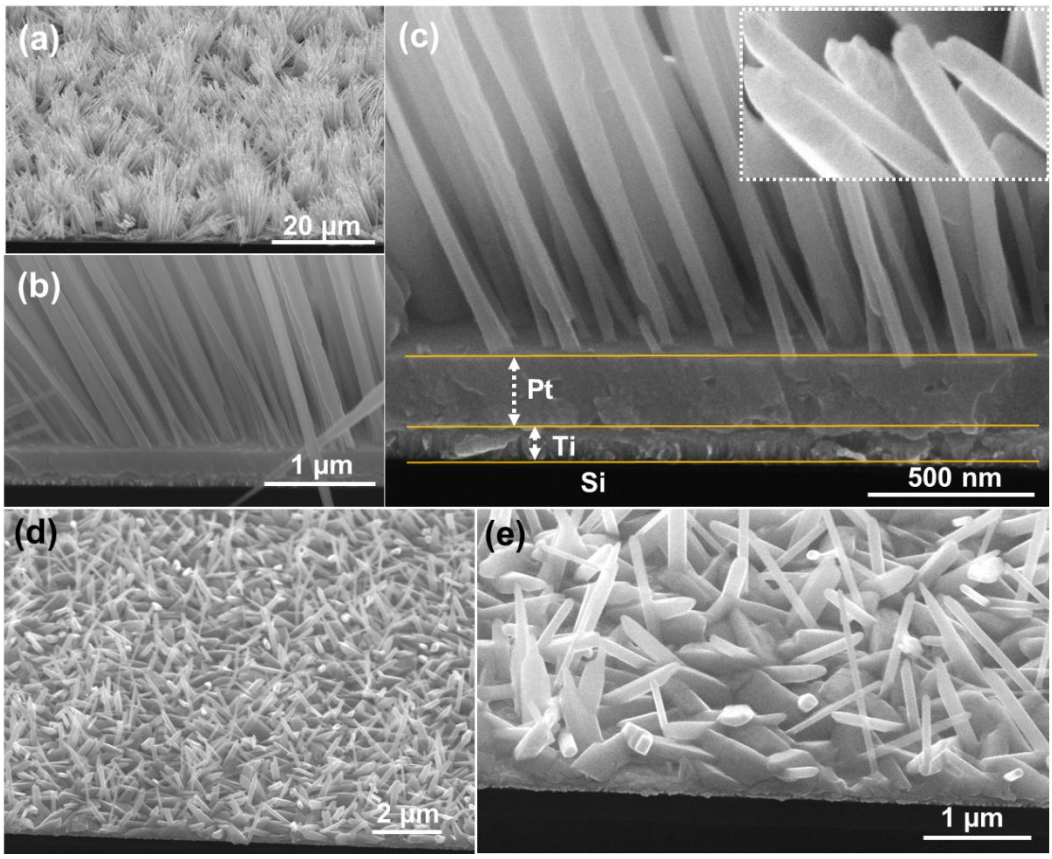

Figure 4.9. (a) Plan-view SEM image of arrays of SbSI nanowires deposited on a surface roughened Pt/Ti/Si substrate, (b) cross-sectional SEM image of the arrays, and (c) zoomed-in SEM image of a sample cross-section (inset shows the tip of the nanowires). (d) and (e) SEM images of randomly oriented SbSI crystallites deposited on a smooth Pt/Ti/Si substrate.

The XRD pattern (Figure 4.10(a)) of as-synthesised arrays of SbSI nanowires on rough Pt/Ti/Si substrates showed a prominent diffraction peak at 44.2° (2θ), which can be indexed to the (002) reflection of orthorhombic SbSI (PDF No: 88-2407). This data indicates that the SbSI nanowires have a preferred *c*-axis orientation. A high resolution TEM image (Figure 4.10(b)) of an isolated SbSI nanowire showed resolved lattice fringes without defects or dislocations, confirmed the single crystalline nature of the nanowires with a preferred growth along the <001>

direction. The mean lattice fringe spacing 0.51 nm corresponds to the d_{020} plane lattice spacing of orthorhombic SbSI (PDF No: 88-2407). The SAED pattern obtained from a SbSI nanowire along the [100] zone axis reiterates the preferential *c*-axis oriented growth of the nanowires. To determine the elemental composition of the nanowires formed, EDX analysis was performed on isolated SbSI nanowires (Figure 4.10(c)). Quantitative EDX analysis showed that the atomic ratio of Sb:S:I is 0.98:1:0.96, giving nanowires a possible composition of SbSI.

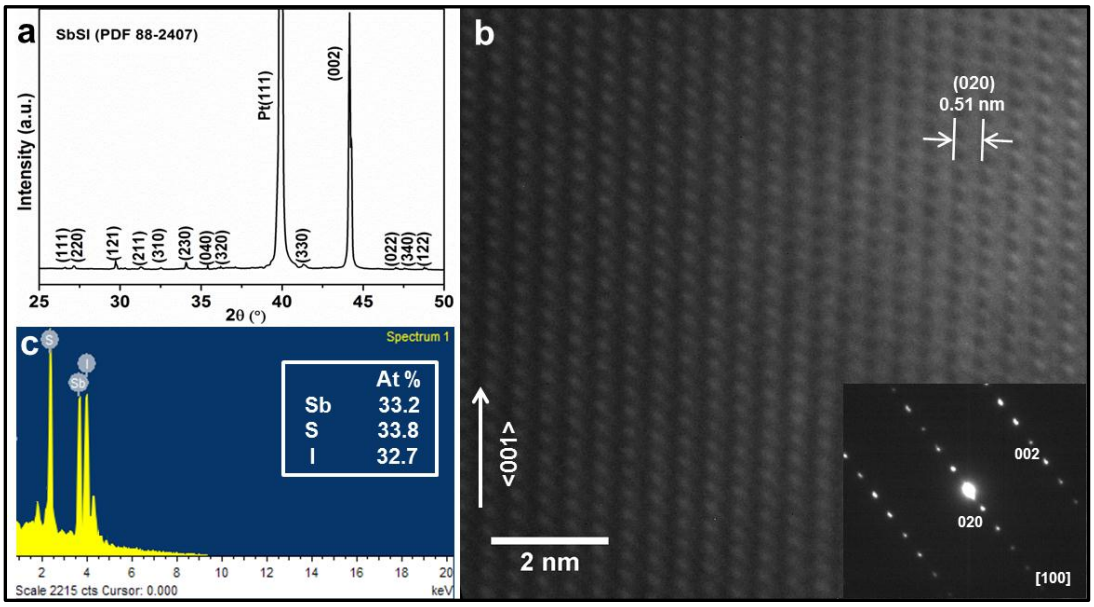

Figure 4.10. (a) XRD pattern of SbSI nanowires formed at 250 °C on a surface roughened Pt/Ti/Si substrate, indexed to orthorhombic SbSI (JCPDS file No: 88-2407), (b) TEM image of a SbSI nanowire showing preferential <001> oriented growth, (inset showing a representative SAED pattern taken from the [100] zone axis); the marked fringe spacing of 0.51 nm corresponds to the (020) lattice plane of SbSI and (c) EDX spectrum of an individual SbSI nanowire.

The formation of SbSI nanowires can be explained by taking into account the inherent anisotropy of its unit cell building blocks as explained earlier in section

4.2.1. In this study, the vertical alignment was caused by the surface roughness of the Pt/Ti/Si substrate. Figure 4.11(a) shows the AFM topographical image and the corresponding roughness profiles (Figure 4.11(b)) obtained for an ultrasonically polished Pt/Ti/Si substrate. Figures 4.11(c) and (d) show photographs of Pt/Ti/Si substrates before and after sonication respectively.

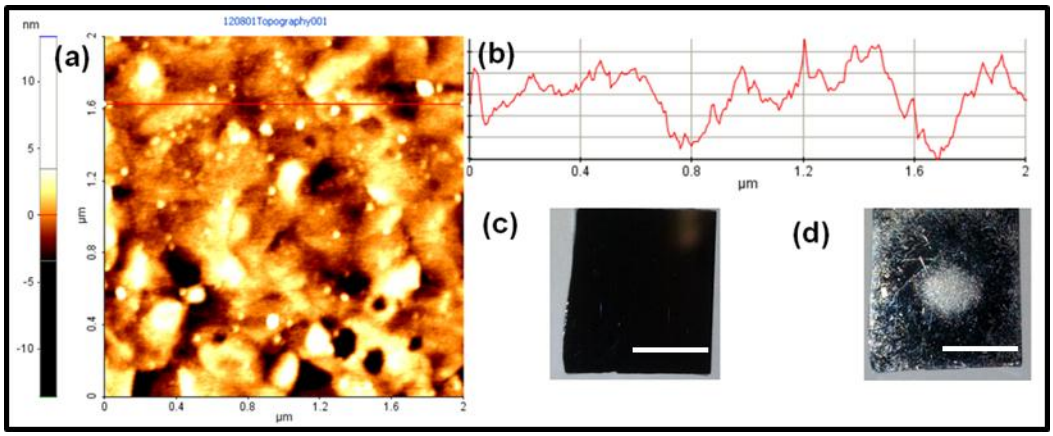

Figure 4.11. (a) AFM topographical image and (b) the corresponding roughness profiles obtained for an ultrasonically polished Pt/Ti/Si substrate. (c, d) Photographs of Pt/Ti/Si substrate before and after sonication, respectively (Scale bars: 0.5 cm).

High nucleation densities of nanostructures can be achieved by ultrasonically scratching a substrate surface.[56] As seen in Figure 4.9(a), high density growth of nanowires can be formed by surface roughening due to an increased number of binding sites for SbSI nucleation. Introducing surface irregularities effectively lowers the interfacial energy between the crystal nuclei and the substrate,[38,39,57] hence minimising the nucleation barrier and facilitating the growth of SbSI nanowires. The inherent growth anisotropy of SbSI as well as the anisotropy of the surface of the scratched substrate together induce an anisotropic strain,[57] and thus

confine the diffusion of SbSI molecules to 1D resulting in vertically aligned arrays of SbSI nanowires.

The bulk ferroelectric characteristics of SbSI nanowires formed on rough Pt/Ti/Si substrates were studied by P-E hysteresis loop acqusition. The well-defined P-E hystseresis (Figure 4.12) provided solid evidence for the existence of ferroelectricity in synthesised arrays of SbSI nanowires. The nanowire arrays showed a coercive field ~ 20 kV cm^{-1}, spontaneous polarisation (P_s) ~ 3.5 μC cm^{-2}, and remanant polarisation (P_r) ~ 2.1 μC cm^{-2}, which are comparable with that of *c*-axis oriented SbSI thin films.[33] Nanoscale PFM characterisation on individual SbSI nanowires was unsuccessful due to the difficulty in positioning the tip at a desired location on the nanowire.

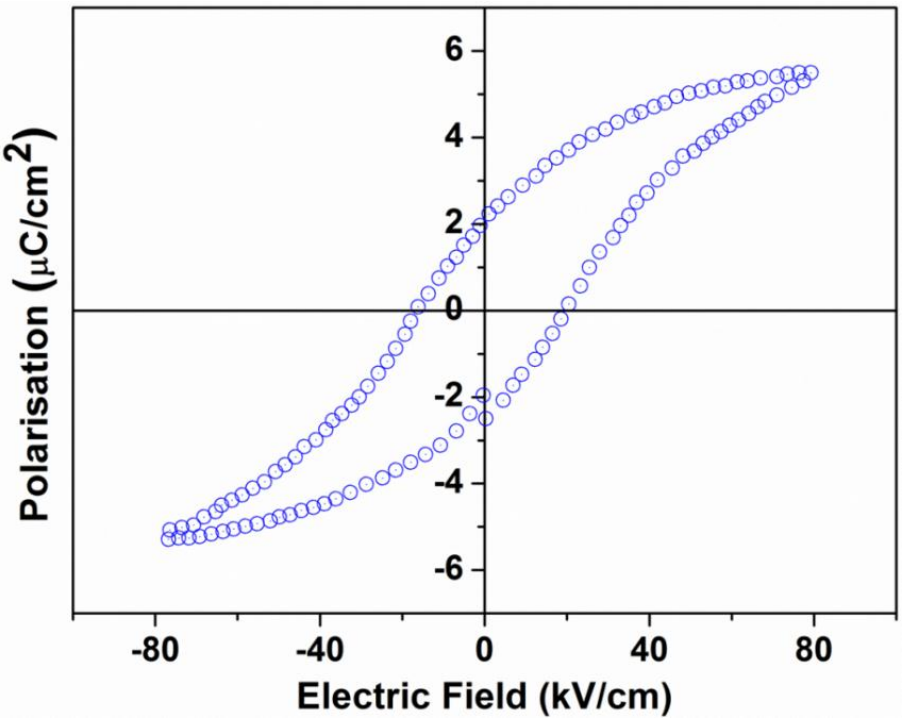

Figure 4.12. Polarisation-electric field hysteresis loop obtained from SbSI nanowire arrays formed on a Pt/Ti/Si substrate.

4.4 Conclusion

In summary, arrays of *c*-axis oriented SbSI nanorods were synthesised by a surface roughness assisted vapour deposition method on AAO/Ti/Si substrates. The growth of SbSI nanorods proceeded via a seedless vapour-solid mechanism. XRD and TEM-SAED analysis of the as-synthesised SbSI nanorods confirmed their single crystalline nature and their preferred <001> oriented growth. The surface roughness of the AAO substrate played a crucial role in vertically orienting the SbSI nanorods, by providing a large number of binding sites for nucleation. The inherent growth anisotropy of SbSI as well, as the roughness of the substrate, together confined the diffusion of SbSI molecules to one dimension resulting in vertically aligned arrays of SbSI nanowires. PFM studies revealed the presence of switchable ferroelectric and piezoelectric responses in individual SbSI nanorods. A 180° phase difference was observed during ferroelectric switching which could be attributed to the presence of the formation of two oppositely oriented (180°) ferroelectric domains, due to the *c*-axis oriented single crystalline nature of the SbSI nanorods. Surface-roughness assisted synthesis was also used to fabricate vertically aligned SbSI nanowire arrays on surface-roughened conducting Pt/Ti/Si substrates. The highly dense arrays of nanowires formed were single crystalline, with predominant growth along their *c*-axis, and displayed good ferroelectric behaviour.

4.5 References

(1) Rørvik, P. M.; Grande, T.; Einarsrud, M.-A. *Adv. Mater.* **2011**, *23*, 4007.

(2) Handoko, A. D.; Goh, G. K. L. *Science of Advanced Materials* **2010**, *2*, 16.

(3) Mitsui, T. Ferroelectrics and Antiferroelectrics. In *Springer Handbook of Condensed Matter and Materials Data*; Martienssen, W., Warlimont, H., Eds.; Springer: Berlin Heidelberg, 2005; pp 903.

(4) Fatuzzo, E.; Nitsche, R.; Harbeke, G.; Ruppel, W.; Roetschi, H.; Merz, W. J. *Physical Review* **1962**, *127*, 2036.

(5) Kern, R. *J. Phys. Chem. Solids* **1962**, *23*, 249.

(6) Hamano, K.; Nakamura, T.; Ishibash.Y; Ooyane, T. *J. Phys. Soc. Jpn.* **1965**, *20*, 1886.

(7) Imai, K.; Kawada, S.; Ida, M. *J. Phys. Soc. Jpn.* **1966**, *21*, 1855.

(8) Yoshida, M.; Yamanaka, K.; Hamakawa, Y. *Jpn J Appl Phys* **1973**, *12*, 1699.

(9) Sime, R. J. *J. Phys. Chem.* **1963**, *67*, 501.

(10) Berlincourt, D.; Nitsche, R.; Merz, W. J.; Jaffe, H. *Appl. Phys. Lett.* **1964**, *4*, 61.

(11) Fridkin, F.; Gerzanich, E.; Groshik, I.; Lyakhovitskaya, V. *ZhETF Pis ma Redaktsiiu* **1966**, *4*, 201.

(12) Nitsche, R.; Merz, W. J. *J. Phys. Chem. Solids* **1960**, *13*, 154.

(13) Belyaev, L.; Groshik, I.; Lyakhovitskaya, V.; Nosov, V.; Fridkin, V. *ZhETF Pis ma Redaktsiiu* **1967**, *6*, 481.

(14) Ueda, S.; Tatsuzak.I; Shindo, Y. *Phys. Rev. Lett.* **1967**, *18*, 453.

(15) Fridkin, V. M.; Groshik, II; Lakhoviz.Va; Mikhailo.Mp; Nosov, V. N. *Appl. Phys. Lett.* **1967**, *10*, 354.

(16) Mori, T.; Sawaguch.E. *J. Phys. Soc. Jpn.* **1968**, *25*, 1195.

(17) Kikuchi, A.; Oka, Y.; Sawaguch.E. *J. Phys. Soc. Jpn.* **1967**, *23*, 337.

(18) Audzijonis, A.; Grigas, J.; Kajokas, A.; Kvedaravicius, S.; Paulikas, V. *Ferroelectrics* **1998**, *219*, 37.

(19) Semiconductors: Non-Tetrahedrally Bonded Elements and Binary Compounds I. In *Landolt-Börnstein - Group III Condensed Matter*; Madelung, O., Rössler, U., Schulz, M., Eds.; Springer-Verlag, 1998; Vol. III/17E-17F-41C.

(20) Bhalla, A. S.; Newnham, R. E.; Cross, L. E.; Dougherty, J. P.; Smith, W. A. *Ferroelectrics* **1981**, *33*, 3.

(21) Johannes, R.; Haas, W. *Appl. Opt.* **1967**, *6*, 1059.

(22) Surthi, S.; Kotru, S.; Pandey, R. K. *Integrated Ferroelectrics* **2002**, *48*, 263.

(23) Kotru, S.; Liu, W.; Pandey, R. K. "PLD growth of high vapor pressure antimony sulpho-iodide ferroelectric films for IR applications"; Proceedings of the 12th IEEE International Symposium on Applications of Ferroelectrics, ISAF 2000., 2000.

(24) Brown, M. P.; Newnham, S. J.; Smith, P. W. "The application of SbSI and other ferroelectric materials to the generation of solitons and shock waves on nonlinear high voltage transmission lines"; Seventh International Conference on Dielectric Materials, Measurements and Applications (Conf. Publ. No. 430), 1996.

(25) Xu, Y. H.; Del Monte, F.; Mackenzie, J. D.; Namjoshi, K.; Muggli, P.; Joshi, C. *Ferroelectrics* **1999**, *230*, 313.

(26) Nowak, M.; Mroczek, P.; Duka, P.; Kidawa, A.; Szperlich, P.; Grabowski, A.; Szala, J.; Moskal, G. *Sensors and Actuators A: Physical* **2009**, *150*, 251.

(27) *The International Technology Roadmap for Semiconductors: 2011 Edition, Emerging research materials and Emerging research devices; http://www.itrs.net/Links/2011ITRS/2011Chapters/2011ERM.pdf, http://www.itrs.net/Links/2011ITRS/2011Chapters/2011ERD.pdf.*

(28) Solayappan, N.; Raina, K. K.; Pandey, R. K.; Varshney, U. *J. Mater. Res.* **1997**, *12*, 825.

(29) Dziuba, Z. *J. Cryst. Growth* **1976**, *35*, 340.

(30) Zadorozhnaya, L. A.; Lyachovitskaya, V. A.; Givargizov, E. I.; Belyaev, L. M. *J. Cryst. Growth* **1977**, *41*, 61.

(31) Arivuoli, D.; Gnanam, F. D.; Ramasamy, P. *J. Cryst. Growth* **1986**, *79*, 432.

(32) Arivuoli, D.; Gnanam, F. D.; Ramasamy, P. *Mater. Chem. Phys.* **1987**, *16*, 181.

(33) Surthi, S.; Kotru, S.; Pandey, R. K. *J. Mater. Sci. Lett.* **2003**, *22*, 591.

(34) Wang, C.; Tang, K.; Yang, Q.; Hai, B.; Shen, G.; An, C.; Yu, W.; Qian, Y. *Inorg. Chem. Commun.* **2001**, *4*, 339.

(35) Yang, Q.; Tang, K.; Wang, C.; Hai, B.; Shen, G.; An, C.; Zhang, C.; Qian, Y. *J. Cryst. Growth* **2001**, *233*, 774.

(36) Voynarovych, I. M.; Gomonnai, A. V.; Solomon, A. M.; Azhniuk, Y. M.; Kikineshi, A. A.; Pinzenik, V. P.; Kis-Varga, M.; Daroczy, L.; Lopushansky, V. V. *J Optoelectron Adv M* **2003**, *5*, 713.

(37) Nowak, M.; Szperlich, P.; Bober, Ł.; Szala, J.; Moskal, G.; Stróż, D. *Ultrason. Sonochem.* **2008**, *15*, 709.

(38) Ho, S.-T.; Chen, K.-C.; Chen, H.-A.; Lin, H.-Y.; Cheng, C.-Y.; Lin, H.-N. *Chem. Mater.* **2007**, *19*, 4083.

(39) Ho, S.-T.; Wang, C.-Y.; Liu, H.-L.; Lin, H.-N. *Chem. Phys. Lett.* **2008**, *463*, 141.

(40) Balarew, C.; Ivanova, M. *Cryst. Res. Technol.* **1986**, *21*, K171.

(41) Liu, C.; Hu, Z.; Wu, Q.; Wang, X.; Chen, Y.; Sang, H.; Zhu, J.; Deng, S.; Xu, N. *J. Am. Chem. Soc.* **2005**, *127*, 1318.

(42) Cao, G. *Nanostructures and Nanomaterials : Synthesis, Properties, and Applications*, 1 ed.; Imperial College Press: London, 2004; Vol. 1.

(43) Tien, L.-C.; Chen, Y.-J. *Appl. Surf. Sci.* **2012**, *258*, 3584.

(44) Fang, J.; Aharonovich, I.; Levchenko, I.; Ostrikov, K.; Spizzirri, P. G.; Rubanov, S.; Prawer, S. *Cryst Growth Des* **2012**, *12*, 2917.

(45) Miyabe, S.; Nakano, T.; Ishimoto, T.; Takano, N.; Adachi, T.; Iwaki, H.; Kobayashi, A.; Takaoka, K.; Urnakoshi, Y. *Materials Transactions* **2007**, *48*, 343.

(46) Dönges, E. *Z. Anorg. Allg. Chem.* **1950**, *263*, 112.

(47) Iwanaga, H.; Fujii, M.; Takeuchi, S. *Phase Transitions* **1998**, *66*, 147.

(48) Wang, L.; Zhang, X.; Zhao, S.; Zhou, G.; Zhou, Y.; Qi, J. *Appl. Phys. Lett.* **2005**, *86*, 024108.

(49) Balke, N.; Bdikin, I.; Kalinin, S. V.; Kholkin, A. L. *J. Am. Ceram. Soc.* **2009**, *92*, 1629.

(50) Jesse, S.; Baddorf, A. P.; Kalinin, S. V. *Appl. Phys. Lett.* **2006**, *88*, 062908.

(51) Jesse, S.; Lee, H. N.; Kalinin, S. V. *Rev. Sci. Instrum.* **2006**, *77*, 073702.

(52) Rodriguez, B. J.; Jesse, S.; Alexe, M.; Kalinin, S. V. *Adv. Mater.* **2008**, *20*, 109.

(53) Varghese, J.; Barth, S.; Keeney, L.; Whatmore, R. W.; Holmes, J. D. *Nano Lett.* **2012**, *12*, 868.

(54) Kalinin, S. V.; et al. *Rep. Prog. Phys.* **2010**, *73*, 056502.

(55) Narayanan, S.; Pandey, R. K. *Isaf '94 - Proceedings of the Ninth Ieee International Symposium on Applications of Ferroelectrics* **1994**, 309.

(56) Bhusari, D. M.; Yang, J. R.; Wang, T. Y.; Chen, K. H.; Lin, S. T.; Chen, L. C. *Mater. Lett.* **1998**, *36*, 279.

(57) Tandra, G.; Subhajit, B.; Soumitra, K.; Apurba, D.; Supriya, C.; Subhadra, C. *Nanotechnology* **2008**, *19*, 065606.

Chapter 5

Fabrication of Arrays of PZT Nanodots via Block Co-Polymer Self-Assembly

5.1 Abstract

Chapter 5 presents a simple methodology for the fabrication of two dimensional arrays of lead zirconate titanate (PZT) nanodots on n-doped Si substrates, via the directed self-assembly of PS-*b*-PEO block-co-polymer templates. This approach produced highly ordered PZT nanodot patterns, with lateral widths and heights as small as 20 and 10 nm respectively, and a coverage density as high as ~ 68×10^9 nanodots cm^{-2}. The existence of a pervoskite phase in the nanodots was confirmed by X-ray diffraction and X-ray photoelectron spectroscopy. The piezo-amplitude and ferroelectric domain response obtained from the nanodots, through piezoresponse force microscopy, confirmed the presence of ferroelectricity in the PZT arrays. Notably, PZT nanodots with a thickness ~ 10 nm, which is close to the critical size limit of PZT, showed ferroelectric behaviour. The presence of a multi-*a*/*c* domain structure in the nanodots is attributed to their polycrystallinity nature.

5.2 Introduction

The continuing miniaturisation of ferroelectric-based memories needs the creation of isolated nanosized ferroelectric domains (< 100 nm) to achieve ultra-high density ferroelectric memory units per unit area.[1-7] Efforts have been made by a number of research groups to realise this goal by nanoscaling ferroelectric materials using different 'top-down' and 'bottom-up' approaches.[3,8-10] Fabrication of two dimensional (2D) arrays of ferroelectric nanoislands or dots is an ideal approach for forming isolated nanodomains, where the individual units can store physically separate bits of data.[3,5,6,8,11] Isolated single-crystalline ferroelectric nanostructures have shown improved memory characteristics such as high polarisation retention

compared to their thin film counterparts, due to the presence of single ferroelectric domains.[11] Techniques such as electron beam lithography,[5,6] nanoimprint lithography,[12,13] dip-pen lithography,[14] sol-gel self-assembly[15-17] and templating[7,11,18-20] have been used successfully to fabricate arrays of discrete nanoislands or dots. Although 'top-down' lithography based techniques have been successful in making precisely positioned ferroelectric nanodots, their inherent feature-size limitations, low throughput and high processing cost makes these techniques less prevalent.[21] While self-assembly-based 'bottom-up' methods offer facile high-throughput synthesis of ferroelectric nanoislands, they suffer from poor ordering and limited control over feature size, which limits their practical application.[15-17,21] Template-assisted synthesis is a simplistic low-cost route for fabricating ferroelectric nanodots, due to the number of deposition methods that can be utilised and good control over the dimensions of the nanostructures formed.[7,11,18-20] For example, Lee *et al.*[3] fabricated individually addressable epitaxial arrays of PZT nanodot capacitors (~ 60 nm in diameter and ~ 20 – 40 nm in height) with a density of 32 x 10^9 nanodots cm^{-2} using anodic aluminium oxide (AAO) templates. However, the use of AAO as a template is limited, due to the difficulty in forming membranes on desired substrates and typically poor ordering at low dimensions (< 50 nm). Nanosphere lithography (NSL) has also been used to obtain 2D ferroelectric nanostructures, but the minimum feature size that could be achieved by this method is limited to ~ 50 nm.[15-17]

5.2.1 Block copolymer self-assembled templates

Block copolymer (BCP) based self-assembly has emerged as a viable 'bottom-up' patterning technique for nanostructures, due to the ability to form different types of

2D and 3D nanoscale patterns on various substrates.[22,23] These self-assembled patterns have been used as nanolithographic masks, as well as templates for the fabrication of arrays of dots and wires of inorganic organic nanostructures.[22,23] Recently, BCP self-assembly has achieved the capability of precisely patterning nanostructures in 2D and 3D geometry with sub-10 nm resolution.[24-26] The capabilities of BCP patterning techniques therefore have the potential to generate ordered arrays of ferroelectric nanodots and nanowires. The use of self-assembled BCPs to produce ferroelectric nanostructures is still in its infancy and has not yet been fully explored. Diblock copolymers have been the most widely used for creating self-assembled patterns of nanostructures.[22,23] Kang *et al.*[8] used polystyrene-*block*-poly(ethyleneoxide) (PS-*b*-PEO) diblock polymer templates for the confined crystallisation of the ferroelectric polymer PVDF-TrFE into periodically aligned nanowire patterns trenches, 30 nm in width and 50 nm in periodicity. Zoelen *et al.*[27] used polystyrene-*block*-poly(4-vinyl pyridine) [PS-*b*-P4VP] for the fabrication of line patterns of $PbTiO_3$ nanoparticles, with a mean height ~ 25 nm and periodicity ~ 65 nm. Kim *et al.*[28] prepared high-density arrays of $PbTiO_3$ nanodots, with mean heights of 7 nm and diameters of 22 nm, using the self-assembled BCP PS-*b*-P4VP. To form $PbTiO_3$ nanodot patterns, the former group employed pulsed laser deposition on PS-*b*-P4VP lamellae, whilst the latter group utilised micelle-based incorporation of a $PbTiO_3$ precursor into the PS-*b*-P4VP thin film, due to the favourable interaction of the precursor with the polar P4VP polymer block. The interaction of metallic precursors towards the P4VP polar block in PS-*b*-P4VP occurred due to the selective co-ordination of the metal ions (Pb^{2+} and Ti^{4+}) with the polar functional moiety (pyridine) present in block. Similar

interactions have been reported in the fabrication of arrays of iron oxide nanoparticles using polystyrene-*block*-polyethylene oxide (PS-*b*-PEO) thin films.[29] This metal ion impregnation method has great potential for generating nanostructures in a single step, without the requirement for polymer etching, as the annealing process not only crystallises the nanostructures but also removes the polymer.

This chapter reports the synthesis of highly ordered 2D arrays of PZT ($PbZr_{0.3}Ti_{0.7}O_3$) nanodots using self-assembled PS-*b*-PEO thin films. PZT was studied due to its commercial importance and its excellent piezoelectric and ferroelectric characteristics.[30] Furthermore, the nanoscale ferroelectric and piezoelectric properties of arrays of PZT nanodots were probed using piezoresponse force microscopy (PFM).

5.3 Results and Discussion

5.3.1 Structural and morphological characterisation of PZT nanodot arrays

Self-assembled thin films of PS-*b*-PEO (42-11) were fabricated on n-doped Si substrates by spin coating the polymer solution onto the substrate followed by solvent annealing and ethanol treatment, as discussed in detail in Chapter 2, Section 2.4; (42-11) defines the number average molecular weight in kg $mol^{-1}$of PS and PEO block respectively. Figures 5.1(a) and (b) shows scanning electron microscopy (SEM) images of self-assembled PS-*b*-PEO (42-11) thin films formed on Si substrates; the bright contrast represents the PS block and the dark contrast represents the PEO block. The hydrophilic PEO block phase separates from the hydrophobic PS block in the form of cylindrical domains. The centre-to-centre cylinder spacing in the phase separated polymer was ~ 40 nm, with a mean PEO

cylindrical diameter ~ 30 nm and film thickness of ~ 40 nm. Arrays of PZT nanodots were formed by the simple inclusion of a PZT precursor solution into the PEO component of the thin film via spin coating, followed by UV/ozone treatment to completely remove the polymers. As shown in Figures 5.1(c) and (d), well-ordered arrays of isolated PZT nanodots with diameter around 30 ± 5 nm were fabricated on an n-doped Si substrate. Close examination of the SEM images revealed that isolated nanodots formed, with only few dots being interconnected. The placement of the nanodots mimicked the original self-assembled block copolymer pattern. The cross-sectional transmission electron microscopy (TEM) image, Figure 5.1(d) inset, of PZT nanodots formed further confirmed that the isolated nanodots were polycrystalline and had an average height of ~15 nm. The mean thickness and diameter of PZT nanodots fabricated using the PS-*b*-PEO (42-11) BCP were less than half the dimensions previously reported by Lee *et al.*[3]. Isolated arrays of PZT nanodots are ideal for the formation of individual ferroelectric domains to achieve high storage density in memory applications.[3,5,6,11] The PZT nanodots fabricated using PS-*b*-PEO (42-11) had a coverage density 42×10^9 nanodots cm^{-2} which in turn gives a memory density of 42 Gb cm^{-2}, which is greater than that previously reported.[3]

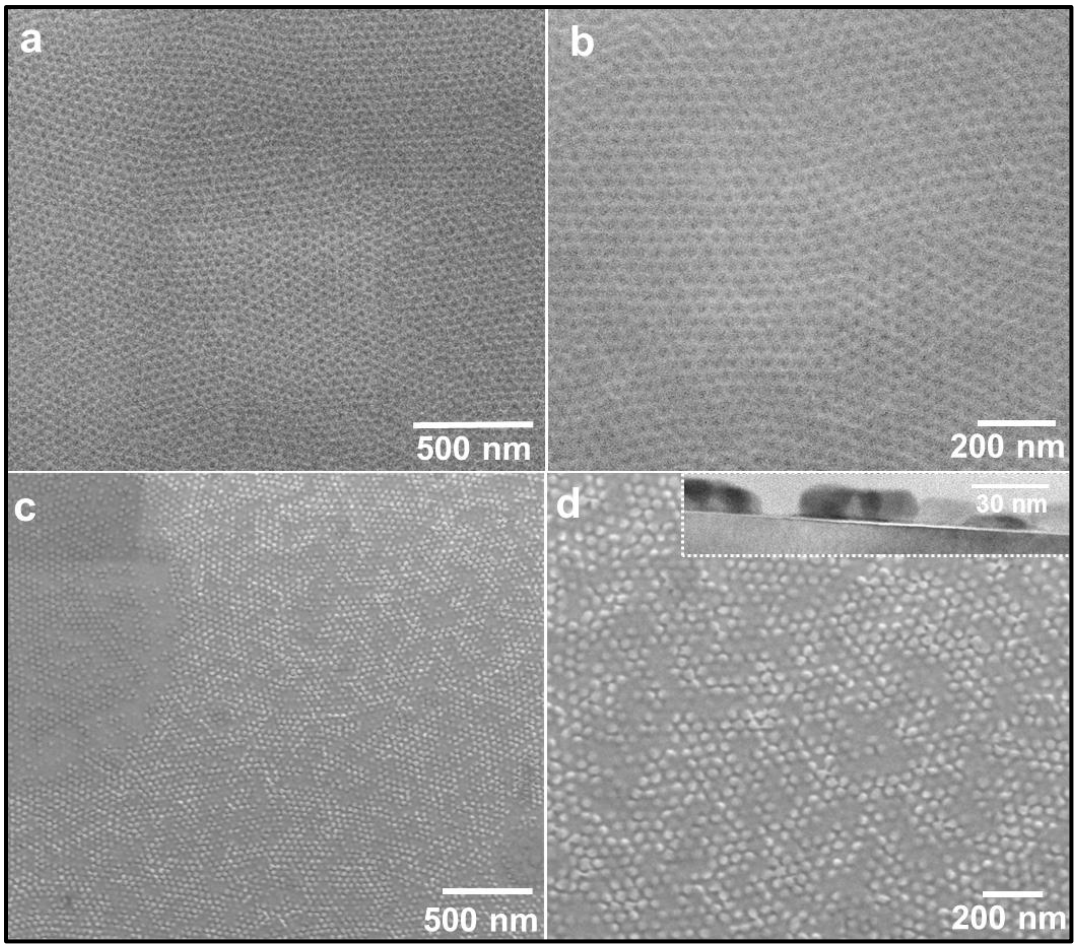

Figure 5.1. Plan-view SEM images of: (a) a PS-*b*-PEO (42-11) self-assembled thin film formed on an n-doped Si substrate, (b) magnified image of the template, (c) array of PZT nanodots deposited using the PS-*b*-PEO thin film at 600 °C and (d) magnified image of PZT nanodots (inset shows cross-sectional TEM image of isolated nanodots).

The size, thickness, separation, distance, and long-range ordering of the nanodots can be controlled by adjusting the molecular weight of any of the components in a BCP.[23] The size of an individual polymer block usually scales with molecular weight, *i.e.* a decrease in molecular weight reduces the size of polymer domains.[23] This hypothesis was utilised to reduce the size and thickness of the PZT nanodots

generated on Si substrates, by using the BCP PS-*b*-PEO (32-11), where the number-average molecular weight, (M_n) of PS was reduced to 32 kg mol^{-1}. The atomic force microscope (AFM) image of a self-assembled PS-*b*-PEO (32-11) thin film formed on an n-doped Si substrate (Figure 5.2(a)) shows that the ordering of the PS-*b*-PEO is significantly improved, while the size of the PEO domains (dark contrast) decreases. As seen in Figure 5.2(a), the PS-*b*-PEO (32-11) thin film possesses high long-range ordering, as evident from the hexagonal arrangement of PEO block domains. A decrease in the size and thickness of the PEO domains leads to a decrease the size of the PZT nanodots formed, as the metals have a preferential affinity towards the hydrophilic PEO block. PS-*b*-PEO (32-11) thin film had an average thickness of ~ 20 nm. As shown in Figures 5.2(b) and (c), the PZT nanodots fabricated using the PS-*b*-PEO (32-11) thin film had smaller dimensions (~ 20±5 nm in diameter, and ~ 10 nm in thickness) and a larger mean centre-to-centre cylinder spacing (~ 30 nm) compared to the nanodots generated from the PS-*b*-PEO (42-11) template. The morphology of the nanodots formed using the PS-*b*-PEO (32-11) template was pyramidal compared to semi-spherical with the PS-*b*-PEO (42-11). The inset in Figure 5.2(c) shows the FFT pattern obtained for the arrays of PZT nanodots, which confirms the hexagonal long-range ordering of the arrays. The coverage density of the PZT nanodots was ~ 68 × 10^9 nanodots per cm^{-2}, for the PS-*b*-PEO (32-11) template, which was greater than with the PS-*b*-PEO (42-11). This can be explained by the decrease in center-to-center cylinder spacing between the polymer blocks in (32-11) template.

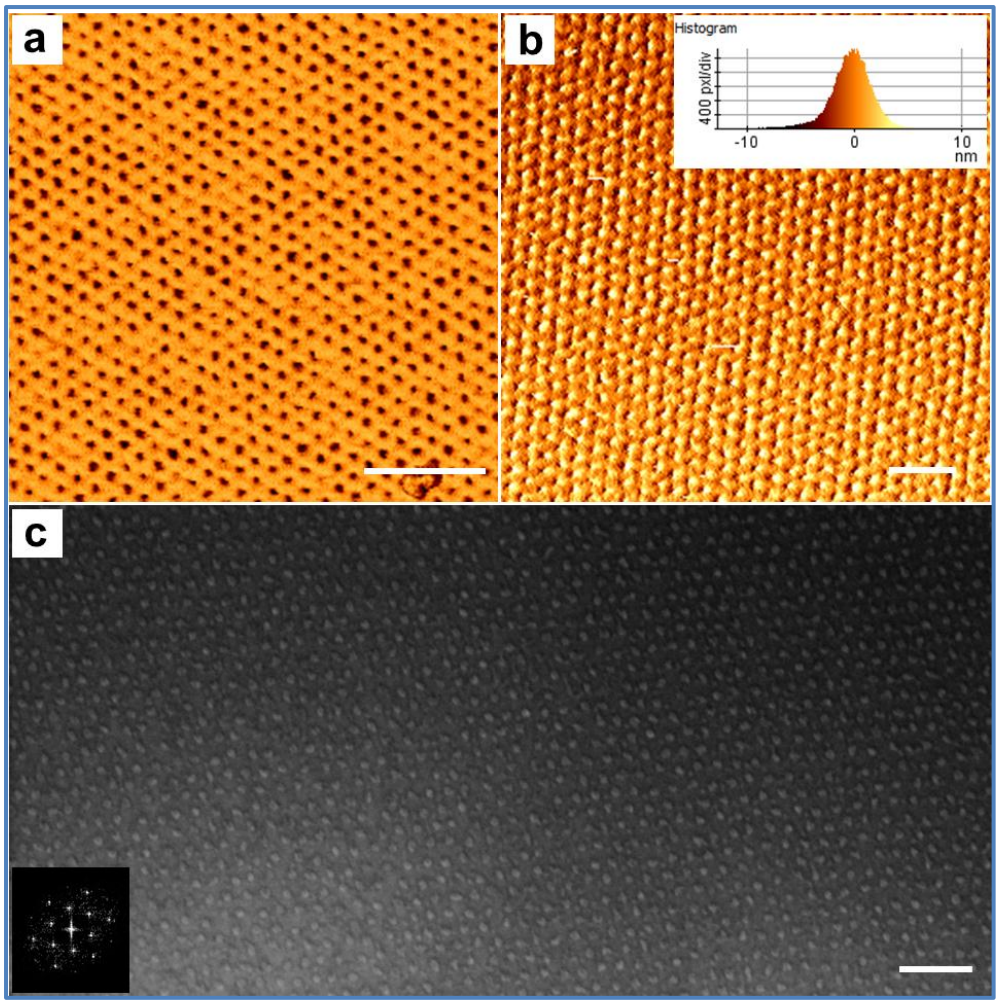

Figure 5.2. AFM topography image of: (a) a PS-*b*-PEO (32-11) self-assembled thin film formed on a n-doped Si substrate and (b) arrays of PZT nanodots formed at using a PS-*b*-PEO (32-11) thin film (inset shows the histogram of the nanodot size). (c) Plan-view SEM image of an array of PZT nanodots formed from a PS-*b*-PEO (32-11) template, the FFT pattern in the inset shows the hexagonal ordering of the nanodots. (Scale bars, 200 nm).

The formation of PZT nanodots using PS-*b*-PEO can be explained by the selective intramolecular or intermolecular co-ordination between the metal ions (Pb^{2+}, Zr^{4+}, and Ti^{4+}) present in the precursor solution and the hydrophilic PEO chains present in PS-*b*-PEO. PEO is known to have a good affinity with the cationic species,[29,31] and

the tendency towards multiple co-ordination is favoured by its all-trans zig-zag, or cis-helical, configuration (Figure 5.3).[31] Thus the Pb^{2+}, Zr^{4+}, and Ti^{4+} ions present in the precursor solution form dative bond with the ether functional moieties (-O-) present in the PEO block, whilst being excluded from the hydrophobic PS block, eventually resulting in the nanodot formation.[29]

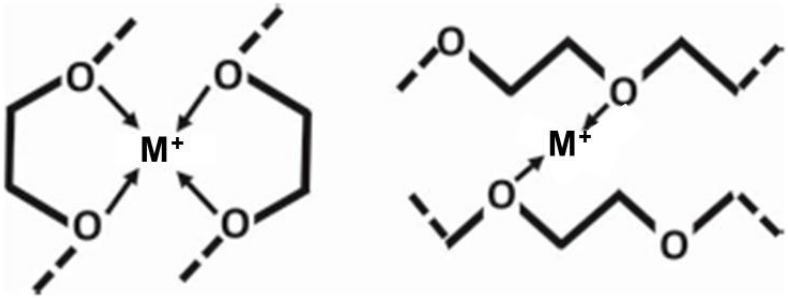

Figure 5.3. Schematic illustration of the possible metal cation-PEO block co-ordination by means of the cis-helical and all-trans zig-zag geometry of the PS-b-PEO chains.[29]

Figure 5.4 shows the slow-scan X-ray diffraction (XRD) pattern obtained for an array of PZT nanodots template from a PS-*b*-PEO (42-11) polymer on a n-doped Si substrate. Diffraction peaks observed at 2θ = 22, 32.1, 38.2 were indexed to (001)/(100), (110)/(101) and (111) reflection planes of tetragonal pervoskite PZT, (PDF no. 33-0784). Similar XRD patterns were obtained for arrays of PZT nanodots template from a PS-*b*-PEO (32-11) polymer.

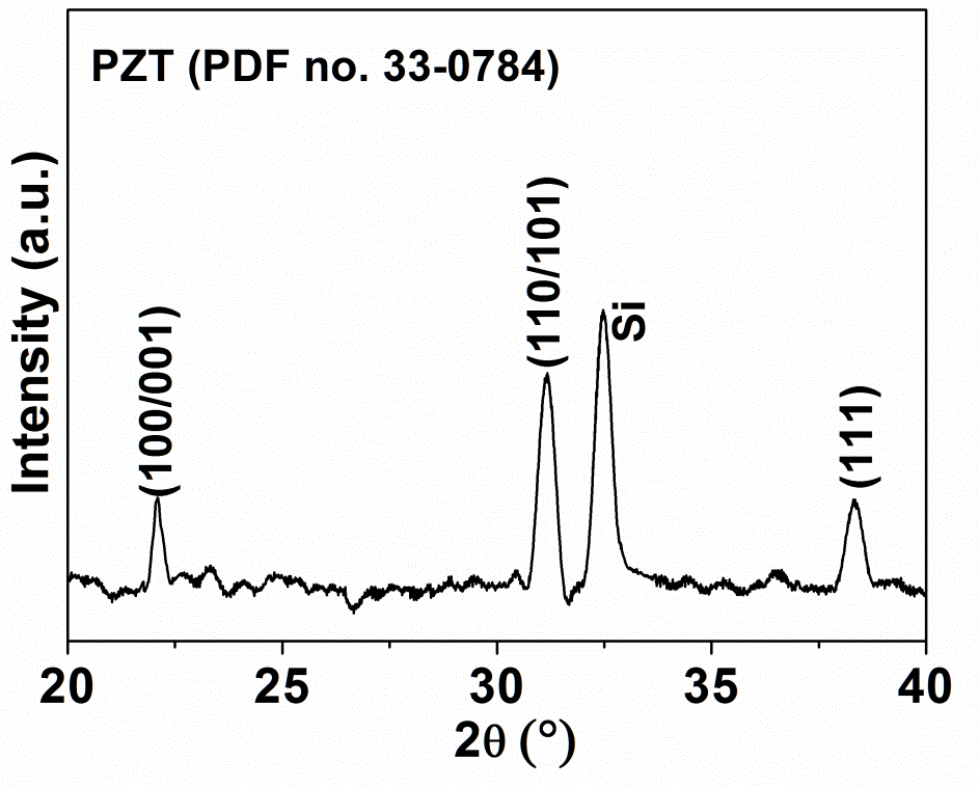

Figure 5.4. Slow-scan XRD pattern obtained for arrays of PZT nanodots template from a PS-*b*-PEO (42-11) polymer formed on an n-doped Si substrate; indexed to pervoskite PZT (PDF no. 33-0784).

In order to confirm the presence of a pervoskite phase, detailed X-ray photoelectron spectroscopy (XPS) analysis was carried out on PZT nanodot samples. Figure 5.5 shows the XPS survey spectrum and the high resolution core-level spectra of individual metal ions from arrays of PZT nanodots produced using the PS-*b*-PEO (42-11) template. The XPS survey spectrum (Figure 5.5(a)) shows dominant peaks of Pb, Zr, Ti, O along with the Si peaks from the substrate, confirming that no contamination occurred during the PZT deposition process. Figures 5.5(b) and (e) shows the high resolution core-level XPS spectra with deconvoluted fits of Pb (*4f*), Zr (*3d*), Ti (*2p*), and O (*1s*) respectively.

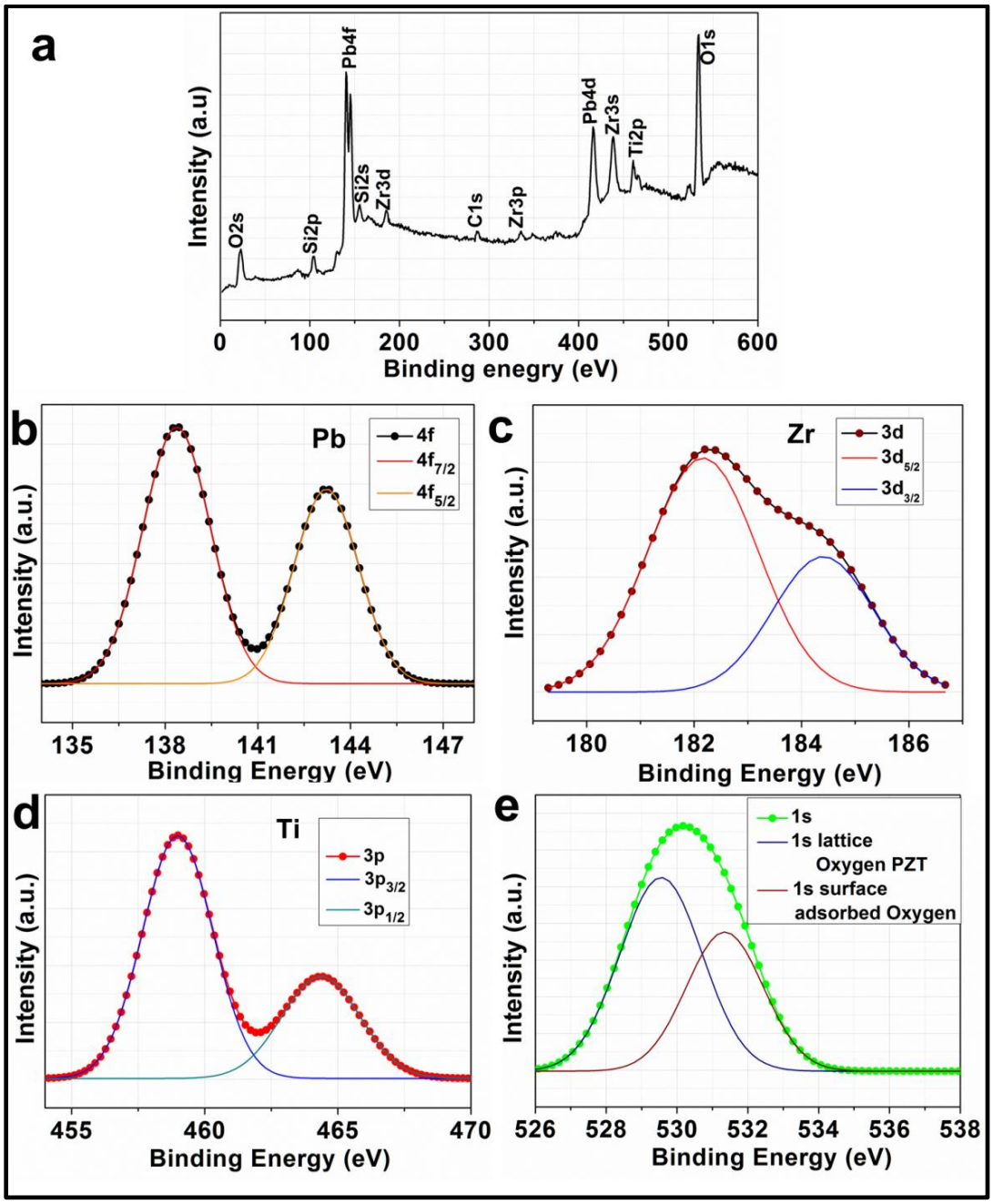

Figure 5.5. (a) XPS survey spectra of PZT nanodots template from a PS-*b*-PEO (42-11) polymer deposited on an n-doped Si substrate. Deconvoluted high resolution XPS spectra of: (b) Pb (4*f*), (c) Zr (3*d*), (d) Ti (3*p*) and (e) O (1*s*) from the PZT nanodots.

As observed in Figures 5.5(b) to (d), Pb, Zr, and Ti shows only one spin-orbit doublet, indicating the presence of a single chemical environment in the PZT nanodots synthesised. The values of core-level binding energies obtained for each metal present in PZT nanodots were, Pb ($4f_{7/2}$) = 138.25 eV, and Pb ($4f_{5/2}$) = 143.11 eV, with a peak separation of 4.86 eV; Zr ($3d_{5/2}$) = 182.20 eV and Zr ($3d_{3/2}$) = 184.55 eV, with a peak separation of 2.35 eV; Ti ($3p_{3/2}$) = 458.81 eV and Ti ($3p_{1/2}$) = 464.25 eV, with a peak separation 5.44 eV. The O (1s) core-level spectrum was deconvoluted into two peaks, at 529.58 eV and 531.33 eV and were assigned to lattice oxygen and surface oxygen on the PZT nanodots respectively.[32] The observed binding energies were in good agreement with those previously reported for a pervoskite PZT chemical environment.[32]

5.3.2 Piezoresponse force microscopy analysis of arrays of PZT nanodots

Piezoresponse force microscopy (PFM) was used to investigate the ferroelectric functionality of the arrays of PZT nanodots. Figure 5.6 shows (a) the piezoresponse topography, (b) and (d) the amplitude and (c) and (e) phase images of PZT nanodots formed from a PS-*b*-PEO (42-11) template, as measured by vertical PFM; the piezoresponse amplitude and phase provide information on the local electromechanical activity and the direction of local polarisation, respectively.[33] The distinct bright and dark contrast in the piezoresponse amplitude images, shown in Figures 5.6(b) and (d), clearly highlight the presence of piezoelectric behaviour in the individual PZT nanodots. The bright contrast is an indication of a large out-of-plane polarisation response present in the nanodots, while the relatively dark contrast indicates less polarised regions.[33] PZT nanodots exhibited good piezoresponse over a large area (Figure 5.6(b)), with the majority of the dots showing a large out-of-

plane piezoresponse. Previous articles have reported that tetragonal PZT films show a very high out of-plane response.[34]

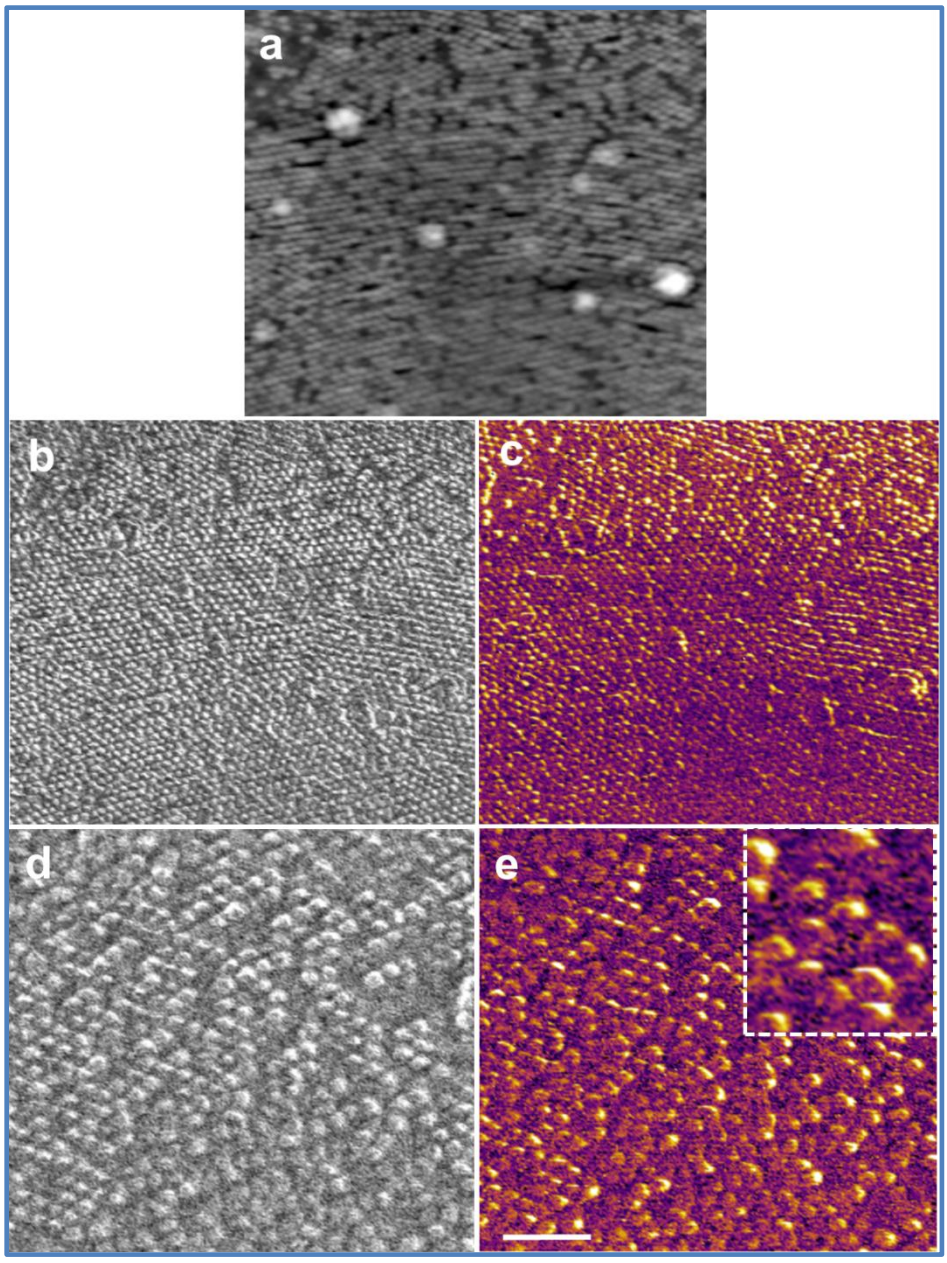

Figure 5.6. PFM images showing (a) topography, (b) amplitude and (c) phase profiles of PZT nanodot arrays fabricated using a PS-*b*-PEO (42-11) template on an n-doped Si substrate. (d, e) high resolution PFM amplitude and phase images of arrays of PZT nanodots (inset shows multi-domain structure). Scale bar, 200 nm.

The phase images in Figures 5.6(c) and (e) show that the ferroelectric domains present in the nanodots have a multi-domain structure, as evident from the orange and violet colour contrast. The random orientation of ferroelectric domains can be explained by the pseudo-epitaxial polycrystalline nature of PZT nanodots and is common in polycrystalline PZT films.[35] This hypothesis is supported by the polycrystalline nature of the nanodots as seen in TEM image (Figure 5.1(d)) XRD pattern (Figure 5.4) obtained for PZT nanodot samples, where the dots show reflections from (110) and (111) directions, indicating that the crystallographic orientation in the sample is not constrained to one orientation. This results in the formation of a multi-*a*/*c* domain (*a*-domain, parallel to the substrate plane; and *c*-domain, perpendicular to the plane) structure is expected. In Figure 5.6(c), some of the dots are composed of a single *c*-domain (orange contrast in top part), whilst dots at the bottom display multi-domains, with evidence of coupled phase contrasts in one dot. These phase contrast can be clearly seen in Figure 5.6(e) and in the magnified inset image. The dragging effect of tip near the curvature of the nanodots may also contribute to the PFM signal. The orientation of the bright and dark contrast on the nanodots may also be indicative of a relationship between the PFM scan direction and piezoresponse in the nanodots. As the tip rises up over a nanodot, it gets a different piezoelectric "push" from when it runs down on the other side. This tip convolution may also be able to contribute to the PFM signal.

Arrays of PZT nanodots fabricated using a PS-*b*-PEO (32-11) template also showed piezoelectric and ferroelectric responses. Figures 5.7(a) and (b) show the PFM amplitude and phase images obtained for these arrays respectively. As seen in the PFM amplitude image (Figure 5.7(a)), most of the nanodots displayed a strong out-

of-plane piezoresponse (bright contrast), while a few of them appeared dark. Close observation of the phase image (Figure 5.7(a)) shows the presence of multi-*a*/*c* domain structure with a high *c*-domain ratio. This observation is consistent with the PFM result obtained for PZT nanodots template from the PS-*b*-PEO (42-11) polymer. Significantly, these nanodots have a thickness ~10 nm and they still show ferroelectric behaviour, which agrees with the previous reports.[36] As in (42-11) sample, the dragging effect of tip should also be taken into account to interpret the PFM signal. Future work is aimed on switching experiments on a selected area of nanodots in order to confirm the presence of ferroelectric behaviour.

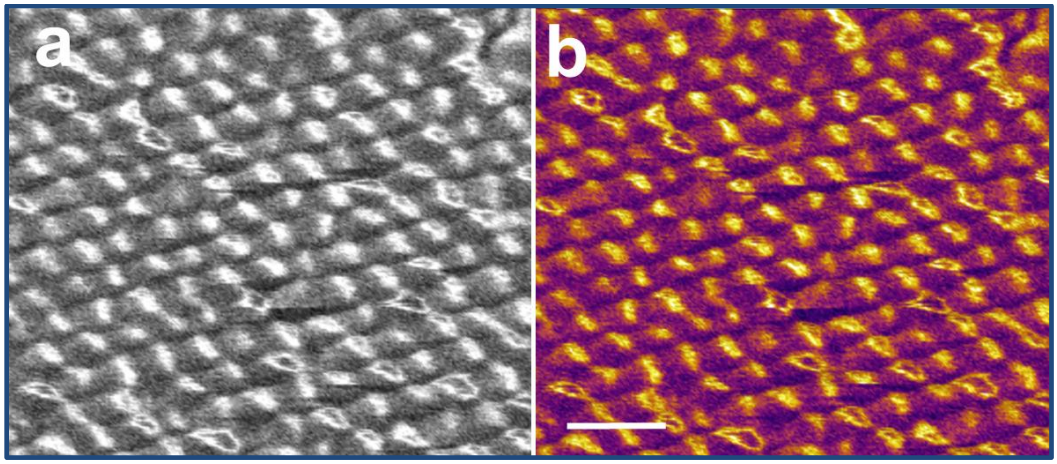

Figure 5.7. High resolution PFM (a) amplitude and (b) phase images of arrays of PZT nanodots fabricated using a PS-*b*-PEO (32-11) template on an n-doped Si substrate. Scale bar, 100 nm.

The variation observed in the domain structure within and among the PZT nanodots makes these arrays less ideal for ferroelectric memory cell applications, since currently the magnitude of switching cannot be well controlled.[37] Mono-domain structures could possibly be achieved by epitaxial growth of the nanodots on suitable

substrates. Nevertheless, the BCP template-assisted approach described in this chapter has great potential for producing highly ordered 2D arrays of ferroelectric nanodots. The same methodology can also be extended to fabricate laterally ordered ferroelectric and piezoelectric nanowire patterns.

5.4 Conclusion

In summary, a simple method for the fabrication of highly ordered arrays of PZT nanodots using self-assembled block copolymer templates has been demonstrated. PZT nanodots with lateral widths and thicknesses as small as 20 nm and 10 nm respectively were prepared PS-*b*-PEO polymer template. The hexagonal long-range ordering of these nanodots was improved by decreasing the molecular weight of the polystyrene (PS) block used in the PS-*b*-PEO template. XRD and XPS analysis confirmed the pervoskite structure of PZT nanodots synthesised. PFM studies on individual PZT nanodots confirmed the presence of piezoelectric and ferroelectric behaviour. The multi-domain structure in the nanodots was attributed to the co-existence of both *a*- and *c*-domains, due to their polycrystalline nature. Switching experiments on a selected area of nanodots has to be done in order to confirm the presence of ferroelectric behaviour.

5.5 References

(1) Ionescu, A. M. *Nat Nano* **2012**, *7*, 83.

(2) Bibes, M. *Nat Mater* **2012**, *11*, 354.

(3) Lee, W.; Han, H.; Lotnyk, A.; Schubert, M. A.; Senz, S.; Alexe, M.; Hesse, D.; Baik, S.; Gosele, U. *Nat Nano* **2008**, *3*, 402.

(4) *The International Technology Roadmap for Semiconductors: 2011 Edition, Emerging research materials and Emerging research devices;* http://www.itrs.net/Links/2011ITRS/2011Chapters/2011ERM.pdf, http://www.itrs.net/Links/2011ITRS/2011Chapters/2011ERD.pdf.

(5) Alexe, M.; Harnagea, C.; Hesse, D.; Gosele, U. *Appl. Phys. Lett.* **1999**, *75*, 1793.

(6) Alexe, M.; Harnagea, C.; Visinoiu, A.; Pignolet, A.; Hesse, D.; Gosele, U. *Scripta Mater.* **2001**, *44*, 1175.

(7) Shin, H.-J.; Choi, J. H.; Yang, H. J.; Park, Y. D.; Kuk, Y.; Kang, C.-J. *Appl. Phys. Lett.* **2005**, *87*, 113114.

(8) Kang, S. J.; Bae, I.; Shin, Y. J.; Park, Y. J.; Huh, J.; Park, S.-M.; Kim, H.-C.; Park, C. *Nano Lett.* **2010**, *11*, 138.

(9) Kusuma, D. Y.; Nguyen, C. A.; Lee, P. S. *The Journal of Physical Chemistry B* **2010**, *114*, 13289.

(10) Scott, J. F. *Integrated Ferroelectrics* **2000**, *31*, 139.

(11) Lee, J.-S.; Lee, B.-I.; Joo, S.-K. *Integrated Ferroelectrics* **2000**, *31*, 149.

(12) Shen, Z.; Chen, Z.; Lu, Q.; Qiu, Z.; Jiang, A.; Qu, X.; Chen, Y.; Liu, R. *Nanoscale Research Letters* **2011**, *6*, 474.

(13) Hu, Z.; Tian, M.; Nysten, B.; Jonas, A. M. *Nat Mater* **2009**, *8*, 62.

(14) Son, J. Y.; Shin, Y.-H.; Ryu, S.; Kim, H.; Jang, H. M. *J. Am. Chem. Soc.* **2009**, *131*, 14676.

(15) Szafraniak, I.; Harnagea, C.; Scholz, R.; Bhattacharyya, S.; Hesse, D.; Alexe, M. *Appl. Phys. Lett.* **2003**, *83*, 2211.

(16) Szafraniak, I.; Chu, M. W.; Harnagea, C.; Scholz, R.; Hesse, D.; Alexe, M. *Integrated Ferroelectrics* **2004**, *61*, 231.

(17) Kim, J.; Hong, J.; Park, M.; Zhe, W.; Kim, D.; Jang, Y. J.; Kim, D. H.; No, K. *Adv. Funct. Mater.* **2011**, *21*, 4277.

(18) Ma, W.; Harnagea, C.; Hesse, D.; Gosele, U. *Appl. Phys. Lett.* **2003**, *83*, 3770.

(19) Ma, W.; Hesse, D.; Gösele, U. *Small* **2005**, *1*, 837.

(20) Wenhui, M.; Dietrich, H.; Ulrich, G. *Nanotechnology* **2006**, *17*, 2536.

(21) Vrejoiu, I.; Alexe, M.; Hesse, D.; Gösele, U. *Adv. Funct. Mater.* **2008**, *18*, 3892.

(22) Kim, J. K.; Yang, S. Y.; Lee, Y.; Kim, Y. *Prog. Polym. Sci.* **2010**, *35*, 1325.

(23) Kim, H.-C.; Park, S.-M.; Hinsberg, W. D. *Chem. Rev.* **2009**, *110*, 146.

(24) Tavakkoli K. G., A.; Gotrik, K. W.; Hannon, A. F.; Alexander-Katz, A.; Ross, C. A.; Berggren, K. K. *Science* **2012**, *336*, 1294.

(25) Park, S.-M.; Liang, X.; Harteneck, B. D.; Pick, T. E.; Hiroshiba, N.; Wu, Y.; Helms, B. A.; Olynick, D. L. *ACS Nano* **2011**, *5*, 8523.

(26) Jeong, J. W.; Park, W. I.; Do, L.-M.; Park, J.-H.; Kim, T.-H.; Chae, G.; Jung, Y. S. *Adv. Mater.* **2012**, *24*, 3526.

(27) van Zoelen, W.; Vlooswijk, A. H. G.; Ferri, A.; Andringa, A.-M.; Noheda, B.; ten Brinke, G. *Chem. Mater.* **2009**, *21*, 4719.

(28) Kim, Y.; Han, H.; Kim, Y.; Lee, W.; Alexe, M.; Baik, S.; Kim, J. K. *Nano Lett.* **2010**, *10*, 2141.

(29) Ghoshal, T.; Maity, T.; Godsell, J. F.; Roy, S.; Morris, M. A. *Adv. Mater.* **2012**, *24*, 2390.

(30) Izyumskaya, N.; Alivov, Y. I.; Cho, S. J.; Morkoç, H.; Lee, H.; Kang, Y. S. *Crit. Rev. Solid State Mater. Sci.* **2007**, *32*, 111.

(31) Evans, C. C.; Bates, F. S.; Ward, M. D. *Chem. Mater.* **1999**, *12*, 236.

(32) Wakiya, N.; Kuroyanagi, K.; Xuan, Y.; Shinozaki, K.; Mizutani, N. *Thin Solid Films* **2000**, *372*, 156.

(33) Kholkin, A.; Kalinin, S.; Roelofs, A.; Gruverman, A. Review of Ferroelectric Domain Imaging by Piezoresponse Force Microscopy. In *Scanning Probe Microscopy: Electrical and Electromechanical Phenomena at the Nanoscale*; Kalinin, S., Gruverman, A., Eds.; Springer New York, 2007; pp 173.

(34) Harnagea, C.; Pignolet, A.; Alexe, M.; Hesse, D. *Integrated Ferroelectrics* **2002**, *44*, 113.

(35) Wu, A.; Vilarinho, P. M.; Shvartsman, V. V.; Suchaneck, G.; Kholkin, A. L. *Nanotechnology* **2005**, *16*, 2587.

(36) Chu, M.-W.; Szafraniak, I.; Scholz, R.; Harnagea, C.; Hesse, D.; Alexe, M.; Gosele, U. *Nat Mater* **2004**, *3*, 87.

(37) Rodriguez, B. J.; Gao, X. S.; Liu, L. F.; Lee, W.; Naumov, II; Bratkovsky, A. M.; Hesse, D.; Alexe, M. *Nano Lett.* **2009**, *9*, 1127.

Chapter 6

Conclusions and Future Work

6.1 Conclusions and Future Work

The ever-continuing miniaturisation of electronic components and devices gives impetus to scale the dimensions of ferroelectrics down to the nanometre-scale region. Various types' fabrication and characterisation methods have been evolved to study the nanostructuring in ferroelectric and related materials. Chapter 1 of this thesis provided an overview of the recent developments in the fabrication, characterisation and application of various nanoscale ferroelectric materials.

Chapter 2 outlined the experimental procedures and characterisation tools required to synthesise and analyse Sb_2S_3, SbSI and PZT nanostructures and described in detail the principles of block *co*-polymer based self-assembly and piezoresponse force microscopy in detail.

Chapter 3 described the preparation of size controlled arrays of Sb_2S_3 nanowires within the cylindrical pores of anodic aluminium oxide (AAO) templates (Sb_2S_3-AAO), utilising a solventless technique and the single-source precursor antimony (III) tris(diethyldithiocarbamate). The data reported demonstrated the single crystalline nature, and preferential <001> growth direction, of the Sb_2S_3 nanowires produced. The templating strategy also provided a way to address the ferroelectric functionality of individual Sb_2S_3 nanowires on an individual basis by piezoresponse force microscopy (PFM). PFM analysis showed that the majority of the Sb_2S_3 nanowires synthesised displayed single ferroelectric domain (180°) structures, due to the preferential alignment of dipoles along the polar *c*-axis. Furthermore, PFM switching studies demonstrated the reversible switching capabilities of individual and groups of Sb_2S_3 nanowires. The low stability of the ferroelectric domains in the Sb_2S_3 nanowires was revealed using time varied PFM phase imaging studies. In

summary, this work demonstrated the controlled synthesis of various diameter single crystalline Sb_2S_3 nanowires with switchable ferroelectricity and piezoelectricity. Further investigation of ferroelectric scaling phenomena in Sb_2S_3 in other morphological forms, such as thin films or as nanodot arrays, would be useful for practical applications such as nanocapacitor.[1] The future work will be aimed at further reducing the diameter of the nanowires to find out the critical size limit of ferroelectric behaviour.

The role of surface roughness in orienting arrays of SbSI nanowires, produced by vapour deposition, was discussed in Chapter 4. Vertically oriented arrays of antimony sulphoiodide (SbSI) nanowires were synthesised by surface roughness-assisted vapour deposition method on AAO/Ti/Si and Pt/Ti/Si substrates. The inherent growth anisotropy of SbSI, as well as the roughness of the substrate, confined the diffusion of SbSI molecules to one dimension resulting in vertically aligned arrays of SbSI nanowires. The as-grown SbSI nanostructures were single crystalline and <001> oriented, as revealed from structural analysis. Switching spectroscopy PFM experiments demonstrated, for the first time, the presence of switchable ferroelectricity and piezoelectricity in individual SbSI nanorods. The ferroelectric switching in SbSI nanorods was found to occur via a 180° ferroelectric domain reversal, due to the preferred orientation of the nanorods along the polar *c*-axis. This facile method deposition method could readily be adopted to fabricate technologically important ferroelectric or piezoelectric materials, such as PZT, on suitable substrates. The vertically oriented SbSI nanowires produced have potential application in energy harvesting, due to their high *c*-axis piezoresponse and should be the subject of future investigations. Future experiments will be focused on

fabricating SbSI nanowires of different diameter by controlling the surface roughness of the substrate used, for example by controlling the pore diameter of the AAO.

Fabrication of two dimensional arrays of ferroelectric nanoislands or nanodots is an ideal approach for generating isolated nanodomains, where the individual units can act as memory by storing physically separate bits of data in memory storage. Chapter 5 detailed a simple methodology for the fabrication of two dimensional arrays of lead zirconate titanate (PZT) nanodots on n-doped Si substrates, using self-assembled PS-*b*-PEO block-co-polymer templates. This templating approach produced highly ordered patterns of pervoskite PZT nanodots, with lateral width of individual dots as small sub-20 nm and heights around 10 nm, with a coverage density as high as 60×10^9 nanodots cm^{-2}. PFM analysis revealed that PZT nanodots with heights around 10 nm were close to the critical size limit of PZT, but still showed ferroelectric behaviour. The presence of a multi-*a*/*c* domain structure in the nanodots is attributed to their polycrystallinity. In general, the variation in the domain structure within and among the PZT nanodots makes these arrays currently non-ideal for ferroelectric memory cell applications, since the magnitude of switching cannot be well controlled.[2] Mono-domain structures can however possibly be achieved by directional anisotropy by epitaxial growth of these nanodots on suitable substrates. Nevertheless, this work demonstrated the capabilities of block copolymer-based self-assembly in creating highly ordered ferroelectric nanopatterns with periodicity as low as 20 nm. In addition, through this self-assembly approach laterally ordered lamellar ferroelectric line patterns can be fabricated. Future work is targeted on the creation of nanopatterns of other prominent ferroelectric materials,

such as $BaTiO_3$, $(K,Na)NbO_3$ and $Bi_4Ti_3O_{12}$ to produce high density ferroelectric memory cells.

The prospect for nanoferroelectrics research is promising as evident from the growing interest in theory, fabrication and application aspects of these nanostructures.[1,3-12] A basic understanding of the finite-size effect in nanoferroelectrics is a prerequisite for the development of new nanoscale devices and hence more theoretical studies in this area are required. Fabrication routes that have the capability to generate nanostructure patterns, with predictable shapes and controlled dimensions at desired locations on a substrate, are critical for the integration of novel nanoferroelectric components into electronic devices such as FeRAM. For instance, the potential of nanoimprint lithography[13-16] and block co-polymer based directed self-assembly[17-19] to produce highly ordered patterns of the nanostructures can be effectively exploited to achieve the above mentioned challenge. Efforts to enhance the spatial resolution of current characterisation tools will also be required to tackle future developments in nanoscale ferroelectric research.[20-22] Characterisation techniques such as PFM, scanning nonlinear dielectric microscopy,[23-25] tip-enhanced Raman spectroscopy[21,26] and transmission electron microscopy[27-30] needs special mention in this regard as their resolution capability has been greatly improved to study even Ångström level ferroelectric characteristics. The broad application spectrum of nanoscale ferroelectric materials, spanning from memory devices to self-powered nanogenerators, may fuel future interests in research and developments in this area. Progress in controlling ferroelectricity on the nanoscale offers great potential for nanoscale ferroelectric devices, especially ferroelectric field-effect transistors (FeFETs) and ferroelectric

tunnel junctions (FTJs).[4,6,31-33] The 2011 international technology road map for semiconductors has listed FTJs and FeFETs as two emerging memory technologies.[34]

6.2 References

(1) Lee, W.; Han, H.; Lotnyk, A.; Schubert, M. A.; Senz, S.; Alexe, M.; Hesse, D.; Baik, S.; Gosele, U. *Nat Nano* **2008**, *3*, 402.

(2) Rodriguez, B. J.; Gao, X. S.; Liu, L. F.; Lee, W.; Naumov, II; Bratkovsky, A. M.; Hesse, D.; Alexe, M. *Nano Lett.* **2009**, *9*, 1127.

(3) Vrejoiu, I.; Alexe, M.; Hesse, D.; Gösele, U. *Adv. Funct. Mater.* **2008**, *18*, 3892.

(4) Ionescu, A. M. *Nat Nano* **2012**, *7*, 83.

(5) Scott, J. F.; Morrison, F. D.; Miyake, M.; Zubko, P. *Ferroelectrics* **2006**, *336*, 237.

(6) Bibes, M. *Nat Mater* **2012**, *11*, 354.

(7) Gruverman, A.; Kholkin, A. *Rep. Prog. Phys.* **2006**, *69*, 2443.

(8) Han, H.; Kim, Y.; Alexe, M.; Hesse, D.; Lee, W. *Adv. Mater.* **2011**, *23*, 4599.

(9) Kang, S. J.; Bae, I.; Shin, Y. J.; Park, Y. J.; Huh, J.; Park, S.-M.; Kim, H.-C.; Park, C. *Nano Lett.* **2010**, *11*, 138.

(10) Rørvik, P. M.; Grande, T.; Einarsrud, M.-A. *Adv. Mater.* **2011**, *23*, 4007.

(11) Handoko, A. D.; Goh, G. K. L. *Science of Advanced Materials* **2010**, *2*, 16.

(12) Zhu, X. *Recent Patents on Nanotechnology* **2009**, *3*, 42.

(13) Shen, Z. K.; Chen, Z. H.; Li, H.; Qu, X. P.; Chen, Y.; Liu, R. *Appl. Surf. Sci.* **2011**, *257*, 8820.

(14) Shen, Z.; Chen, Z.; Lu, Q.; Qiu, Z.; Jiang, A.; Qu, X.; Chen, Y.; Liu, R. *Nanoscale Research Letters* **2011**, *6*, 474.

(15) Guo, L. J. *Adv. Mater.* **2007**, *19*, 495.

(16) Fang, J.-R.; Shen, Z.-K.; Yang, S.; Lu, Q.; Li, J.; Chen, Y.-F.; Liu, R. *Microelectron. Eng.* **2011**, *88*, 2033.

(17) Tavakkoli K. G., A.; Gotrik, K. W.; Hannon, A. F.; Alexander-Katz, A.; Ross, C. A.; Berggren, K. K. *Science* **2012**, *336*, 1294.

(18) Jeong, J. W.; Park, W. I.; Do, L.-M.; Park, J.-H.; Kim, T.-H.; Chae, G.; Jung, Y. S. *Adv. Mater.* **2012**, n/a.

(19) Herr, D. J. C. *J. Mater. Res.* **2011**, *26*, 122.

(20) Maksymovych, P.; Huijben, M.; Pan, M.; Jesse, S.; Balke, N.; Chu, Y.-H.; Chang, H. J.; Borisevich, A. Y.; Baddorf, A. P.; Rijnders, G.; Blank, D. H. A.; Ramesh, R.; Kalinin, S. V. *Phys Rev B* **2012**, *85*, 014119.

(21) Lucas, M.; Riedo, E. *Rev. Sci. Instrum.* **2012**, *83*, 061101.

(22) Ivry, Y.; Chu, D.; Durkan, C. *Appl. Phys. Lett.* **2009**, *94*, 162903.

(23) Cho, Y. *J. Mater. Res.* **2011**, *26*, 2007.

(24) Cho, Y.; Kazuta, S.; Matsuura, K. *Appl. Phys. Lett.* **1999**, *75*, 2833.

(25) Tanaka, K.; Kurihashi, Y.; Uda, T.; Daimon, Y.; Odagawa, N.; Hirose, R.; Hiranaga, Y.; Cho, Y. *Jpn J Appl Phys* **2008**, *47*, 3311.

(26) Berweger, S.; Neacsu, C. C.; Mao, Y.; Zhou, H.; Wong, S. S.; Raschke, M. B. *Nat Nano* **2009**, *4*, 496.

(27) Jia, C.-L.; Mi, S.-B.; Urban, K.; Vrejoiu, I.; Alexe, M.; Hesse, D. *Nat Mater* **2008**, *7*, 57.

(28) McGilly, L. J.; Gregg, J. M. *Nano Lett.* **2011**, *11*, 4490.

(29) Nelson, C. T.; Gao, P.; Jokisaari, J. R.; Heikes, C.; Adamo, C.; Melville, A.; Baek, S.-H.; Folkman, C. M.; Winchester, B.; Gu, Y.; Liu, Y.; Zhang, K.; Wang, E.; Li, J.; Chen, L.-Q.; Eom, C.-B.; Schlom, D. G.; Pan, X. *Science* **2011**, *334*, 968.

(30) Polking, M. J.; Han, M.-G.; Yourdkhani, A.; Petkov, V.; Kisielowski, C. F.; Volkov, V. V.; Zhu, Y.; Caruntu, G.; Alivisatos, A. P.; Ramesh, R. *Nature Materials* **2012**, *11*, 700.

(31) Lee, D.; Yang, S. M.; Kim, T. H.; Jeon, B. C.; Kim, Y. S.; Yoon, J.-G.; Lee, H. N.; Baek, S. H.; Eom, C. B.; Noh, T. W. *Adv. Mater.* **2012**, *24*, 402.

(32) Chanthbouala, A.; Crassous, A.; Garcia, V.; Bouzehouane, K.; Fusil, S.; Moya, X.; Allibe, J.; Dlubak, B.; Grollier, J.; Xavier, S.; Deranlot, C.; Moshar, A.; Proksch, R.; Mathur, N. D.; Bibes, M.; Barthelemy, A. *Nat Nano* **2012**, *7*, 101.

(33) Bocher, L.; Gloter, A.; Crassous, A.; Garcia, V.; March, K.; Zobelli, A.; Valencia, S.; Enouz-Vedrenne, S.; Moya, X.; Marthur, N. D.; Deranlot, C.; Fusil, S.; Bouzehouane, K.; Bibes, M.; Barthélémy, A.; Colliex, C.; Stéphan, O. *Nano Lett.* **2011**, *12*, 376.

(34) *The International Technology Roadmap for Semiconductors: 2011 Edition, Emerging research materials and Emerging research devices;* http://www.itrs.net/Links/2011ITRS/2011Chapters/2011ERM.pdf, http://www.itrs.net/Links/2011ITRS/2011Chapters/2011ERD.pdf.